On the age of the Milky Way bulge stellar population

Francisco Ricardo Surot Madrid

SIGILL: UNIVERSITAT: LUDOVIC: MAXIM:

München 2018

On the age of the Milky Way bulge stellar population

Francisco Ricardo Surot Madrid

Dissertation
an der Fakultät für Physik
der Ludwig–Maximilians–Universität
München

vorgelegt von
Francisco Ricardo Surot Madrid
aus Santiago, Chile

München, den 30. August 2018

Erstgutachter: Prof. Dr. Achim Weiss
Zweitgutachter: PD Dr. Markus Kissler-Patig
Tag der mündlichen Prüfung: der 27. September 2018

Contents

List of Figures

List of Tables

Die Milchstraße unterscheidet sich nicht wesentlich von anderen weit entfernten Spiralgalaxien. Allerdings erlaubt es uns unsere Lage innerhalb der Milchstraße, ihre Sternpopulationen mit einer Genauigkeit zu studieren, wie sie für extragalaktische Quellen undenkbar wäre. Der "Bulge" der Milchstraße (d.h. die Sternpopulation innerhalb von $\sim 3\,\mathrm{kpc}$ vom Galaktischen Zentrum) ist die massereichste der verschiedenen Komponenten der Milchstraße, die sehr alte Sterne beherbergt ($\gtrsim$10 Milliarden Jahre). Die Untersuchung der Eigenschaften dieser Sternpopulation kann deshalb Aufschluss geben über die Entstehung und Entwicklung der Milchstraße als ganzes, und von Spiralgalaxien im breiteren Kontext. Bislang herrscht weitgehend Konsens bezüglich der globalen kinematischen, chemischen und strukturellen Eigenschaften der Bulge-Population. Das Alter der Sterne im Bulge, oder besser gesagt die Altersverteilung, ist noch nicht vollständig verstanden.

Das Ziel dieser Arbeit ist es, bei den Fragen *"Wie alt ist der Bulge?"* und *"Gibt es einen räumlichen Altersgradienten im Bulge?"* anzusetzen, indem das Alter von Sternen in mehreren verschiedenen Feldern bestimmt wird, die alle innerhalb einer Zone von 300 Quadratgrad um das Zentrum des Bulges liegen.

Zum Einsatz kommen Aufnahmen des "VISTA Variables in the Vía Láctea" (VVV) Surveys, in denen durch Fitten der Point Spread Function die genauen Magnituden und Farben von einer halben Milliarde Sterne im Bereich des Bulges extrahiert werden. Die neu erstellten photometrischen Kataloge, die auch dafür genutzt werden, die Extinktion in Richtung des Bulges zu ermitteln, werden der gesamten wissenschaftlichen Gemeinschaft öffentlich zugänglich gemacht. Der Beitrag der vorgelagerten Disk-Population entlang der verschiedenen Blickachsen in Richtung Bulge wird mit Hilfe eines statistischen Verfahrens ermittelt und entfernt, um einen finalen Satz an Sternen zu erhalten, der ausschließlich die Bulge-Population repräsentiert. Das Alter der Sterne in verschiedenen Feldern wird durch den Vergleich der Beobachtungen mit synthetischen Sternpopulationsmodellen bestimmt, welche sorgfältig so konstruiert wurden, dass Beobachtungseffekte berücksichtigt werden (Streuung in der Entfernung, differenzielle Rötung, photometrische Vollständigkeit, photometrische und systematische Unsicherheiten). Die Simulationen zur Generierung der synthetischen Poulationen wurden auf zweierlei Arten durchgeführt: *i)* ein Modell, das eine spektroskopisch bestimmte Metallizitätsverteilung verwendet, dient als A-priori-Verteilung, so dass das Alter als einzig freier Parameter übrig bleibt; *ii)* ein genetischer Algorithmus findet aus allen möglichen Kombinationen von Alter und Metallizität die beste Lösung heraus (entsprechend einer uniformen A-priori-Verteilung in Alter und Metallizität).

Wir schlussfolgern letztlich, dass der Bulge selbst über seine gesamte Ausdehnung hinweg ($|l| < 10^\circ$ und $-10^\circ < b < +5^\circ$) im Schnitt alt zu sein scheint ($>$9.5 Milliarden Jahre), mit einem schwachen Altersgradienten von 0.16 Milliarden Jahren pro Grad in Richtung Galaktisches Zentrum.

The Milky Way (MW) galaxy is not much different from its faraway cousins. However, our position within the MW allows us to study the properties of its stellar populations with exquisite detail in comparison to extragalactic sources. The bulge of the MW (i.e. the stellar population within $\sim 3\,\mathrm{kpc}$ from the Galactic center) is the most massive stellar component of the MW that also hosts very old stars ($\gtrsim$10 Gyr), therefore the study of its stellar population properties can shed light on the formation and evolution of the MW as a whole, and of other spiral galaxies at large. So far, there is a general consensus on the global kinematic, chemical and structural properties of the bulge populations, however the age, or rather, the distribution of the ages of the stars in the bulge is yet to be completely understood.

In this work we aim at addressing the questions *"How old is the bulge?"* and *"Is there a spatial age gradient in the bulge?"* through the determination of the stellar ages in the different fields sparsely distributed within a region of $300\,\mathrm{deg}^2$ centered on the bulge.

We use VISTA Variables in the Vía Láctea (VVV) survey images to extract accurate magnitude and color of half a billion stars in the bulge area using point spread function fitting. The newly derived photometric catalogs, used in addition to probe the extinction towards the bulge, are made publicly available to the entire community. The contribution of the intervening disk population along the bulge lines of sight has been detected and removed by using a statistical approach in order to obtain a final stars sample that is representative of the bulge population only. The determination of the stellar ages in different fields is provided through the comparison between the observations and synthetic stellar population models, which have been carefully tailored to account for the observational effects (i.e. distance dispersion, differential reddening, photometric completeness, photometric and systematic uncertainties). The simulations leading to the construction of synthetic populations have been carried out by using two different methods: *i)* a model that uses a spectroscopically derived metallicity distribution functions as prior, leaving the age as the only free parameter; *ii)* a genetic algorithm that finds the best solution within all possible combinations of age and metallicity (i.e. uniform prior in age and metallicity).

We ultimately find that the bulge itself appears to be on average old ($>9.5\,\mathrm{Gyr}$) throughout its extension ($|l| < 10^\circ$ and $-10^\circ < b < +5^\circ$), with a mild gradient of about 0.16 Gyr/deg towards the Galactic center.

Chapter 1

Introduction

In this chapter I briefly summarize the current understanding of the Milky Way bulge as constrained from the physical properties of its stellar content. Particular emphasis is given to the kinematics, chemical content and morphology of the bulge probed by photometric and spectroscopic surveys, such as: the Optical Gravitational Lensing Experiment (OGLE - Udalski et al., 1992, 2015), the Bulge Radial Velocity Assay (BRAVA - Rich et al., 2007b; Howard et al., 2008), the Abundances and Radial velocity Galactic Origins Survey (ARGOS - Freeman et al., 2013), the GIRAFFE Inner Bulge Survey (GIBS - Zoccali et al., 2014), Gaia ESO Survey (GES - Gilmore et al., 2012; Randich et al., 2013), the Apache Point Observatory Galactic Evolution Experiement (APOGEE - Majewski, 2012; Majewski et al., 2015), and VISTA Variables in the Vía Láctea (VVV - Minniti et al., 2010).

The Milky Way (MW) is an *ordinary* spiral galaxy not much different from its nearest big neighbor, Andromeda, and much like uncountable other spiral galaxies in the Universe. However, it is only in the MW that we are able to resolve stars individually in all evolutionary sequences, therefore understanding the Galactic formation and evolution from the detailed properties (e.g. structure, kinematics, age and chemical abundances) of its stellar content. From an observational point of view, this brings both advantages and disadvantages. If on one hand being inside the MW (i.e. closer view) allows us to reach a level of detail that is unattainable for extragalactic studies, on the other hand it requires to map a very large area on the sky (i.e. hundreds of square degrees) and as such it is observationally very time-consuming, not to mention that the closer to the plane we observe, the higher the extinction gets, becoming prohibitive for any study based on optical passbands. Hence, it should come as no surprise if the current knowledge of the MW structure, formation and evolution has tremendously improved with the advent of the stellar spectroscopic and photometric surveys.

Within the MW, we usually distinguish three major stellar components; the halo, the disk and the bulge. The oldest known stars are in the Galactic halo, which is its most voluminous stellar component, extending well beyond 50 kpc from the Galactic center (Helmi, 2008; Xu et al., 2018, and references therein), albeit making up $\lesssim 1\%$ of the total stellar mass of the MW (Robin et al., 2003). Nevertheless, these very old and metal-poor field and cluster stars in the halo, are essentially the *fossil records* of the Galaxy's past, and are mainly exploited by Galactic archaeology to shed light on the formation of the MW, and by extension, that of other spiral galaxies (Zoccali & Valenti, 2016, and references therein).

The disk is instead the most massive stellar component of the MW, accounting for about three quarters of the stellar mass in the galaxy. It comprises two distinct components: the *thin* and *thick* disks, with exponential height scales of 300 pc and 900 pc, and length scales of 2.6 kpc and 3.6 kpc, respectively (Jurić et al., 2008). The stars in the thin disk are overall younger, more metal-rich and kinematically colder than stars in the thick disk (see e.g. Bensby et al., 2007, 2014, and reference therein). Therefore, although much more massive than the halo, the disk hosts stars whose ages span a very large range (from recently formed to several-Gyr old), but on average much younger than the halo.

Finally, with a stellar mass of $2.0 \times 10^{10}\,\mathrm{M}_\odot$ (Valenti et al., 2016) the MW bulge represents the most massive component that also hosts very old stellar populations ($> 10\,\mathrm{Gyr}$). As such, the detailed study of its stellar content provides the best way to understand how the bulk of the MW formed and evolved.

1.1 The Galactic bulge: a global view

Despite its importance as one of the major stellar components of the MW, until about a decade ago the bulge was still poorly explored, especially in its innermost regions. This was mostly due to the combination of: *i)* the large and patchy extinction that makes optical observations difficult, if not impossible, along many lines of sight; *ii)* the very limited performance of the past generation of near-infrared (near-IR) instrumentation; and *iii)* the relatively scarce availability of multiplexing capabilities, both in the optical and infrared domain. Consequently, our understanding of the MW bulge was mostly based on the study of the stellar population in few small low-extinction windows located close to the minor axis, i.e. Baade's Window at ($l = 1°, b = -3.8°$), the Plaut field at ($l = 0.9°, b = -8.5°$) or the SgrI-SWEEP field at ($l = 1.25°, b = 2.65°$).

The analysis of the color-magnitude diagrams (CMDs) of these few sampled fields suggested a purely old ($> 10\,\mathrm{Gyr}$) population (Ortolani et al., 1995; Kuijken & Rich, 2002; Clarkson et al., 2011; Zoccali et al., 2003), while the spectra of few tens of stars in Baade's Window and other external fields found the bulge population to be mostly metal-rich, with a mean peak around solar value and [α/Fe] enhancement (Rich, 1988, 1990; McWilliam & Rich, 1994; Rich & Origlia, 2005; Fulbright et al., 2006, 2007; Rich et al., 2007a). The general consensus was that the MW bulge experienced an early and very fast formation, and as such, it was believed to be the best template for the study of ellipticals and S0 spirals, due to the similar formation scenarios and other similarities that can relate bulges to these galaxies (see Falcón-Barroso et al., 2002).

However, the emerging picture based on the properties of the stellar population, probed across the bulge by the numerous recent photometric (i.e. OGLE, VVV) and spectroscopic (BRAVA, ARGOS, GIBS, GES, APOGEE-S) surveys, is much more complicated than we used to believe. The MW bulge is indeed a very complex structure.

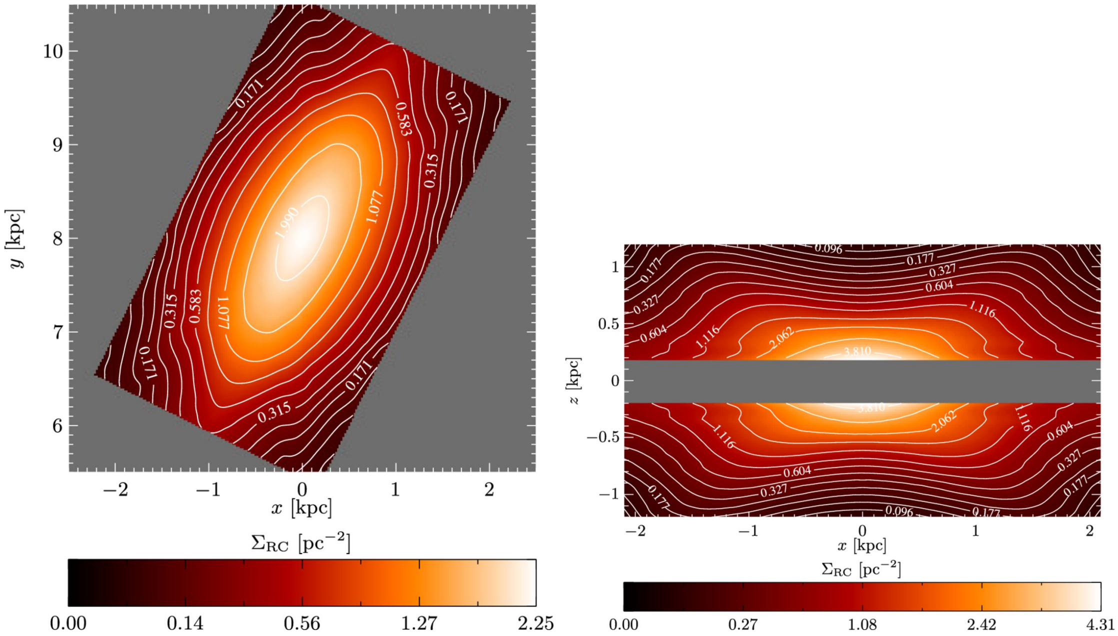

Figure 1.1: The MW bulge as seen from the North Galactic pole (left) and edge on (right). Numbers give the surface density of red clump stars in pc^{-2}, contours define isophotes separated by 1/3 mag. Figures reproduced from Wegg & Gerhard (2013).

1.1.1 Morphology and 3D structure

The first insights into the global morphology of the MW bulge come from the Cosmic Background Experiment (COBE) and Diffuse Infrared Background Experiment (DIRBE) (Weiland et al., 1994), which provided the first low angular resolution map of the bulge in the wavelength range between $1.25\,\mu$m and $4.9\,\mu$m. The surface brightness distribution of the bulge, as revealed from the infrared map, was consistent with a triaxial bar. Although, a bar in the inner Galaxy was first suggested much earlier by de Vaucouleurs (1964), from HI line profile at 21 cm observations.

Over the decades many different tracers have been used to confirm the presence of the bar and to constrain its properties. Nevertheless, the most compelling observational evidence for the existence of a bar in the bulge comes from studies of red clump (RC) stars, which can be used as standard candles to derive the stellar density distribution in the inner region of the Galaxy (see Zoccali & Valenti, 2016, for a recent review).

As a reminder note, RC are core helium-burning stars that can be used as distance tracers because their magnitude are fairly standard, changing slowly and smoothly with age and metallicity, an well represented in stellar evolution models (Salaris & Girardi, 2002).

Wegg & Gerhard (2013) used the VVV-DR1 (Saito et al., 2012a) to map the RC distribution across the inner $2.2 \times 1.4 \times 1.1$ kpc of the bulge. They find a strong boxy/peanut/X-shaped structure, with a bar orientation with respect to the Sun-Galactic center line of sight of $\sim 27°$, and whose near-side points towards the first Galactic quadrant ($0° \leq l \lesssim 30°$).

As shown in Figure 1.1, the outer bulge regions appear indeed as a boxy/peanut/X-shaped structure, which is a signature of the bulges formed out of dynamical instabilities in disk galaxies (see e.g. Debattista et al., 2006, and references therein). In particular the X-shape is produced by bending and buckling of elongated stellar orbits, the so-called *banana* and *anti-banana* orbits and even *brezel*-like orbits (see e.g. Portail et al., 2015).

From the observational point of view, the X-shaped structure (see right panel in Figure 1.1) causes a split (bimodality) in the RC magnitude distribution for fields in the outer bulge regions ($|b| > 5^\circ$) along the minor axis (McWilliam & Zoccali, 2010; Nataf et al., 2010; Saito et al., 2011; Gonzalez et al., 2015a). Specifically, this split in the RC distribution is the signature of two southern arms of the X-shaped structure crossing the line of sight.

Finally, the RC distribution towards the Galactic center suggests also the presence of an axisymmetric structure in the innermost $\sim$250 pc (Gonzalez et al., 2011; Gerhard & Martinez-Valpuesta, 2012; Valenti et al., 2016), and of a long bar with semi-major axis of $\sim$4.6 kpc, which appears to be the natural thin extension of the main bar at larger radii (Wegg et al., 2015).

1.1.2 Metallicity

The peak and the shape of the metallicity distribution function (MDF) of a given system provide crucial constraints on the initial mass function (IMF), star formation efficiency, as well as to the possible gas infall timescale (Matteucci et al., 1999; Ferreras et al., 2003). As such, over the decades many spectroscopic studies focused on the determination of the bulge MDF by targeting small samples of K or M giants in few fields sparsely located along the bulge minor axis (see e.g. Rich et al., 2012, and reference therein). The general agreement then was that the bulge population is on average metal-rich, although spanning a fairly broad metallicity range (e.g. $-1.5 \lesssim$ [Fe/H] $\lesssim +0.5$, where $[\mathrm{Fe/H}]_\star \equiv \log_{10}(N_{\mathrm{Fe}}/N_{\mathrm{H}})_\star - \log_{10}(N_{\mathrm{Fe}}/N_{\mathrm{H}})_\odot$). In addition, the presence of a metallicity gradient across the bulge has been debated at length since Minniti (1994) showed the first evidence by using a sample of globular clusters distributed within 3 kpc from the Galactic center (see Zoccali et al., 2008; Rich et al., 2012). However, the first comprehensive overview of the metallicity distribution in the bulge was provided only later by Gonzalez et al. (2013), who used a combination of VVV and 2MASS (Kleinmann, 1992) data to construct the first photometric metallicity map of the bulge. As clearly seen from the derived map (see Figure 1.2, left panel), the mean metallicity of bulge stars becomes progressively more metal-rich towards the Galactic center.

The detailed and systematic study of the MDF shape and its variation across the bulge became possible only thanks to the recent spectroscopic surveys (ARGOS, GIBS and GES), which all together have provided spectra for more than 20,000 RC stars across a large bulge area. Besides confirming the metallicity range constrained in previous studies, the most important finding (common to all surveys) is the presence of a composite population in the bulge. Specifically, all derived MDFs are best reproduced when considering two populations, metal-rich (MR) and metal-poor (MP), whose relative fraction

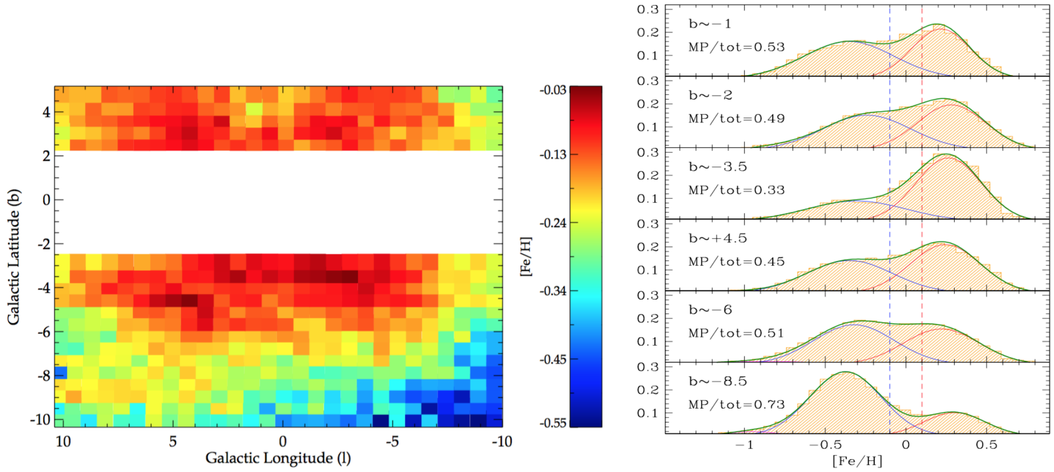

Figure 1.2: *Left:* Photometric metallicity map of the bulge based on VVV and 2MASS data. Figure reproduced from Gonzalez et al. (2013). *Right:* MDF of RC stars at constant latitudes based on GIBS data. The fraction of metal-poor stars compared to the total is given in each panel. Vertical dashed lines mark the limits of the metal-poor and metal-rich population. Figure adapted from Zoccali et al. (2017).

changes along different lines of sight, hence producing the observed mild vertical gradient found in earlier studies. As is evident in the right-hand panel of Figure 1.2, the peaks of the MP and MR components are roughly constant across varying longitudes, and centered around $[\mathrm{Fe/H}]_{\mathrm{MP}} \sim -0.33$ and $[\mathrm{Fe/H}]_{\mathrm{MR}} \sim 0.25$ in all observed fields. MP stars dominate in the outer bulge regions, while MR stars become more numerous moving towards the plane. However, Zoccali et al. (2017) also found evidence that in the innermost fields (i.e. $|b| < 3°$, see first 2 top right panels of Figure 1.2), the MP component becomes important again as its relative fraction starts increasing close to the plane. This new finding has been further investigated by Zoccali et al. (2017) by scaling the relative fraction of MP and MR component, as traced by the RC stars, to the total number of RCs in the bulge provided by the stellar density map of Valenti et al. (2016). This surprising result is shown in Figure 1.3, where the spatial distribution across the bulge of the MP and MR component is presented separately. The MP component displays an axisymmetric distribution, concentrated mostly within $|l| \lesssim 3°$ and $|b| \lesssim 4°$. On the other hand, the MR map has a distinctive boxy distribution, dispersed around $|l| \lesssim 6°$ and $|b| \lesssim 3°$, following the bar morphology.

An additional confirmation that MP stars do not trace the strong boxy/peanut/X--shaped structure is presented by Ness et al. (2012) and Rojas-Arriagada et al. (2017). These two studies have shown that only MR stars exhibit the split in the RC distribution, the typical signature of the X-shape (see §1.1.1).

Finally, studies of RR-Lyrae (RRL) (Dékány et al., 2013; Pietrukowicz et al., 2015; Gran et al., 2016) and Type II Cepheids (Bhardwaj et al., 2017), which are excellent tracers of old ($> 10\,\mathrm{Gyr}$) and MP population, reached the same conclusion.

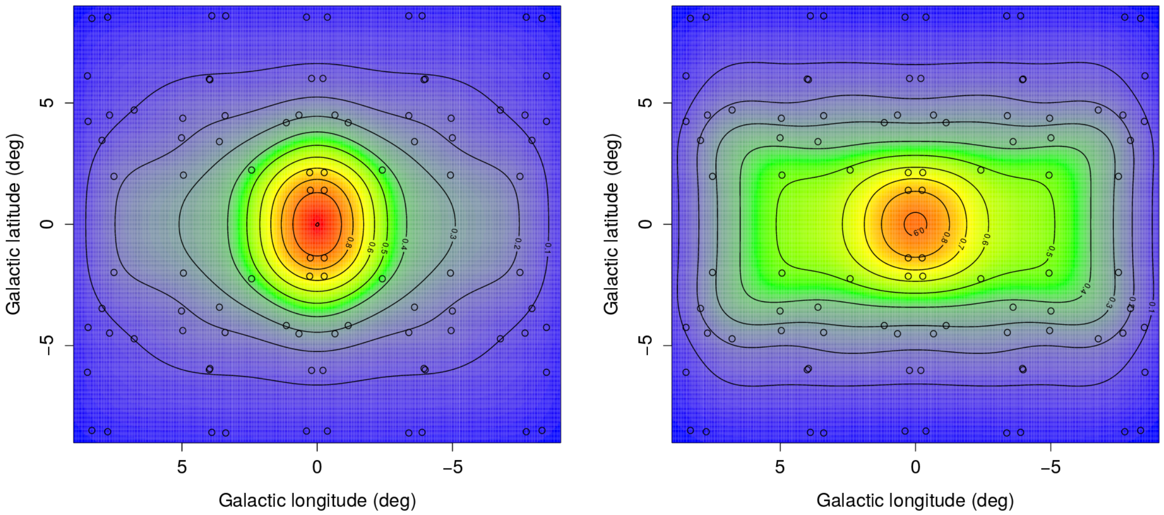

Figure 1.3: Density map of MP (left) and MR (right) RC stars obtained using the MDF of GIBS fields and the total number of RC stars from Valenti et al. (2016). Figure adapted from Zoccali et al. (2017)

1.1.3 Kinematics

With over six thousand spectra of M-giants in 42 fields distributed mostly across the outer bulge regions (i.e. $b \lesssim -4^\circ$) the BRAVA survey provided the first systematic study of the bulge kinematics. The study of the observed radial velocity and velocity dispersion (σ) of stars as a function of the position within the bulge revealed that overall the bulge rotates as a bar. Specifically, the radial velocity distribution of bulge stars gets steeper when moving towards the center (i.e. as function of the longitude), while showing very little spread at fixed longitude but different height from the plane. This trend, known as cylindrical rotation indicator, is characteristic of bulges that originate from the buckling instability of a, previously settled, rotating bar. When viewed edge-on, the stars are expected to show little difference in their mean rotation velocities measured at different scale height from the plane of the galaxy.

The cylindrical rotation has been later confirmed by the ARGOS survey at larger latitudes and longitudes, as well as by the GIBS survey that instead probed the innermost regions up to $b = -1^\circ$. In addition, the GIBS survey found the presence of a high σ peak in the central $\sim 200\,\mathrm{pc}$ (Zoccali et al., 2017), which matches a peak in the mass density profile obtained by Valenti et al. (2016). Very recently, Valenti et al. (2018) constrained and measured the central velocity dispersion peak within a projected distance from the Galactic center of $\sim 280\,\mathrm{pc}$, reaching $\sigma = 140\,\mathrm{km/s}$ at $b \pm 1^\circ$. There it is shown that the central σ peak is symmetric with respect to the Galactic plane, with a longitude extension at least as narrow as predicted by GIBS.

Finally, it is important to mention that only M- and K-giants are found to trace a cylindrical rotation pattern. Indeed, Kunder et al. (2016) showed that the kinematics of RRL stars (i.e. MP and old stars) do not rotate cylindrically.

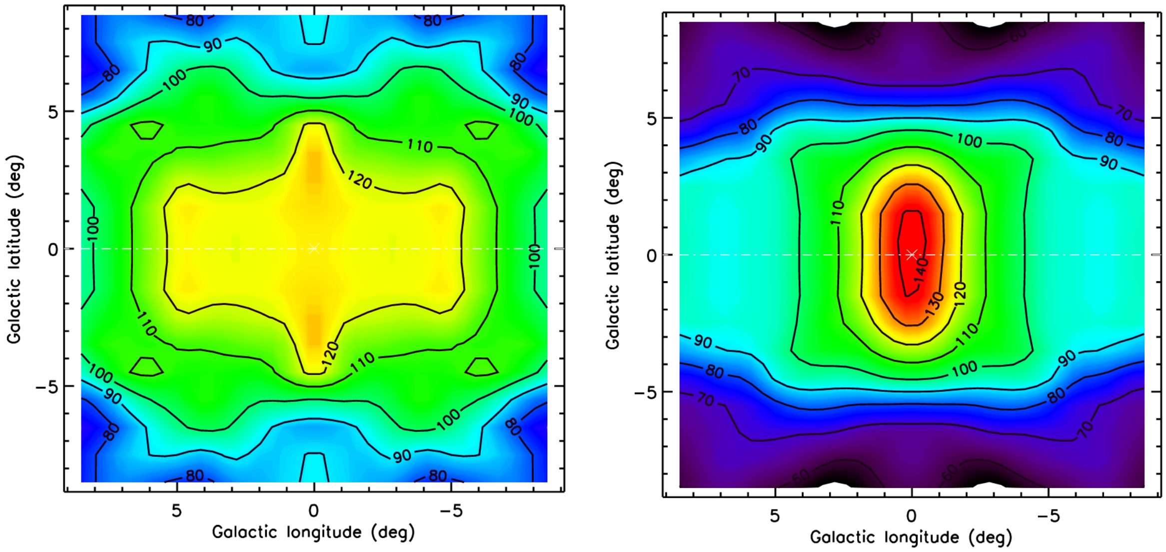

Figure 1.4: Spatial trends of the galactocentric radial velocity dispersion for the MP (left) and MR (right) component, respectively. The contours mark the constant-σ lines, with the respective numeric value, in km/s. Figure adapted from Zoccali et al. (2018).

1.1.4 Global properties of MP and MR components

As highlighted already in §1.1.2, the bulge MR and MP components have clearly different properties in terms of spatial distribution, that is, the MR component traces the bar while the MP one is much more spherically concentrated. When coupling the metallicity and kinematics information derived over the years from different surveys, it became evident that MP and MR stars in the bulge differ also in their kinematic properties.

By studying the vertex deviation, which is the angle formed by the velocity dispersion ellipsoid in radial velocity vs. longitudinal motion (v_r vs. μ_l), as a function of the stellar metallicity, Babusiaux et al. (2010) showed that MR stars display elongated orbits, which are typical of galactic bars, whereas MP stars generally exhibit isotropic orbit distribution, as axisymmetric spheroids.

Overall, the bulge rotates cylindrically like a bar (Rich et al., 2007b; Kunder et al., 2012; Ness et al., 2013b; Zoccali et al., 2014; Ness et al., 2016), however as shown in Figure 1.4, MR stars show a steep velocity dispersion (σ) gradient as a function of the latitude, from $\sigma \sim 50\,\mathrm{km/s}$ at $b = -8°$ up to $\sigma \sim 140\,\mathrm{km/s}$ at $b = -1°$. Instead, the MP component has a dispersion that ranges from $\sim$80 km/s in the outer region to $\sim$120 km/s at $b = -1°$ (Zoccali et al., 2017; Rojas-Arriagada et al., 2017).

Zoccali et al. (2018) provided the fractional contribution of MP and MR stars to the total stellar mass budget of the Galactic bulge, and its variation across the bulge area. They find that MP stars make up 48% of the total stellar mass of the bulge, within the region $|l| < 10°$, $|b| < 9.5°$, with the remaining 52% made up of MR stars. The MR component dominates the mass budget at intermediate latitudes $|b| \sim 4°$, but becomes marginal in the outer bulge ($|b| > 8°$). While the total σ has a trend that follows the total stellar mass, when one examines the σ of each component individually (see Figures 1.3 and 1.4), it is evident that the high central σ peak is actually due to the MR component, in a region where MR stars make up a smaller fraction of the stellar mass. This is due to the kinematic (i.e. orbits) and spatial distribution of the two metallicity component being significantly different.

1.1.5 Formation mechanisms

Historically, following the prescription of Kormendy & Kennicutt (2004), bulges have been classified into two main categories according to their formation: *classical* and *pseudo* bulges.

A structure that is the result of gravitational collapse of primordial gas or from the effects of early mergers is called a classical bulge. These systems share fundamental properties with elliptical galaxies, and experienced fast and early formation. As such, the bulge formed before the disk and its stellar population is sharply old and α-elements enhanced.

The Pseudo-bulges would form due to dynamical instabilities of the disk induced by the presence of a bar, meaning that they would be mostly disk-like, although still having characteristic properties (Zoccali & Valenti, 2016). The bar heats up the disk in the vertical direction, giving rise to the typical boxy/peanut/X-shape. In this case the emerging bulge shows bar-driven kinematics (i.e. cylindrical rotation) and the age and chemical content of the stellar population correspond to the properties of the disk at the bar formation time.

The formation mechanism of either classification of bulge also often implies that the classical bulge would be a spheroid (as is formed from collapse and chaotic mergers), while the pseudo-bulge would often be associated with the presence of a bar (Zoccali & Valenti, 2016). However, observations of high-redshift gas-rich disks hint towards a more complex scenario, where the bulge formation mechanism may be linked to the merging of smaller dense star forming clumps originating from the disk itself (see e.g. Bournaud et al., 2009, and reference therein).

In this context, it is therefore worth emphasizing that the profound differences between the spatial and kinematics properties of the MW bulge MR and MP components, as presented in the previous sections, do not necessarily imply a different origin scenario. Although it might be tempting to assign a classical and pseudo-bulge origin to the MP and MR components respectively, from a purely observational perspective, it is not possible to separate bulge populations on the basis of a given formation mechanism. Different models of bulge formation are being developed, arguing that a spheroidal shape can be obtained through different formation scenarios (see e.g Di Matteo, 2016; Debattista et al., 2017; Fragkoudi et al., 2017), which do not invoke a gravitational collapse but rather the evolution of disks with various properties. As observers, we can instead provide detailed description of the MR and MP components in terms of spatial, kinematics, chemical abundances, but most importantly age properties. In this way, future bulge formation models can be constrained much better than before, hopefully allowing us to definitely discard some scenarios in favor of the others.

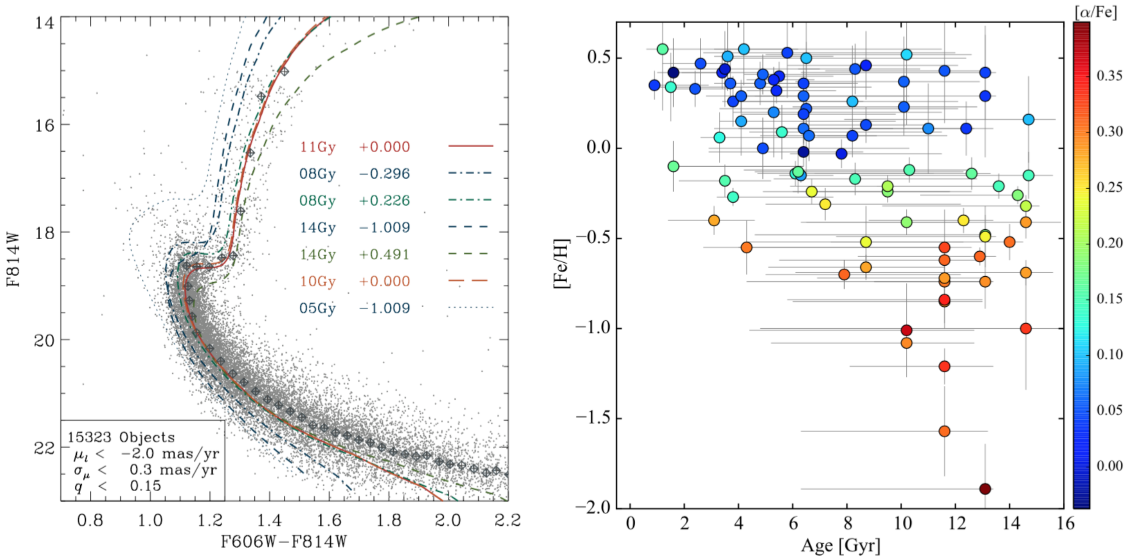

Figure 1.5: Bulge stellar ages derived from photometric and spectroscopic studies. *Left:* CMD of the Sgr-I-SWEEP field decontaminated by disk stars using proper motion compared with isochrones of different metallicity and age. Figure adapted from Clarkson et al. (2008). *Right:* Age versus [Fe/H] for a microlensed dwarfs sample. Figure reproduced from Bensby et al. (2017).

1.2 The bulge age: current view and tension

While there is a general agreement regarding the properties of the bulge morphology (i.e. 3D structure), metallicity and kinematics, an unanimous consensus on the age is still missing. Indeed, in the recent years the age of the bulge stellar population has been the most controversial problem because of a number of contradicting results based on different approaches.

Dating bulge stars is a very complicated task, challenged by the stellar crowding, the large and high differential extinction, the uncertainties in the distance modulus, the distance spread due to the spatial depth of the bulge/bar along the line of sight, the metallicity dispersion, and finally the contamination by foreground disk stars. The different contributions of all these factors prevent accurate location, in terms of magnitude and color, of the main sequence turn-off (MS-TO) for the bulge population, so far among the most reliable age diagnostics (Renzini & Fusi Pecci, 1988). Historically, the earliest age constraint by van den Bergh & Herbst (1974) in the Plaut field along the bulge minor axis at $b = -8°$ (∼1 kpc) indicated a globular cluster-like age. Terndrup (1988) fitted the photometry of bulge fields at a range of latitudes with globular cluster isochrones of varying metallicity, but lacking a certain distance for the bulge, only a weak age constraint (11-14 Gyr) was derived. Ortolani et al. (1995) solved the problem of the distance uncertainties by comparing the bulge population with the two clusters NGC 6528 and NGC 6553. Specifically, by measuring the difference between the RC and the MS-TO magnitudes in the bulge field and in the clusters, for the first time they showed that the relative ages of the bulge and metal-rich cluster population could not differ by more than 5%. Feltzing & Gilmore (2000) used the counts of stars brighter and fainter than the MS-TO observed in their Hubble Space Telescope (HST) based photometry of Baade's Window and another low extinction field known as Sgr-I-SWEEP at $l = 1.25°$ and $b = 2.65°$, to argue in favor of an old age. The case for a *purely old* bulge has been further strengthened by later studies based on more accurate HST (see e.g. left panel of Figure 1.5) and ground based photometry of different bulge fields located mostly along the minor axis (Kuijken & Rich, 2002; Clarkson et al., 2008, 2011; Zoccali et al., 2003), but also at the edge of the bar (Valenti et al., 2013). Unlike previous works, the problem of contamination from foreground disk stars was tackled either by a kinematic decontamination by using proper motions (Kuijken & Rich, 2002; Clarkson et al., 2008, 2011), or statistically by considering control disk fields (Zoccali et al., 2003; Valenti et al., 2013). From the analysis of optical and near-IR decontaminated CMDs, these studies found the majority of the bulge stellar population to be old (i.e. $> 10\,\mathrm{Gyr}$), with no evidence of significant age differences between the field and old MW cluster population. In particular, Clarkson et al. (2011) provided an upper limit of $\sim$3.4% for a bulge component younger than 5 Gyr, although arguing that the majority of the stars brighter than the old MS-TO in their CMD could be blue straggler stars (BSS).

There is, however, a clear discrepancy between the ages inferred from the determination of the MS-TO in the observed CMDs and those derived by the microlensing project of Bensby and collaborators (Bensby et al., 2013, 2017), which derives individual stellar ages from the effective temperature and gravity (i.e. from isochrones in the $[\mathrm{T_{eff}}, \log \mathrm{g}]$ plane) as obtained from high resolution spectra. Bensby et al. (2017) observed a sample of 90 F and G dwarf, turn-off and subgiant stars in the bulge (i.e. $|l| \lesssim 6°$ and $-6° < b < 1°$) during a microlensing event, which amplifies the light of the otherwise too faint dwarf and allows for high-resolution spectra studies to be carried out even as far as the bulge. They found that about 35% of the MR stars ($[\mathrm{Fe/H}] > 0$) span ages in between 8 Gyr and 2 Gyr, whereas the vast majority of MP ($[\mathrm{Fe/H}] \lesssim -0.5$) are 10 Gyr or older (see right panel of Figure 1.5). In addition, from the derived age-metallicity and age-α elements distribution the authors concluded that the bulge must have experienced several significant star formation episodes, about 3, 6, 8 and 12 Gyr ago. Comparable results have been found by Schultheis et al. (2017), who presented the age distribution of 74 giants in Baade's Window as a function of stellar metallicity. Specifically, the relation of Martig et al. (2016) calibrated on asteroseismic data has been used to link the [C/N] abundances measured from APOGEE spectra to the stellar age. While the age distribution of the MP ($[\mathrm{Fe/H}] < -0.1$) giants peaks at 10 Gyr with a decreasing tail towards younger age (as young as 2 Gyr), MR ($[\mathrm{Fe/H}] > -0.1$) stars can be either young or old. Indeed, their age distribution appears bimodal, with two peaks at 4 and 11 Gyr.

Different concepts have been explored and proposed to partially reconcile the spectroscopic and photometric ages. In this respect the first attempt was presented by Nataf & Gould (2012) and Nataf (2016) who proposed a higher helium enrichment factor than currently adopted for the MR isochrones. The use of standard isochrones on He-enhanced stellar populations would lead to photometric and spectroscopic ages that are over- and under-estimated, respectively. Therefore, the discrepancy could be interpreted under the assumption that the chemical evolution of the bulge is He-enhanced. On the other hand, Haywood et al. (2016) suggested the discrepancy being caused by the effect of the age--metallicity degeneracy that makes it hard to distinguish in the CMD a young MR star from an old MP one. They compared the MS-TO color spread observed in the CMD of Clarkson et al. (2011) with that of synthetic CMDs obtained by using two different age-metallicity relations: *i)* the one presented by Bensby et al. (2013), based on a total sample of 59 micorlensed dwarfs, and *ii)* one that extends from [Fe/H] $= -1.35$ dex at 13.5 Gyr to [Fe/H] $= +0.5$ dex at 10 Gyr. When taking into account distance, reddening and metallicity effects, Haywood et al. (2016) showed that the MS-TO color spread of a *purely* old stellar population would be wider than what is observed, and thus advocating for the presence in the bulge of a conspicuous population of young and intermediate-age stars. Very similar results have been presented by Bernard et al. (2018) who calculated the star formation history (SFH) of four bulge fields, including that of Clarkson et al. (2011). Their findings suggest that over 80% of the stars are older than 8 Gyr, but also the presence of star formation as recent as $\sim$1 Gyr.

1.3 The goal of this project

Clearly, as of today the age distribution of the bulge is still not universally understood, and in particular its spatial variation across the large area of the bulge has not been explored. In this framework, the use of near-IR deep photometry provided by the VVV survey represents a unique opportunity, as it covers the central $\sim 300\,\mathrm{deg}^2$. of the bulge and can penetrate the high extinction near the plane that the optical studies avoid.

With this in mind, we have set off to obtain photometrically derived age estimates of the bulge, with the ultimate ambitious goal to produce an age map.

To do so, we derive a new set of point-spread function (PSF) fitting photometry in $\mathrm{JK_s}$ for the whole VVV bulge area ($|l| < 10°$, $-10° < b < +5°$), which is better suited to handle the highly crowded fields near the Galactic plane than aperture photometry. This new photometry includes completeness values to assess how many stars at given $\mathrm{JK_s}$ values we are not observing, as well as a new high resolution extinction map for the whole area.

We use the CMDs derived from the new photometry in several bulge fields and we remove the contamination from foreground disk by using a statistical approach. The resulting clean bulge CMDs are then compared with synthetic populations, specifically tailored for each field such as to include the effects of differential reddening, distance dispersion, and photometric and systematic uncertainties associated with the observations.

The comparison between observed and synthetic CMDs finally leads to the stellar age determination. However, this is done by using two different approaches.

On method exploits the advantage of knowing the metallicity distribution of the bulge stars from the GIBS survey, so by imposing the observed MDF the age is the only free fitting parameter. The second method uses neither age nor metallicity initial assumptions, allowing a genetic algorithm to define the best solution in what would be the SFH reconstruction, or the 'ignorance model'.

Lastly, we compare the ages from these results with a set of N-body simulations, discussing the new results with respect to earlier studies.

Chapter 2

The new bulge photometry

This chapter provides and overview of the new photomerty I have obtained for a bulge region of $\sim 300\,\mathrm{deg}^2$ around the Galactic center. It includes the methodology used to obtain calibrated photometric catalogs from the available images, as well as some interesting applications. Most of the details discussed here are presented in Surot et al. (2018b, in prep), with the exception of §2.6 and §2.7.

2.1 The dataset

In this work, we have used a combination of J and $\mathrm{K_s}$ images from the VVV survey (Minniti et al., 2010) collected with the wide field near-IR imager VIRCAM mounted on the VISTA 4-m telescope on ESO Paranal Observatory.

The VVV survey mapped an area of about $300\,\mathrm{deg}^2$ centered on the Milky Way bulge ($-10° < l < +10°$, $-10° < b < +5°$), and $250\,\mathrm{deg}^2$ covering a portion of the southern disk ($-65° < l < -10°$, $|b| < 2°$). It is divided into observational groups called *tiles*, which cover roughly $1.6\,\mathrm{deg}^2$ each, for a total of 196 tiles in the bulge (designated b201-b396) and 152 in the disk (called d001-d152). The survey used two observing modes, one providing quasi simultaneous single-epoch observations in ZY JH$\mathrm{K_s}$ passbands, and another following a variability multi-epoch study in $\mathrm{K_s}$. However, at the end of the survey, all bulge fields ended up having effectively 2 epochs also in J.

VIRCAM is equipped with a mosaic of 16 detectors with gaps about the size of the detectors themselves between them. The average pixel scale of the detectors is $0.399''$, with percent-level variations across the whole detectors ensemble, resulting in each detector covering $\sim 133\,\mathrm{arcmin}^2$ on the sky. A single VIRCAM frame is called *pawprint*, and it consists of 16 single-detector images (SDIs).

The VVV observing strategy was designed to obtain a pair of pawprints jittered by $\sim 20''$ to account for detectors bad cosmetics, at 6 different positions. The combination of the paired jittered pawprints is referred to as stacked pawprint (see left panel of Fig.2.1).

The offsets pattern between the 6 positions was properly defined in order to get a nearly homogeneous sky coverage of $\sim 1.5 \times 1.2\,\mathrm{deg}$, the so-called tile. The right panel of Figure 2.1 shows a schematic view of the pattern of offsets for any given detector of the stacked pawprint. In summary, a single tile is composed of 16×6 SDIs (i.e. a stacked pawprint $\times6$ positions), per epoch, per filter.

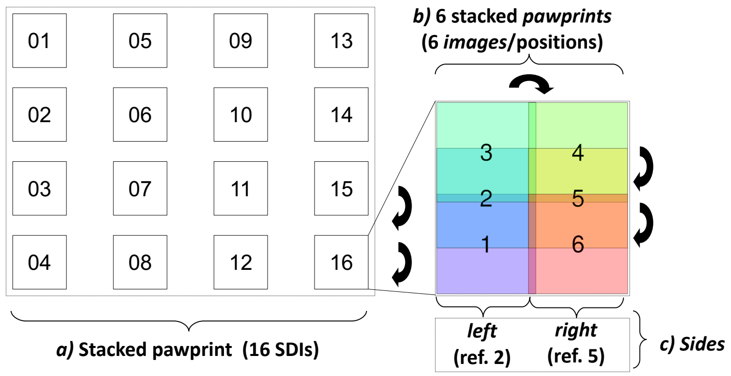

Figure 2.1: *Left panel*: Representation of a stacked pawprint. *Right panel:* Schematic pattern for any given SDI in the 6 stacked pawprints. Colours and numbers denote the order in which the 6 exposures are taken, and the semi-transparent shaded areas around them the corresponding field of view.

The exposure time per pawprint and epoch was only 4 sec for K_s and 2×6 sec for J. With this strategy almost every pixel within a tile gets exposed at least twice, yielding effective exposure time of 8 sec for K_s and 24 sec for J-band for the stacked pawprints. However, the overlap areas between stacked pawprints and edges of the tiles had 2-6 times higher exposures causing the noise distribution within a tile to vary strongly with position in the sky. For this reason we decided to work on the stacked pawprint images (i.e. average of the two jittered exposures at each pawprint position), rather than using the final tile images. Such images are available for download at Cambridge Astronomy Survey Unit (CASU[1]), after the corresponding raw science and calibration frames are processed by the VISTA data flow system pipeline (Lewis et al., 2010). For a more detailed description see Saito et al. (2012a).

Figure 2.2 shows schematically the bulge area covered by the observations, and the official VVV tiles numbering used also in this work. Tiles for which 2 epochs in J and K_s have been used are highlighted in green. In principle we could have used 2 epochs for all 196 tiles because they have been observed twice in J-band and up to 290 times in K_s. However, to enabling the study of the age and age variation across the bulge a basic requirement is to obtain CMDs as deep and accurate as possible. This is achieved when all images in both bands have similarly good image quality (IQ). Only 65% of the tiles satisfies this images selection criterion for both filters in 2 epochs. The complete list of stacked pawprint images used in this work amounts to 3912 (corresponding to $3912\times16=62592$ SDIs). The average IQ of the selected images is $0.75''\pm0.1$ and $0.54''\pm0.04$ for J and K_s bands, respectively.

---

[1] http://casu.ast.cam.ac.uk/

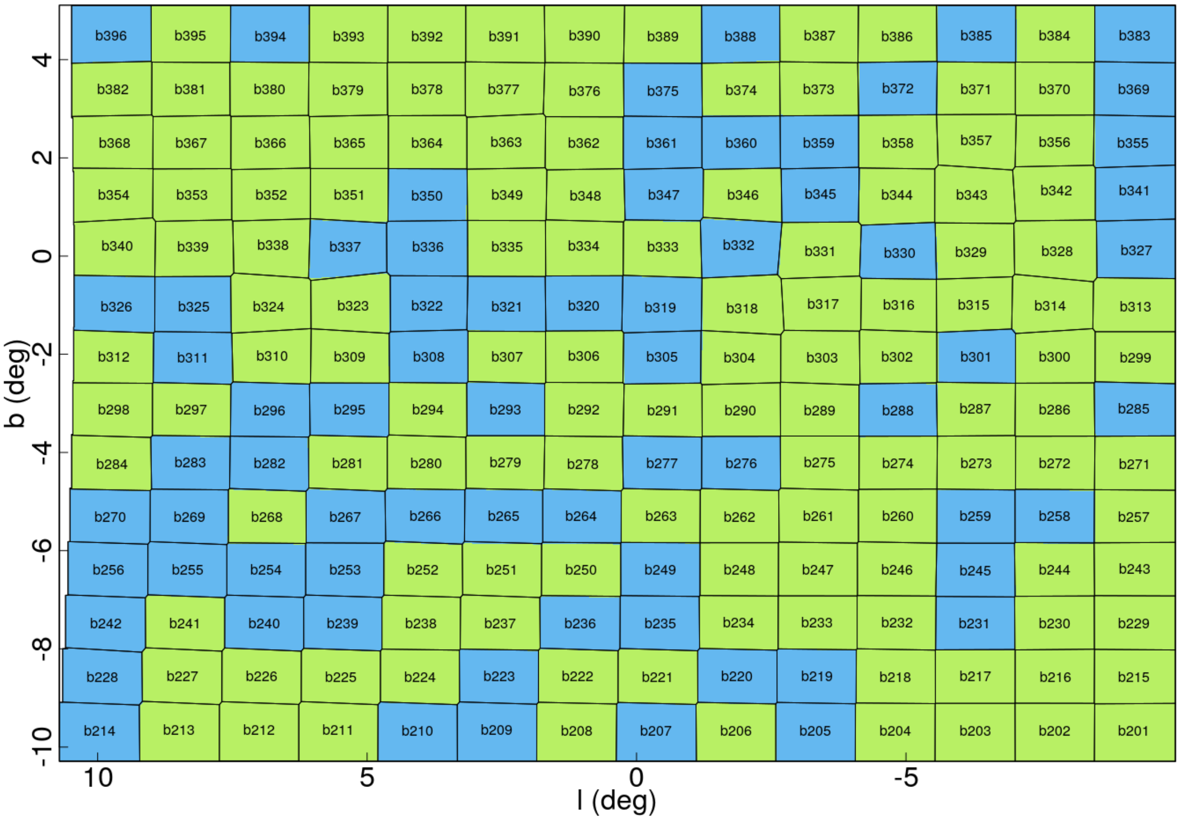

Figure 2.2: VVV survey bulge area and tile numbering. The color code refers to the number of epochs used to construct the photometric catalog of each tile: green for 2 epochs and blue for only 1 epoch.

2.2 PSF photometry

The bulge region studied here is characterized by a very large star density, especially close to the Galactic plane ($|b| < 3°$, $\gtrsim$1500-3000 stars per arcmin^2), therefore to obtain accurate stellar photometry we used point spread function (PSF) fitting algorithms on each SDI, independently. In this regard, each SDI has its own PSF, and as such, it is expected to represent an independent photometric system (i.e. zero-points). Therefore, to obtain the final photometric catalog of any given tile we must first calculate and apply an internal detector-by-detector photometric calibration, and then combine all the SDI catalogs together. In addition, we need to assess the photometric and systematics errors affecting the derived magnitude, as well the completeness level (i.e. fraction of observed to truly present/recovered stars per color-magnitude bin).

To this end, we make use of an ad-hoc customized pipeline based on DAOPHOT, ALLSTAR (Stetson, 1987), and ALLFRAME (Stetson, 1994) to extract the magnitudes from the SDIs. Later for quick image coordinates transformations and internal cross-matching we use DAOMASTER (Stetson, 1993).

2.2.1 Initial parameters

The first step towards the catalog creation, is to propose a set of initial parameters to the DAOPHOT routine. For this purpose we first set the gain[2] and read-out noise (RON[3]) levels, as published in the ESO Health Check monitor for the VIRCAM instrument. From this database, we have taken the closest values to the time of observation for each SDI.

From the VIRCAM manual[4] we obtain for each detector the recommended analog-to--digital unit (ADU) value corresponding to the linearity régime. However, we found that the values listed in the manual not always reflect what is observed in the SDIs, possibly because the reduction process due to dark correction, flat-fielding and combination of the jittered pair frames, has slightly changed the baseline counts for each FITS. In fact, visual inspection of the SDIs revealed that very bright stars (that should be and look like completely saturated) do not show the expected plateau in the counts, but rather a *hole* with near-zero counts in their center, surrounded by a somewhat smooth ring (see Figure 2.3).

We argue that this is due to the handling of overflow values, when a high number count is reset to some negative number following a misinterpretation of a sign bit, and it is smoothed out by the jitter combination. Using this kind of stars as a guideline, we have defined our highest count limit to 18,500 counts, which is roughly the level at which we can still find star-like (i.e. PSF) signals, minus some arbitrary conservative margin of 1,000 counts. In case of detector #5, which has a notoriously lower listed high-count limit in the instrument manual, we have decided to reduce the high-count limit value to 15,500. We will henceforth refer to this as our *saturation limit*, even though, as stated here, it is not

---

[2] http://www.eso.org/observing/dfo/quality/VIRCAM/reports/HEALTH/trend_report_GAIN_AVG_HC.html

[3] http://www.eso.org/observing/dfo/quality/VIRCAM/reports/HEALTH/trend_report_READNOISE_AVG_HC.html

[4] http://www.eso.org/sci/facilities/paranal/instruments/vircam/doc.html

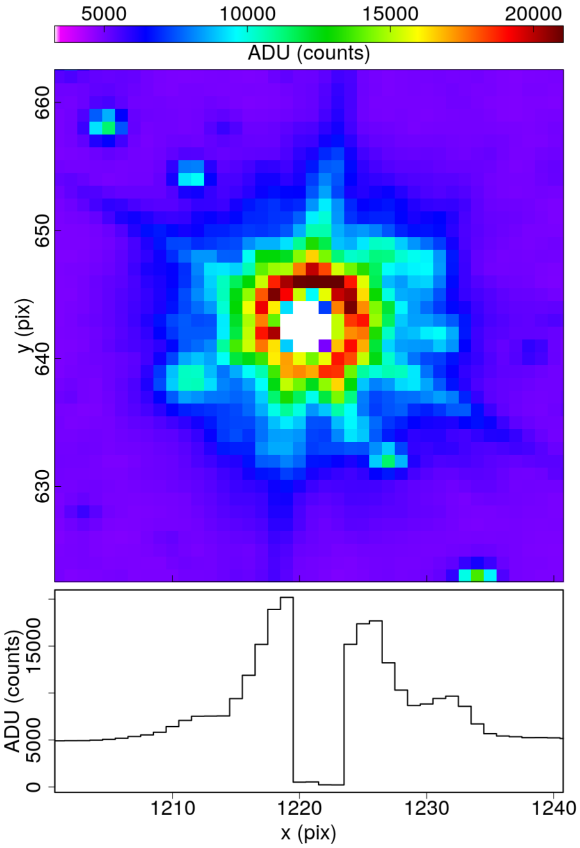

Figure 2.3: Zoom in to a saturated star in detector #5. The top panel shows a heatmap of the ADU counts, while the bottom panel is an horizontal cut through the center of the star. In cases like this very bright star the fault is evident, but for moderately saturated stars the central dip is much more subtle and cannot be filtered out simply.

directly to the point of actual saturation, but to when the images start being indirectly affected by it.

By taking the brightest stars in the images and measuring the approximate radius from their center at which the ADU rises well above the local sky level, we have arrived at 15 pixels to be a reasonable value for the PSF radius. This value has been adopted throughout the whole reduction procedure that leads to the catalog extraction, regardless of detector.

As the next step, we need to determine the Full Width at Half Maximum (FWHM) of the stars. It turns out that the FWHM values stored in the image headers are sometimes at odds with what is seen in the image, and in our earliest results we found several exceptions that forced us to produce an independent measure of the FWHM. In the end, we favored a brute force approach, where we select 2,000 stars by using the DAOPHOT/PICK subroutine (pick-stars) from each image, estimate their FWHM from their profiles based on their maximum number of counts and the surrounding background, and obtained a general FWHM for the image from the median of the ensemble. Several tests on different fields and images, showed that this was sufficiently close to the original value in general, and once we started using this estimator on the most problematic fields, the related issues were resolved and the CMDs were consistent across neighboring tiles and SDIs. We use the so-derived FWHM as the PSF fitting radius.

2.2.2 PSF calculation

To construct the PSF model for each SDI we select 450 bright isolated stars that are still well below the saturation limit (see §2.2.1) by using the DAOPHOT/PICK subroutine.

We then proceed to iteratively filter out stars with a bad profile shape and bad pixels, as defined by DAOPHOT, until no star has bad-pixels in its fitting radius and the final sample has no profile outliers.

Once the selection of PSF-stars have been made, we calculate their profile using a Moffat distribution[5] with $\beta = 2.5$ and allowing for a quadratic XY variation. The so--derived PSF-model is used as input parameter in the ALLSTAR routine, allowing to remove neighboring stars, and subsequently re-fitting the PSF profile. An iteration of 5 times usually led to a convergent profile for most SDIs. However, for certain problematic cases, it was necessary to reduce the counts saturation limit (i.e. in steps of 1,000 ADU). The computational routine leading to the final PSF-model is schematically reproduces in Figure 2.4 in the form of a flow diagram.

2.2.3 SDIs mosaic and catalog calibration

In short, PSF-fitting photometry is performed independently on each SDI by using the ALLFRAME routine and the PSF-model as derived in §2.2.2. However, in practice the entire photometric procedure is very complex because of the need to process a large number of individual images, and the requirement of being able to produce a coherent mosaic of the corresponding catalogs with accuracy.

To match all catalogs we need to transform the in-image stellar positions (i.e. XY coordinates) into a new common reference system (i.e. X'Y' coordinates) by applying coordinate transformations equivalent to a simple shift and rotation. Accurate coordinates transformation are best obtained if derived on overlapping regions that are sufficiently large and uniform. However, the SDIs themselves are not uniform due to the ~ 60 pixel jitter applied during the observations (see §2.1), and coordinate transformations based mostly on the overlapping edges of the SDIs (i.e. the vertical overlap area in the right panel of Figure 2.1) were characteristically unreliable. For this reason, following the references given in the right panel of Fig 2.1, for each detector we decided to group the SDIs and corresponding catalogs of the 6 stacked pawprints into two sides: *left* (stacked pawprints 1, 2 and 3) and *right* (stacked pawprints 4, 5 and 6). Each *side* would then have a particular XY-to-X'Y' transformation, based on the coordinates system of stacked pawprint 2 for the

---

[5] $f_{\mathrm{Moffat}}(x, y, \beta) = \gamma \left(1 + \frac{x^2}{\alpha_x^2} + \frac{y^2}{\alpha_y^2} + \alpha_{xy} xy\right)^{-\beta}$, where γ, and the α coefficients are free parameters set by the fit.

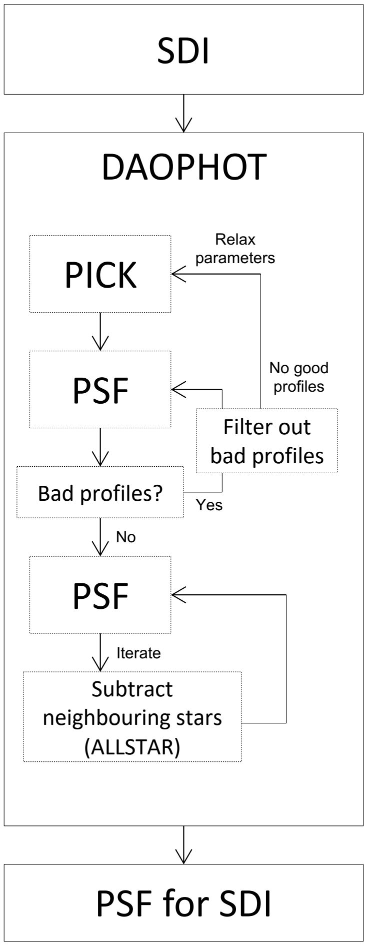

Figure 2.4: Flow diagram of the computational routine used to obtain the PSF model of each SDI

left, and 5 for the *right*. In case of multi-epoch observations (i.e. 12 stacked pawprints per filter), the reference is taken from the earliest epoch set.

What follows is the detailed description of the procedure applied to 3 SDIs of one of the two sides (i.e. left or right), for one of the 16 detectors. To aid the reader, such procedure is also schematically shown in Figure 2.5 as flow diagram. As a first step, for a given detector we run the ALLSTAR routine on each SDIs-side in order to obtain the corresponding preliminary photometric catalogs, that are used exclusively for mosaic construction purposes.

DAOMASTER is then used on each side set to derive the coordinates transformation, and to create a mosaic of combined SDIs-side (steps 1 to 3 in Figure 2.5). We process the so-derived side mosaic images (one per filter and epoch) with ALLSTAR only to obtain the corresponding list of stars centroids in the new coordinates system (step 4 in Figure 2.5). We finally perform PSF-fitting photometry with ALLFRAME on all J and K_s side SDIs, by using also the coordinate transformations that lead to the mosaic, and the PSF models

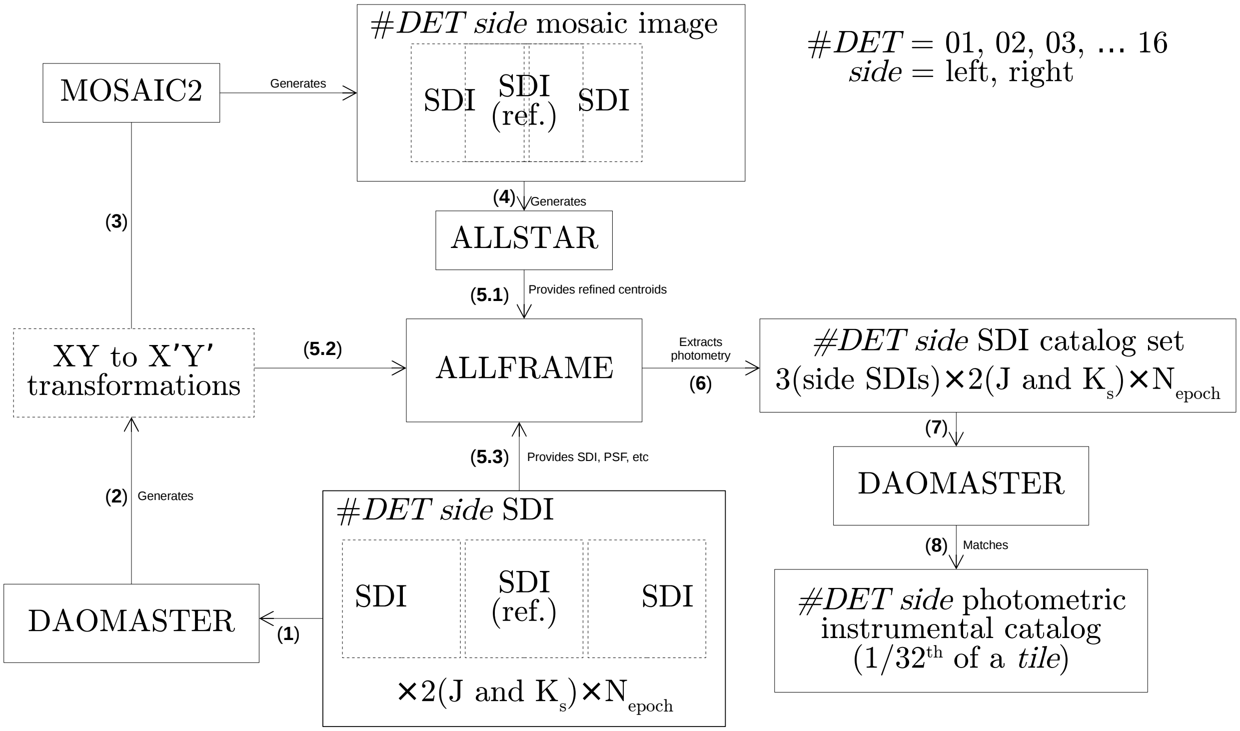

Figure 2.5: Flow diagram of the computational routine used to obtain the photometric catalog of a given detector SDIs-side. See text for further details.

as derived in §2.2.2 (see steps 5.1 to 5.3 in Figure 2.5). The advantage of ALLFRAME over ALLSTAR is that the former allows for a better refinement of the sources centroid, enabling to derive a deeper photometry. The output products are photometric catalogs containing all stars detected in a given detector, per side and filter (step 6 in Figure 2.5). This means that for each one of the 196 bulge tiles, we ended up having a total of 16 (detectors) × 2 (sides: left and right) × 2 (filters, J and K_s) single band catalogs. The joint JK_s catalogs containing all stars from a given detector and side are then obtained through cross-correlation by using again DAOMASTER and the previously derived coordinate transformations (steps 7 and 8 in Figure 2.5).

The absolute magnitude calibration of the photometric joint JK_s catalogs is obtained through cross-correlation with the catalogs produced by CASU for the same set of images. Specifically, we first transform the XY position of the detected sources in these catalogs into the absolute system RA-DEC by using the WCS recorded in each image header. Then the match with the CASU catalogs is done with STILTS (Taylor, 2006), using a RA-DEC separation criterion with a tolerance of 0.5 arcsecs, roughly 1.5 pixels. Overall, the match presents a natural spread of about $\pm(0.02 - 0.03)$ mag for J and usually a 50% higher for K_s (see Figure 2.6).

We also perform internal crosschecks within different pawprint images for which we have significant overlap. From these matches, the general result is a well centered dispersion of

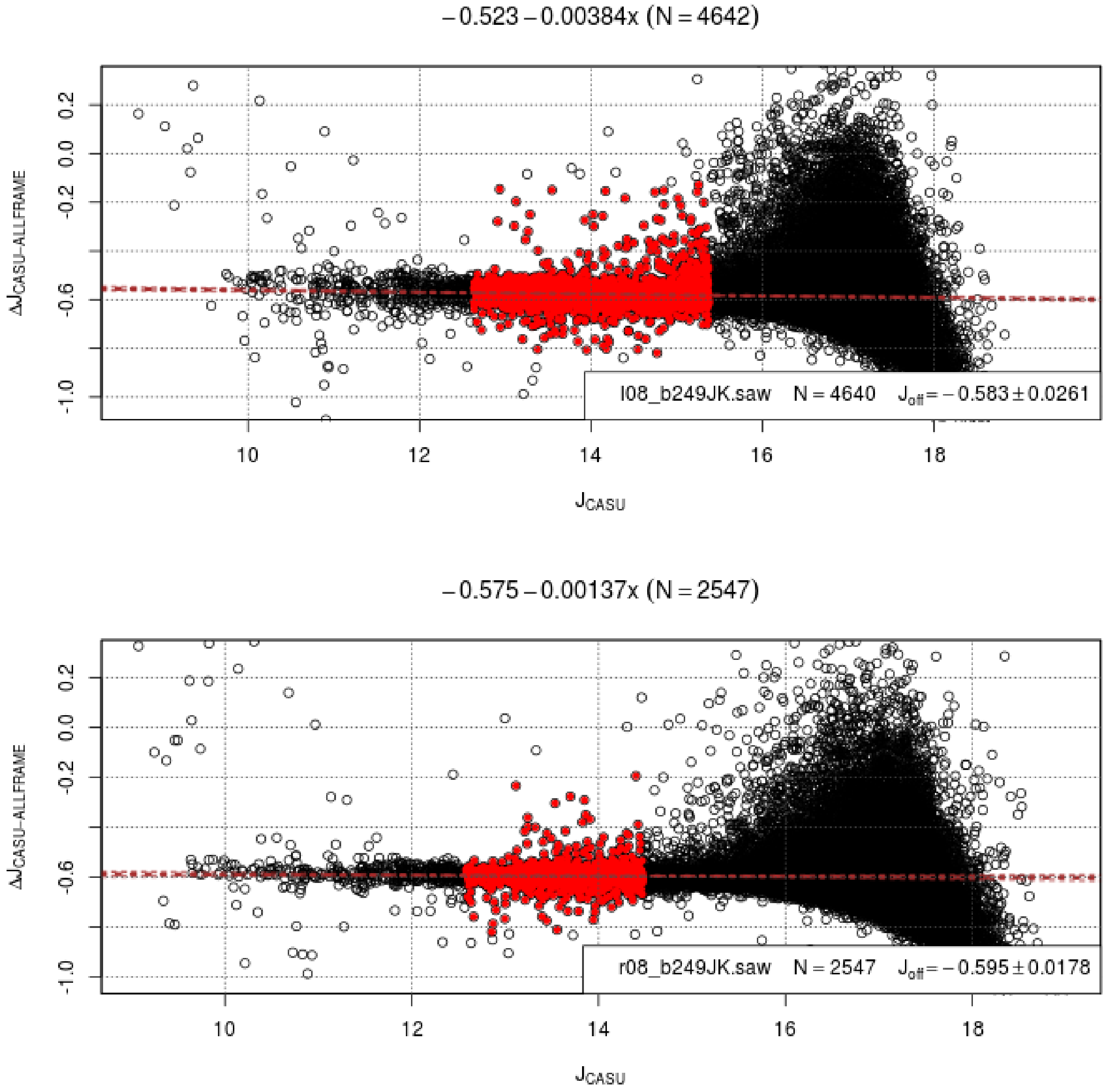

Figure 2.6: Example plot for the CASU-ALLFRAME calibration for detector #8 of tile b249. Top panel refers to the *left* side, while the bottom panel to the *right* side. Displayed is the magnitude difference in J between CASU and ALLFRAME catalogues vs. CASU reference. The black circles follow all the matches, while the red dots mark the selected magnitude range where the zero-point is calculated. The title of each plot refers to the linear fit performed on the red dots, as well as the number of stars from which it is derived. Also shown in the legend is the source catalog, the estimated zero-point and the corresponding uncertainty. The criterion to select the red dots is dependent on a window from which we have the minimum spread in the Δm relation.

magnitude difference, Δm, around 0 with nominal spread within 0.5σ, with an intrinsic scatter of ± 0.01 mag for J and, again, about 50% higher for $\mathrm{K_s}$. Exceptions arise, however. For instance, the stars from detector #16 show systematically redder colors in the upper third part of the detector ($Y \gtrsim 1400$), for all images. This is due to a known defect in the CCD with filter-dependent sensitivity. This caveat in described below in §2.3.

2.3 Completeness

The level of completeness of the new photometry is assessed through artificial star experiments. The basic idea is to add to the SDIs synthetic stars with the observed PSF and J and $\mathrm{K_s}$ magnitude spanning the range observed in the data. Then re-process the entire dataset containing the artificial stars of known true magnitudes by following the same procedure described in §2.2. The fraction of recovered stars with respect to those added provides an estimate of the photometric completeness.

In practice, for each detector-side $\mathrm{JK_s}$ catalog, we first define a color-magnitude mask covering almost the whole corresponding CMD. This mask is used to construct a uniform 2D distribution in color-magnitude space, from which we draw pairs that define the J and $\mathrm{K_s}$ magnitude of the injected stars (m^{in} atlas). This allows us to have completeness information virtually on all stars present in the observed CMD with no waste in CPU time.

The artificial stars are then spatially distributed (i.e. XY) around a grid properly customized to avoid artificially increasing the crowding (see Zoccali et al., 2003). Specifically, we use a hexagonal grid with distance between nodes of 30 pixels ($\sim 2\times$PSF radius). Such choice allows us to keep the crowding under control (i.e. similar to the data) and to minimize the number of simulations by optimizing the density of injected stars given the distance restriction. Indeed, with respect to a square grid, the hexagonal one allows for $\sim 15.4\%$ more nodes within the same area.

To obtain a statistically robust completeness function we decided to inject $\sim 120{,}000$ artificial stars per detector-side, which means doubling that quantity per detector. However, given the limitation imposed by the grid, only $\sim 11{,}000$ stars per side can be arranged at the time. Therefore, this process must be repeated 10 times to reach the desired total number of injected stars.

We proceed to randomly assign a $\mathrm{JK_s}$ pair from the m^{in} atlas to every node in the defined XY grid. Because the sides are actually composed of $3 \times N_{epochs}$ SDIs, we use the transformation provided by DAOMASTER in the photometric procedure to properly divide the grid and the associated $\mathrm{JK_s}$ in the constituent SDIs.

This effectively produces a set of injection catalogs with XY $\mathrm{J}^{in}{\mathrm{K_s}}^{in}$ entries, one for each SDI, so that the artificial stars in any one detector-side are coherent (i.e. in the overlapping areas of each SDI pair, the injected stars are in the same absolute position with the same magnitudes). These catalogs are then fed to the ADD subroutine of DAOPHOT, together with the calculated PSF-model from §2.2.2, to produce modified images with the artificial stars injected.

These modified images are then processed in exactly the same way as described in §2.2, with the exception of the coordinate transformations that are recycled from the photometry process, rather than redefined. This produces, for each detector, 2 catalogs $\mathrm{JK_s}$ (left and right).

We note that since the catalogs themselves have joint $\mathrm{JK_s}$, that is, there is no measure in one filter without the other, the final product is a completeness value that is a function of both magnitudes: $p = p(\mathrm{J}, \mathrm{K_s})$.

Finally, side-by-side, we cross-correlate these catalogs to the injection ones using STILTS, with a separation criterion in XY of at most 1.5 pixels (similar to the calibration run), providing us now with a recovered magnitude m^{rec} match to the corresponding m^{in}.

We consider a star as *recovered* if $|m^{in} - m^{rec}| < 0.75\,\mathrm{mag}$ (see Sollima et al., 2007). Thus, the final completeness value $p(\mathrm{J}, \mathrm{K_s})$ is simply defined as the ratio between the number of recovered stars and the number of injected stars per $(\mathrm{J} - \mathrm{K_s}) - \mathrm{K_s}$ bin. Of course, this assumption provides a very good measurement as long as the uncertainties, due to the combination of photometric error and systematics, are within the adopted magnitude and color bin. Here we have decided to use a unique $(\mathrm{J} - \mathrm{K_s}) - \mathrm{K_s}$ bin of $0.14 \times 0.13\,\mathrm{mag}^2$, which turned out to stabilize the uncertainty variation of p itself when moving across the CMD.

We note that the completeness in general is different from one detector to another, with nominal ± 0.2 variations around the $p = 0.5$ level, regardless of actual stellar density.

Finally, in the available technical documentation at the CASU website[6] several known issues are highlighted regarding the VISTA image quality. Most of them are either unavoidable or resolved by the time of the observations, but there are two precautions we thought would be best to take, and that was to not include detectors #4 and #16 in the completeness analysis. In the case of detector #4, the problem is mild and not always present, but we decided to exclude it regardless. For detector #16, however, the defect is persistent and too hard to correct effectively.

2.4 Final photometric catalogs

The final product of the procedure described in the previous sections is a compilation of 196 photometric catalogs, one per each VVV bulge tile, (see Fig.2.2) covering a total of $\sim 300\,\mathrm{deg}^2$ around the Galactic center.

For each star detected in a given tile, the catalog provides: the equatorial and galactic coordinates (RA, DEC, l, b); the magnitudes with the corresponding photometric errors $(\mathrm{J}, \mathrm{K_s}, \sigma_\mathrm{J}, \sigma_{\mathrm{K_s}})$; the completeness value (p(J,$\mathrm{K_s}$)); the extinction ($\mathrm{E(J - K_s)}$, $\sigma_{\mathrm{E(J-K_s)}}$, $\mathrm{A_J}$, $\mathrm{A_{K_s}}$) as derived from the reddening map of Gonzalez et al. (2012); statistics describing the quality of the PSF-fit (sharpness, χ^2); the magnitude *combined errors* $(\Delta\mathrm{J}, \Delta\mathrm{K_s})$; the number of times a particular star was detected (rep); and a binary (i.e. base 2) flag tracing the detector(s) of origin of the entry.

It is worth mentioning that to properly assess the photometric quality of each catalog one should not exclusively use the tabulated photometric errors, but rather the *combined*

---

[6] http://casu.ast.cam.ac.uk/surveys-projects/vista/technical/known-issues

errors that are obtained considering the photometric errors and the uncertainty derived by the repeated and controlled injection of artificial stars. Indeed as we show in Figure 2.7, the combined effect of systematics and photometric uncertainties produces a spread in the recovered vs. injected magnitudes (black solid line) that is considerably larger than what one would expect from the photometric error alone (colored points). In addition, Figure 2.7 evidences the known issue related to the saturation/non-linearity of bright stars in the VVV K_s-band images ($K_s \sim 12$). Of course this problem is also present in the J-band, but the uncertainties up to $J \sim 10$ are well in line with the rest of the profile, from both photometric and simulated sources.

The provided χ^2 and sharpness (s) values can be additionally used to flag and filter out poor and/or false detections from the catalog. The χ^2 refers to the quality of the star PSF-fitting, and its value should be distributed around 1 (i.e. $\chi^2 = 1$ for the *ideal* fit), therefore any considerably deviant value points to a poor fit. The sharpness (s) provides a measurement of how *round* the recovered detection looks in the image. This is a number centered around 0 for perfectly round detections, up to some internally filtered value that usually moves in the (extreme) ranges of $|s| \lesssim 10$. However, $|s| \lesssim 2$ is much more common.

In our analysis, we have adopted a number of *quality filters* that have different properties, fine-tuned to the characteristics of a given catalog tile, but whose common effect is removing the poor and false detections (e.g. stars with either a poor fit, $|\chi| >> 1$, and/or elongated sources in the image, $|s| \gtrsim 1.5$). Such *unlikely stars* appear more evidently as a diffuse feature in the raw CMD, and generally have minimal effect of the global shape of the CMD. Extended sources, such as background distant galaxies, can still pass the photometric internal quality cuts and therefore appear in the final CMD.

The first *quality filter*, and the most effective in nominal (i.e. not very crowded) fields, is obtained in the [J *vs.* s] plane, where we take bins in J and use iterative σ-clipping to get rid of the most deviant s stars per J bin. This usually results in removing a small portion of the stars in the derived CMD, but targeting mostly the outliers in the s distribution.

For the most crowded fields, the former filter is not effective enough because the high star density produces more frequent blending events, which skews the s(J) distribution enough to prevent effective cleaning. For these fields, we use the index $s \times (\chi^2 - 1)$, and produce a 3D histogram of [K_s *vs.* ($J - K_s$) *vs.* $s \times (\chi^2 - 1)$] space, and simply remove the stars within the least populated cubic bins. Removing the lower 1-4% least populated quantiles seems to solve the problem, although with a non-zero removal of *bona fide* stars. However, the removed *true* stars are not particularly concentrated in the CMD, but rather more or less uniformly distributed within the outer CMD contours.

Finally, we stress here that particular care must be paid to ensure that the adopted *quality filters* do not alter the shape of the CMD, and do not remove too many stars in relation to the total numbers, otherwise a non-negligible correction in the completeness estimates of the catalog would become necessary.

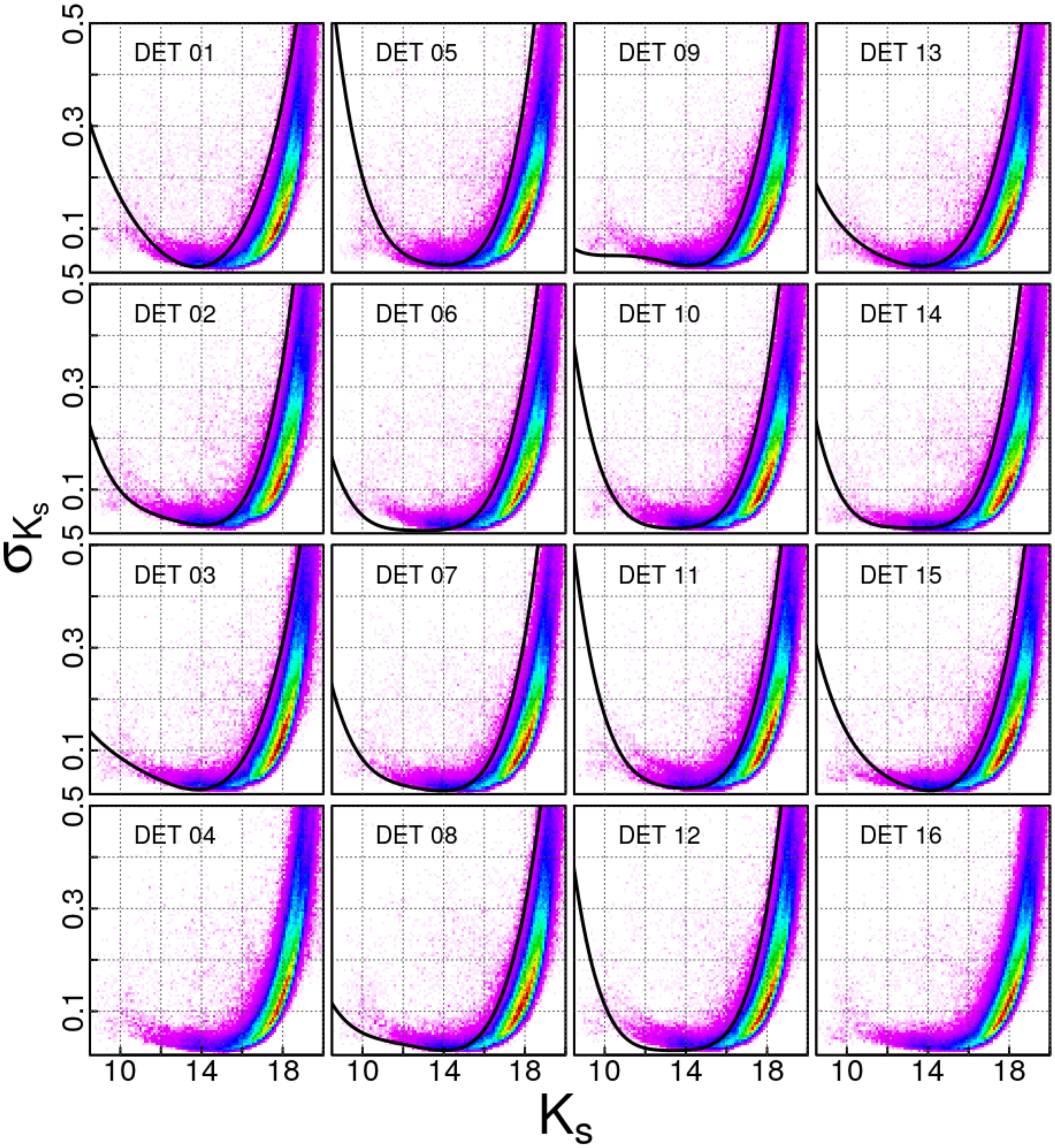

Figure 2.7: Photometric error profile for a sample field. The 2D histogram in each panel displays the $\sigma_{\mathrm{K_s}}$ vs. $\mathrm{K_s}$ distribution of detected stars within a given detector (the detector number is labeled in each panel). Color coded for the density in each 2D histogram, from low (magenta) to very high (dark red) relative densities. The split or broadened sequences are due to the error mitigation in overlapping areas of a side ensemble. Detections in overlapping areas have smaller uncertainty. The black solid line refers to the *combined errors*: $\Delta_{\mathrm{K_s}}$ vs. $\mathrm{K_s}$, as calculated from the completeness experiments (except for detectors #4 and #16, for which no completeness is available).

Table 2.1: Position and average color excess of the tiles sample for which we show the derived CMDs. The total number of detected sources in each tile is also given.

Name	(l, b)	$< E(\mathrm{J}-\mathrm{K_s}) >^a$	Detected stars
b208	$(+1.11°, -9.67°)$	0.058 ± 0.014	1,748,959
b249	$(-0.45°, -6.39°)$	0.151 ± 0.046	2,704,933
b272	$(-7.79°, -4.23°)$	0.389 ± 0.091	2,853,891
b283	$(+8.28°, -4.21°)$	0.253 ± 0.038	3,196,013
b292	$(+0.97°, -3.14°)$	0.333 ± 0.063	4,133,744
b333	$(-0.49°, +0.16°)$	3.236 ± 0.668	2,850,439
b376	$(+0.98°, +3.38°)$	0.888 ± 0.248	3,830,302
b384	$(-7.78°, +4.51°)$	0.249 ± 0.053	3,363,181

[a] Color excess from Gonzalez et al. (2012), average and standard deviation are taken over the whole tile.

2.4.1 Derived Color-Magnitude Diagrams

The entire photometric dataset is very extensive and varied, therefore we show here the derived CMDs and corresponding completeness maps only for a sample of 8 tiles sparsely distributed across the bulge area (see Table 2.1). The fields have been selected such as, through the relative comparison of their CMDs, the reader can easily and quickly appreciate how the quality of the photometry varies along the bulge minor axis or at large longitudes (see Table 2.1) because of the different stellar density and extinction.

Note that, when using standard point-scatter plots, the large number of detected stars in each tiles (routinely 1- 5 million) saturates the plot for $\mathrm{K_s} > 15$, thus preventing us from distinguishing different evolutionary sequences such as the sub-giant branch (SGB) and the MS-TO. Therefore, in this work any CMD is shown as Hess density diagram. In addition, the first *quality filter* described in §2.4 has been used to marginalize the number of poor and false detections, whose severity depends mostly upon the field crowding. The result of this *cleaning* procedure for the 8 selected fields is shown in Figure 2.8.

With the exception of the tile b333, the common features of all CMDs are: the well defined bulge red giant branch (RGB- reddest vertical sequence $\mathrm{K_s} \gtrsim 16$), the bright portion of the main sequence (MS) of the disk (bluest vertical sequence $\mathrm{K_s} \gtrsim 16$), the bulge RC (stellar overdensity along the brightest portion of the bulge RGB and generally between $14 > \mathrm{K_s} > 12$), the brightest end of the evolved disk population (vertical plume departing from the RGB towards the blue in the CMD at $\mathrm{K_s} \lesssim 11$), and the bulge MS that overlaps with the faint portion of the disk MS.

The color spread of all sequences in the bright part of the CMD ($\mathrm{K_s} \gtrsim 16$) is mostly caused by the differential reddening, metallicity spread and distance depth, whereas at faint magnitudes the photometric and systematic errors become predominant, smearing out the color of MS stars over a broad magnitude range. The photometric limit is obviously quite constant ($\mathrm{K_s} \sim 19.5$) within the sample tiles, however as expected because of the different

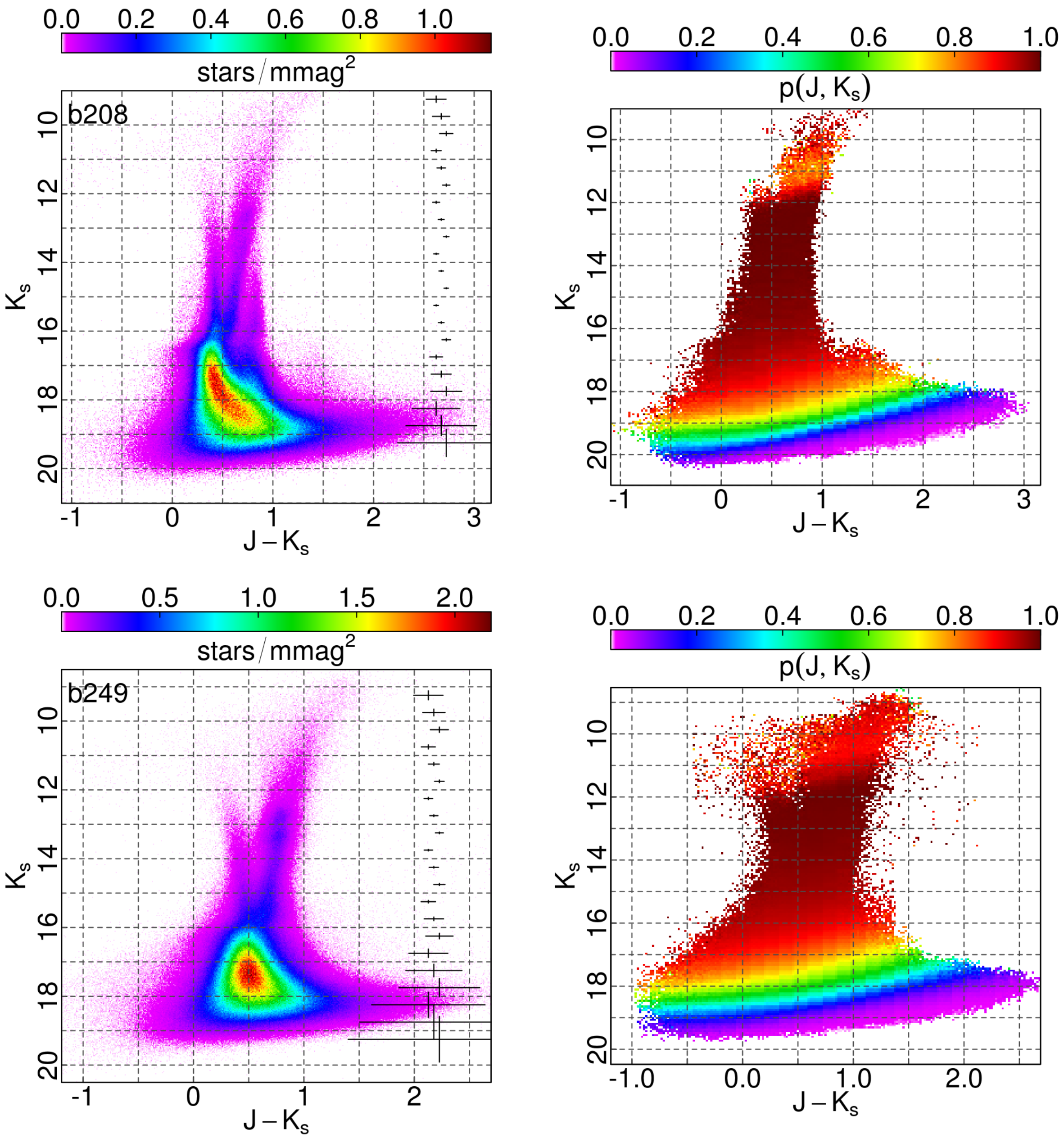

Figure 2.8: Hess diagram of selected fields with typical color and magnitude errors shown as crosses at their respective K_s reference level (left panel), and corresponding photometric completeness map (right panels). The VVV name of the field is labelled in each plot.

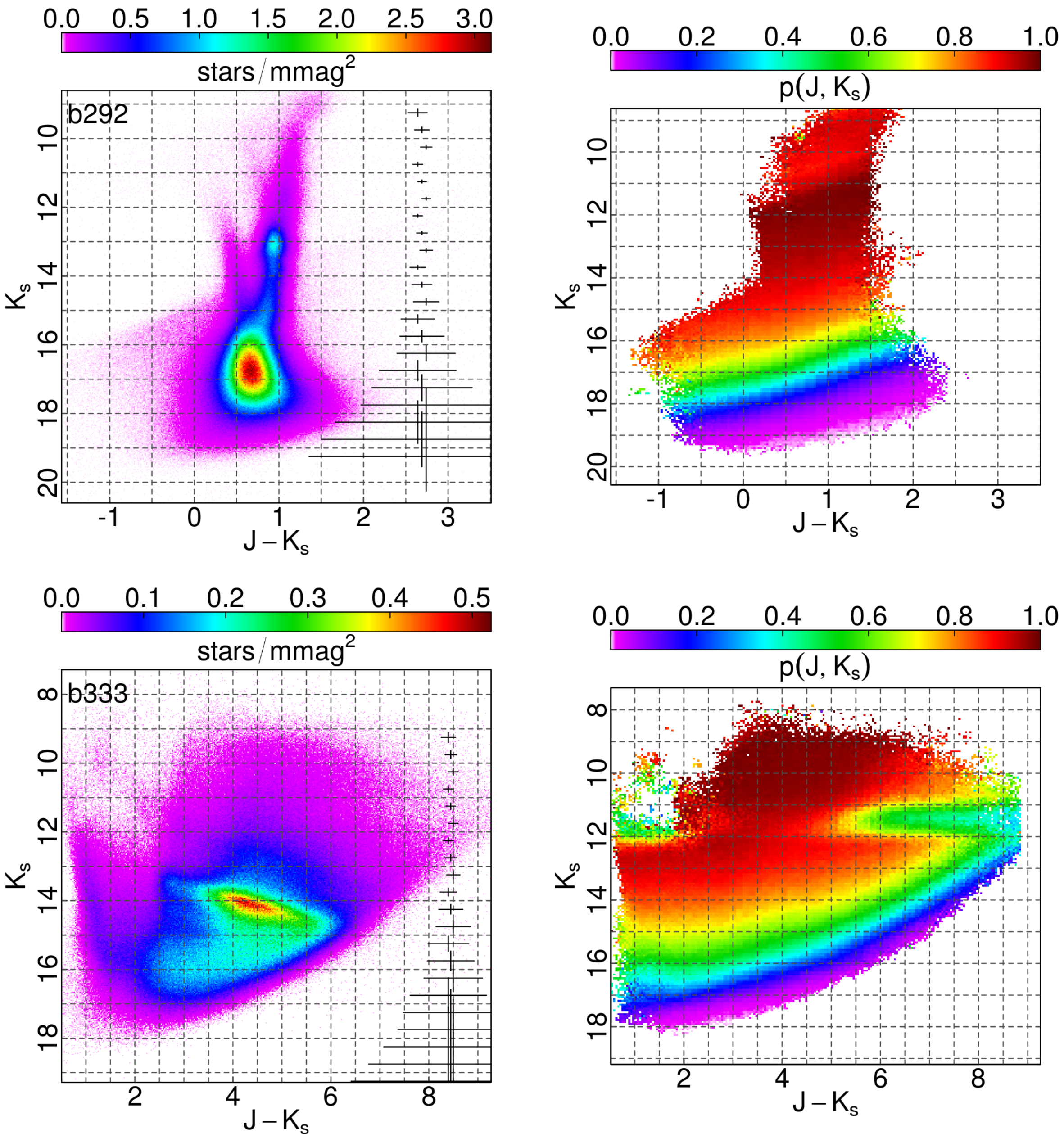

Figure 2.8: (continued)

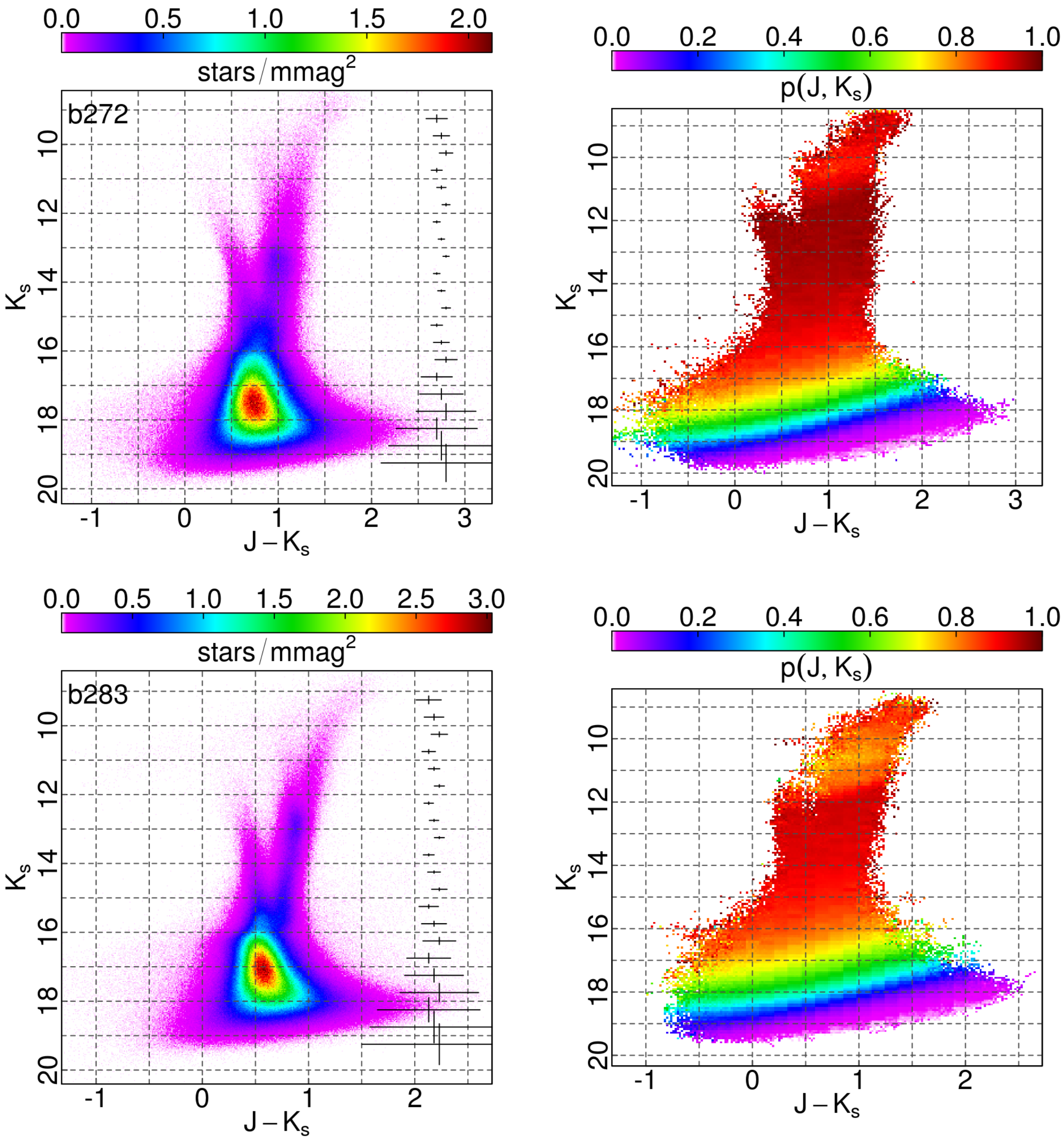

Figure 2.8: (continued)

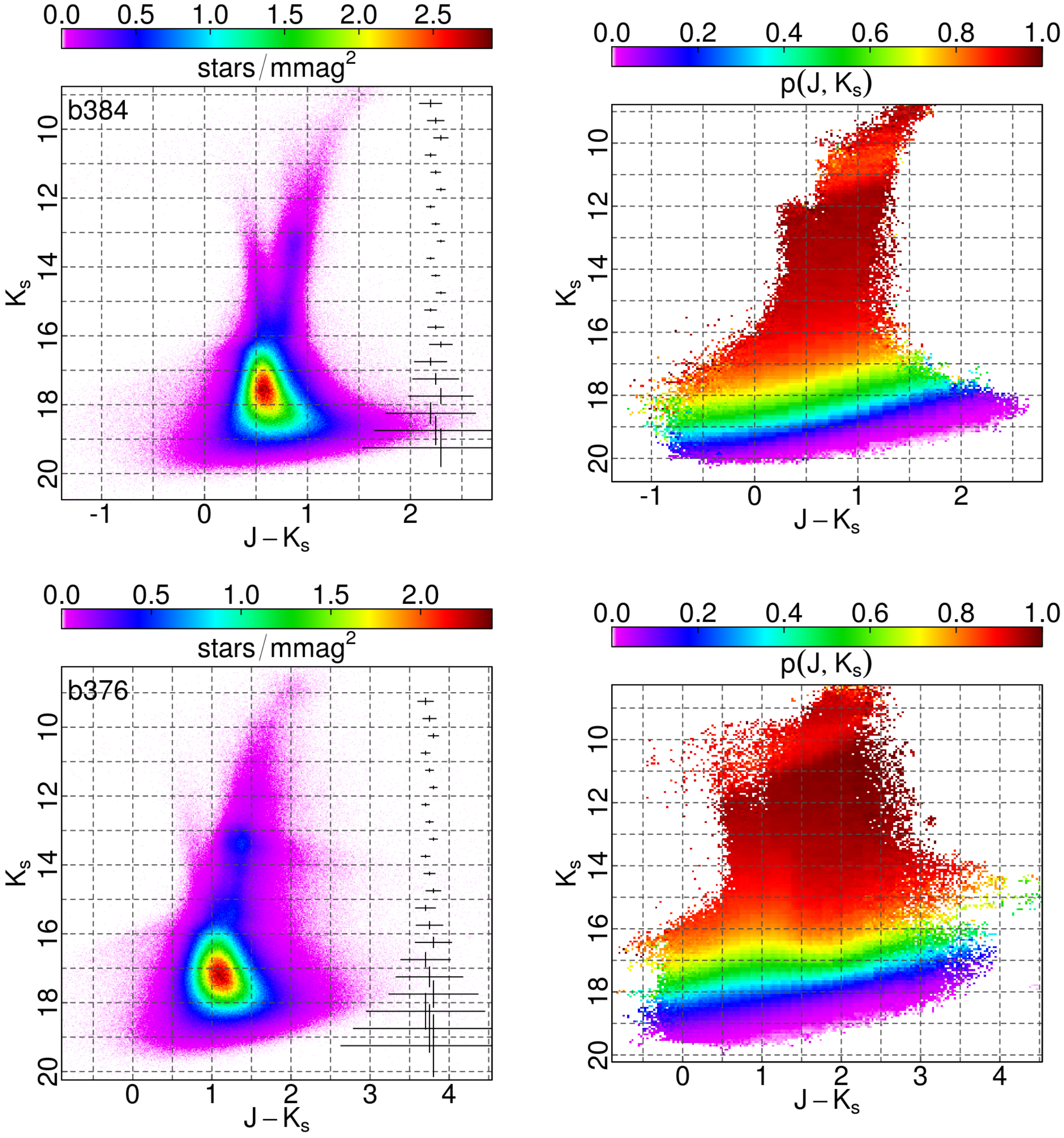

Figure 2.8: (continued)

crowding and extinction, the photometric completeness varies substantially within the fields. The bulge MS-TO is close to the *hot spot*, i.e. most dense area in the Hess diagrams, however due to the superposition of young disk MS and the increasing dispersion, it is impossible to ascertain this evolutionary phase easily. That said, in the subsequent chapters we demonstrate that we can determine the age, and age distribution of bulge population sampled by different tiles, providing that enough attention is paid to the observational effects.

The fields b208, b249 and b333 deserve special attention because, given their location, the derived CMDs show peculiar features. Specifically, in the CMD of b208 one can identify the local K and M dwarf sequence as the vertical plume ($\mathrm{K_s} \gtrsim 16, (\mathrm{J}-\mathrm{K_s}) \sim 0.8$), redder than the bright disk MS and bulge RGB. This sequence is usually only evident in the outskirts of the bulge area, at very large heights from the plane (i.e. $b \lesssim -8°$, see also Saito et al., 2012b). Moving towards the center, because of increasing reddening and stellar density, the local dwarf sequence progressively fades away and is *swallowed* by the bulge RGB.

Tile b249 is particularly interesting because is located in the region where the X-shape of the bulge (see §1.1) is clearly evident. Indeed, from the derived CMD one can observe the presence of 2 well separated RC (i.e. two apparent overdensities along the RGB at $\mathrm{K_s} \sim 12.9$ and $\mathrm{K_s} \sim 13.2$), which are the signatures of two southern arms of the X-shape structure crossing the line-of-sight.

Tile b333 is also peculiar because it is located on the Galactic center region, and as such it is the most heavily reddened field in our sample (i.e. $\mathrm{A_{K_s}} > 5$, Gonzalez et al., 2012). The derived CMD is the shallowest in the sample, and barely covers the entire RC population with a 50% completeness level. However, because the large extinction affects only the bulge, the blue plume corresponding to the intervening evolved disk stars is clearly traceable in the CMD (see vertical sequence in the range $1 \lesssim (\mathrm{J}-\mathrm{K_s}) \lesssim 2.5$ and $8 \lesssim \mathrm{K_s} \lesssim 12$). In this respect, for studies of the evolved disk populations along the bulge line-of-sight, the innermost tiles affected by large reddening are ideal because the bulge-disk separation is quite clear.

2.5 Overview of the global photometry

Containing nearly 600 millions stars, the whole new photometry represents one of the most accurate and complete census of the evolved and un-evolved stellar population in the Milky Way bulge.

As such this photometric database represents a treasure trove for the whole community, enabling different studies beyond those described in this thesis. This is the reason why we decided to make all catalogs available for download at the CASU website, along with a set of figures (i.e completeness map, stellar density map, Hess diagram) that describe the main properties of the entire photometric compilation, and at the same time provide a quick look at the global bulge morphology and stellar content.

In Figure 2.9 we provide an overview of the global photometric completeness as a

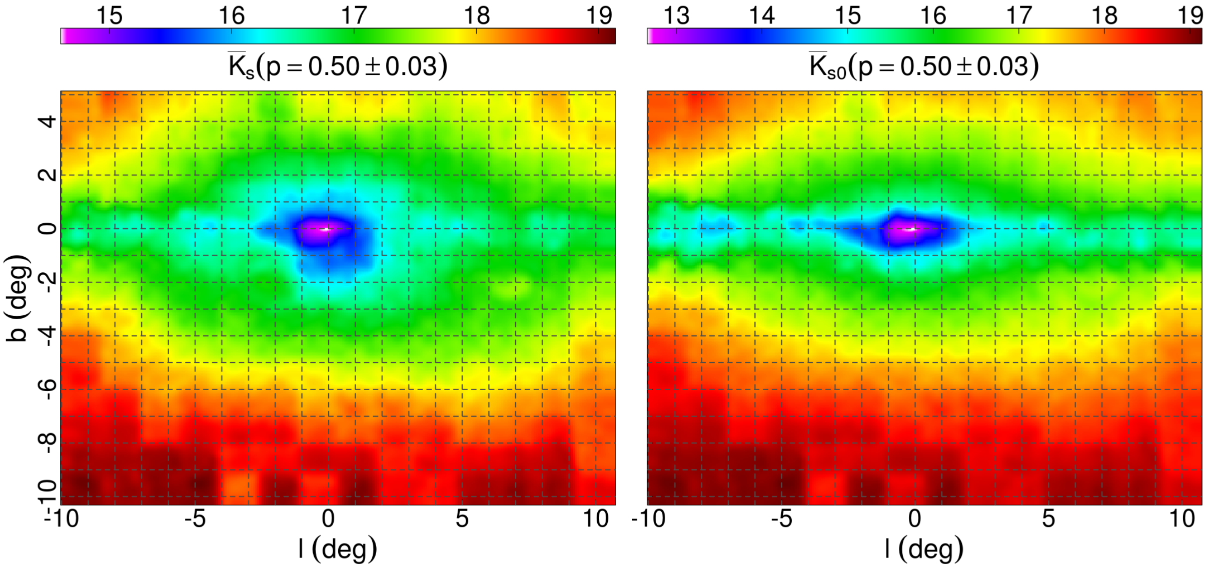

Figure 2.9: Observed mean K_s (left panel) and reddening-corrected K_{s0} magnitude of stars with ∼50% completeness level ($p = 0.50 \pm 0.03$) across the whole bulge area studied in this work.

function of the position within the bulge, in the form of the mean K_s and K_{s0} (K_s corrected by extinction from Gonzalez et al., 2012) magnitudes of the stars at $50 \pm 3\%$ completeness level. By providing a global view of the photometric quality as a function of the star magnitude and position, the maps in Figure 2.9 help to quickly understand the potential and usefulness of the photometry according to the type of studies that one is interested in.

For instance, in this work we need a good sampling of the old MS-TO region in the observed CMDs. We know that for a 10 Gyr old population of solar metallicity, and at the distance of the bulge, the MS-TO is expected at $K_{s0} \sim 17$. Therefore, by looking at the reddening-corrected completeness map (Figure 2.9, right panel), we can quickly assert that, with some exceptions at $l = \pm 10^\circ$, any field within $|b| \lesssim 3.5^\circ$ is likely not complete enough for stellar dating. Therefore, we should either discard or treat with particular caution any results derived from such regions. On the other hand, if the science goal is to study and make a census of the RC or bright RGB populations ($K_s < 14$), then the photometric catalogs of all but the most central two tiles of the bulge are adequate.

As expected the overall completeness of the derived photometry increases when moving from the center outwards because of the decreasing extinction and stellar density (i.e. confusion). In fact, the silhouette of the bulge emerging from the completeness map closely resembles the boxy-peanut shape that is pictured in the stellar maps shown in Figure 2.10. Some Galactic globular clusters located in the VVV area reveal themselves in Figure 2.10 as blue and cyan small dots because of their locally higher stellar density.

To provide a global and quick view of the stellar content within the VVV area, in Figure 2.11 we show the CMD obtained by stacking together all 196 tiles. In the $[K_s vs (J - K_s)]$ plane (left panel of Figure 2.11) the effect of the large reddening is clearly evident,

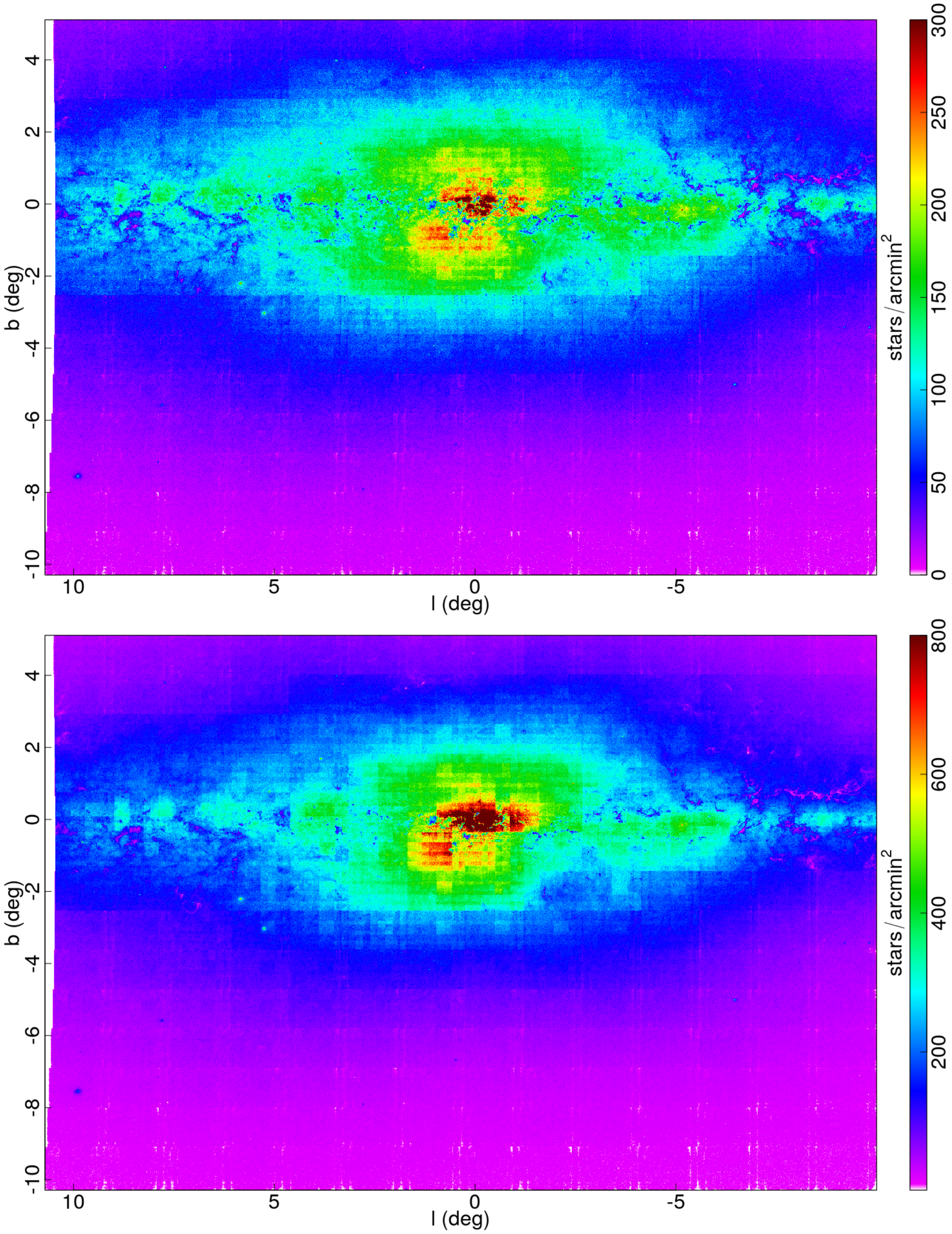

Figure 2.10: Stellar density map of the whole bulge area as derived by counting all stars with $K_s < 16$ (top panel), and by correcting the star counts for completeness on a detector-by-detector basis (bottom panel). In the cases of detectors #4 and #16, we have used the mean completeness of the tile as a general value for all stars within them (see text).

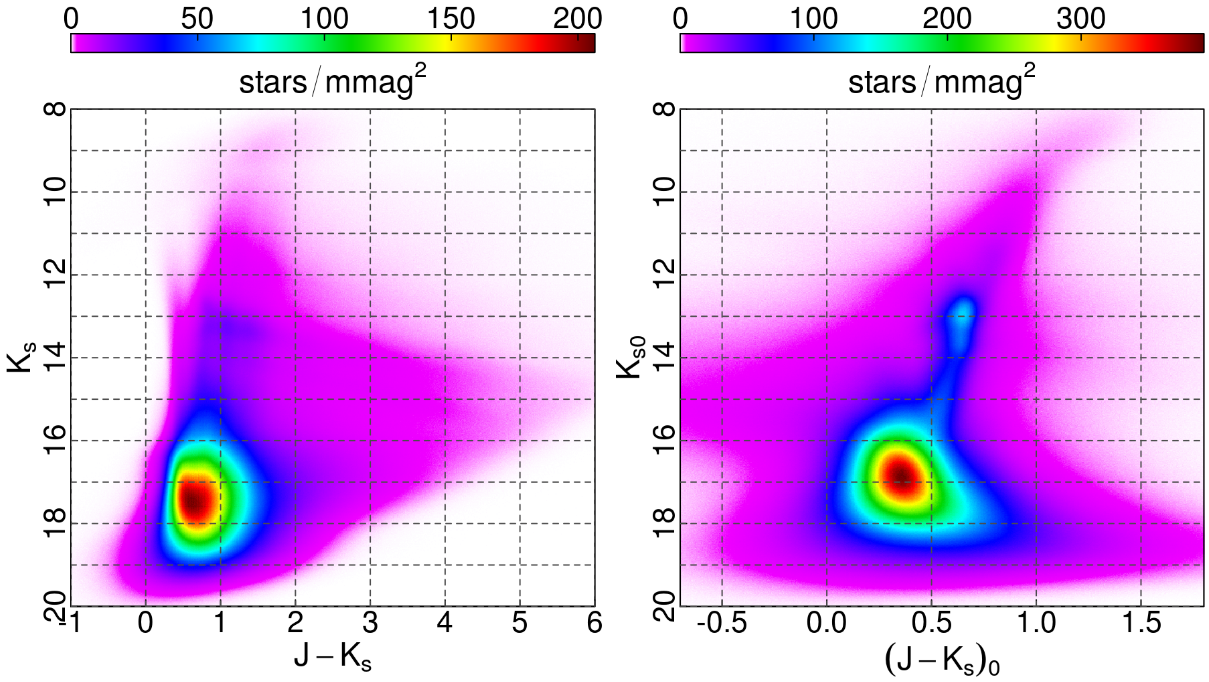

Figure 2.11: Hess diagram of all 196 tiles stacked together in the observed $[\mathrm{K_s}, \mathrm{J}-\mathrm{K_s}]$ plane (left panel), and de-reddened $[\mathrm{K_{s0}}, (\mathrm{J}-\mathrm{K_s})_0]$ plane (right panel) by using Gonzalez et al. (2012) color-excess map and (Nishiyama et al., 2009) extinction law (right). The CMDs comprise nearly 600 million stars.

smearing the stars' color over a huge magnitude range (i.e. $-1 \lesssim (\mathrm{J}-\mathrm{K_s}) \lesssim 6$), and making the RGB and RC sequences very blurred and hard to identify. On the other hand, when we correct the photometry by using the Gonzalez et al. (2012) reddening map and the extinction law from Nishiyama et al. (2009) (i.e. $\mathrm{A_J} = 1.526\mathrm{E}(\mathrm{J}-\mathrm{K_s})$ and $\mathrm{A_{K_s}} = 0.528E(\mathrm{J}-\mathrm{K_s})$, shown in right panel of Figure 2.11) the sequences of the evolved bulge stellar populations stand out clearly. We note that the color spread in the blue part of the CMD at $\mathrm{K_s} \lesssim 16$ is somehow artificial because it is the result of applying the bulge extinction correction to the bright MS disk stars along the line-of-sight that, unlike background bulge stars, are not affected by such high reddening. In other words, the large extinction is confined within the bulge only, and not between us and the disk.

Finally, we reckon that because of the large differential extinction and distance depth, for detailed study of the stellar populations along the bulge line-of-sight one should not use Figure 2.11, but instead consider smaller CMDs obtained within smaller sub-regions.

2.6 Tracing the RC distribution

With accurate PSF photometry in hand, we can now properly trace the RC population across the whole VVV area. This is a rather crucial piece of information because RCs are useful standard candles and their distribution in the near-IR CMD plane can be safely used as anchor when comparing CMDs of different fields and observations vs. models.

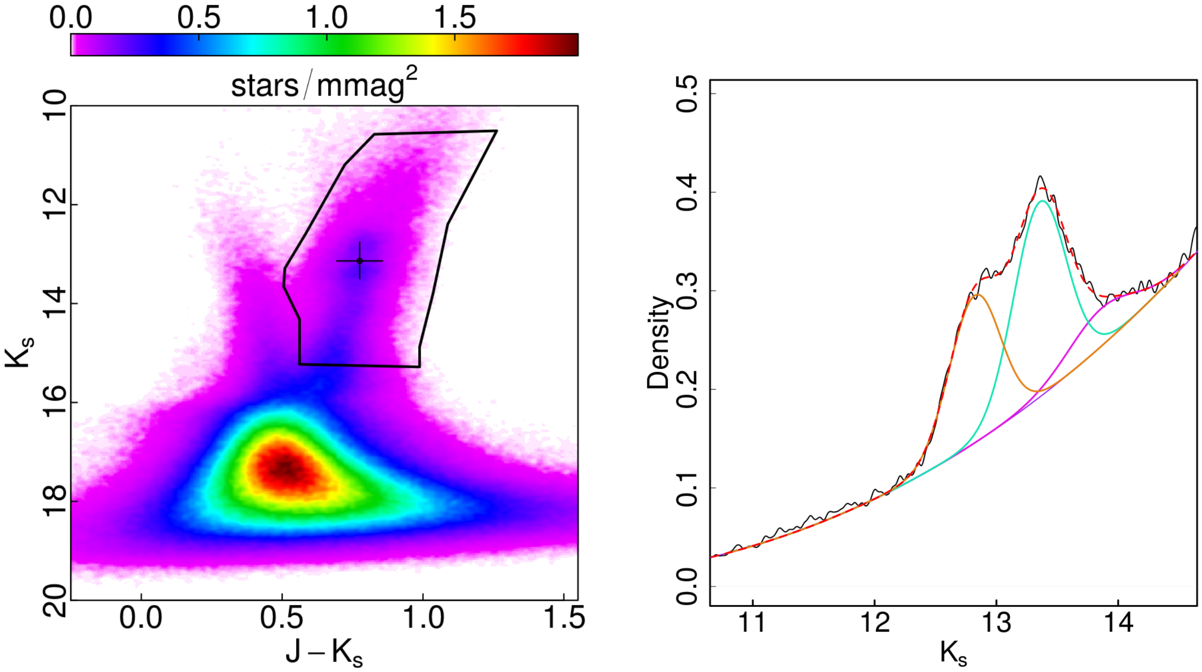

Figure 2.12: Example of the procedure adopted throughout this work to trace the RC distribution, for a typical field where the X-shape of the bulge is detected (see text). *Left panel:* observed Hess diagram of b249 tile, with a black polygon acting as the selection window used to isolate RC and RGB stars, and to construct the corresponding luminosity function reported in the right panel. The black cross shows the final estimate of the mean RC position, together with its effective width in color and magnitude. *Right panel:* kernel estimate of the selected RC and RGB luminosity function (black solid line). Also plotted are the fit to the RGB distribution (violet line), and three gaussian components used to fit the RCs (apricot and cyan) and RGB-bump (magenta). The global fit using all components is shown as dashed red line. In this example, the mean and σ of the gaussians component are: $K_s = 12.82 \pm 0.21$ mag, 13.36 ± 0.22 mag, for the RC, and 13.86 ± 0.28 mag for the RGB-bump.

We start by making an educated color-magnitude cut in the CMD such as to enclose evolved stars only (e.g. RGB, and RC) down to the magnitude and color levels where their sequence is still distinguishable from the bright MS of the disk (see left panel in Figure 2.12). Then we estimate the K_s-magnitude star density (i.e. very similar to luminosity function histogram, but without depending on the arbitrary choice of a starting bin position) with a narrow enough gaussian kernel as to not introduce extra dispersion. We fit the so--derived luminosity function with a 4^{th}-degree polynomial by excluding the magnitude region around the RC. By subtracting the fit to the RC region, the residual corresponds to the distribution of RC and RGB-bump stars only. Finally, to trace the RC population in term of mean magnitude and star counts we fit the residual with gaussians (see right panel in Figure 2.12).

Because of the bulge X-shape, we know that some fields ($|b| > 4°, |l| \lesssim 4°$) show a prominent bimodality in the RC profiles, therefore in those regions we have opted to use at least 3 gaussians to fit the RC profile: two for the RC and one for the RGB-bump. It is worth mentioning that in principle, in the fields showing the split of the RC we should expect also 2 RGB-bumps. However, because the luminosity of RGB-bump corresponding to the brightest RC (i.e. the southern arm of the X-shape closer to us) overlaps with the luminosity range spanned by the second and fainter RC, its detection is usually very hard, and a proper characterization is impossible. Here we remind the reader that, indeed, the RGB-bump is much less populated than the RC.

In general, we have a set of $n+1$ gaussians, where n is the number of RC components. Even though we can (and will) treat each individual RC component as a tracer for its own population (i.e. two populations set a few kpc apart), most of the time we will need a single set of $\mathrm{JK_s}$ RC values to match overall distances over different fields. For this we combine the individual measurements into a global RC. Each RC gaussian has a centroid μ_i, a variance σ_i^2 and a scale a_i. Therefore, the $\mathrm{K_s}$ magnitude of the global RC position is given by:

$$\mathrm{K_s^{RC}} = \sum_{i=1}^{n} \mu_i a_i \tag{2.1}$$

Where we have set $\sum\limits_{i=1}^{n} a_i = 1$. For the global RC color, we define a weight for the N stars within the selection area as:

$$\omega_k = \sum_{i=1}^{n} a_i \Phi(\mathrm{K_{s}}_k, \mu_i, \sigma_i^2) \tag{2.2}$$

Where $\Phi(x, \mu, \sigma^2)$ defines the normal distribution density function of mean μ and variance σ^2 at position x. At last, the global color of the RC is defined as:

$$(\mathrm{J}-\mathrm{K_s})^{RC} = \sum_{k=1}^{N} (\mathrm{J}-\mathrm{K_s})_k \omega_k \tag{2.3}$$

Where, once again, we have set $\sum\limits_{k=1}^{N} \omega_k = 1$.

It is important to note, that this approach necessarily implies a contamination from RGB stars when estimating the RC color. However, the effect of the interlopers is negligible for the vast majority of the fields because the high stellar density makes easier to identify the sequences. On the other hand, it can be quite significant in the peripheral fields (i.e.

$b \lesssim -6°$) where the bulge stellar density drops drastically (see maps in Figures 2.10 and 2.13). Nevertheless, the natural alignment between RC and RGB alleviates the error in this estimator.

Finally, to provide an example of the possible uses of the RCs, enabling the study of the global bulge structure and morphology, in Figure 2.13 we show the stellar density map as derived by combining the RC distribution from Valenti et al. (2016) (for the region $|b| \leq 4°$) and from this study (for the outer regions). In this case, the RC stars are used as tracers of the intermediate-to-old population, that should exclude most of the disk contamination, effectively producing a map that traces instead the density of stars in the bulge alone.

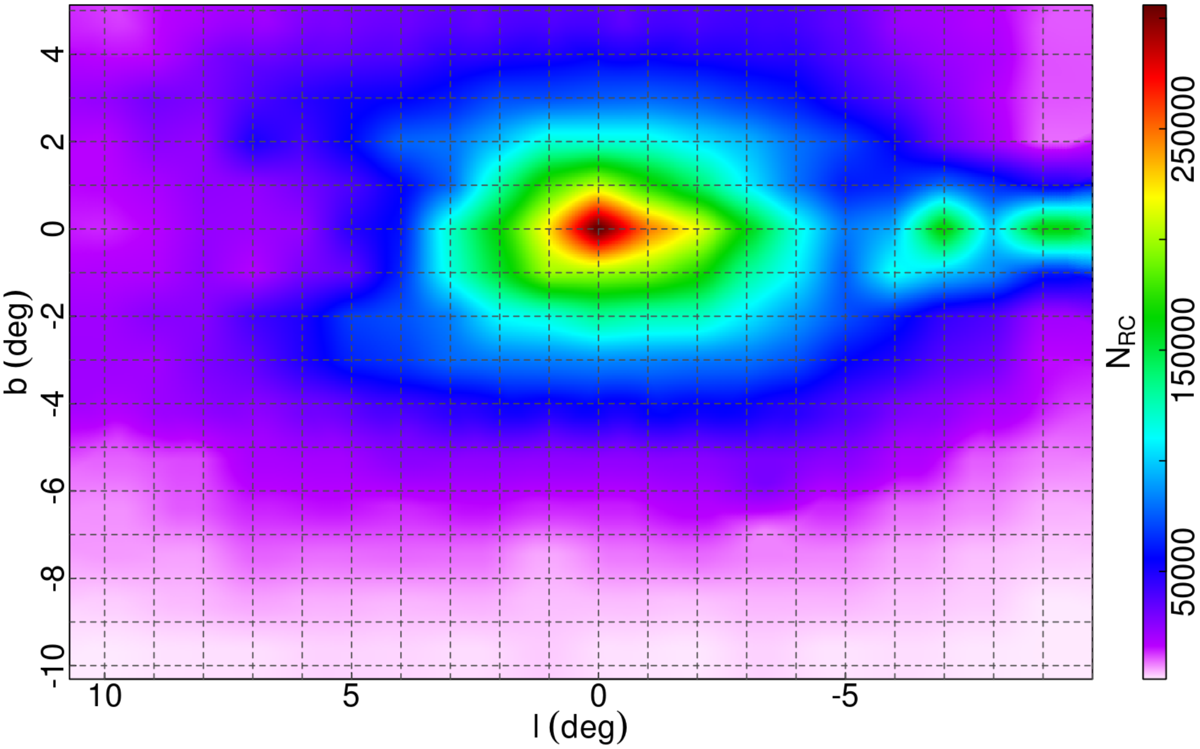

Figure 2.13: Density map in the Galactic longitude-latitude plane based on RC star counts. Star counts for the region at $|b| \leq 4°$ are taken from Valenti et al. (2016), whereas from this study for the outer region.

2.7 A new bulge extinction map

As repeatedly mentioned, in this study we use the extinction map from Gonzalez et al. (2012), which has been found to be accurate enough to study the fields located in regions at $|b| > 3°$. However, while inspecting the extinction corrected CMD of some fields at lower heights from the Galactic plane, we noticed some odd features suggesting a possible underestimation of the extinction. Here, we briefly note that Gonzalez et al. (2012) derived the color excess map from the RC distribution as traced in the VVV area by using aperture-photometry based catalogs for regions at $|b| > 3°$, and for the inner regions a set of PSF-fitting catalogs obtained with DoPhot software (Alonso-García et al., 2018). In regions characterized by large reddening and stellar density, the crowding may contribute to blending signals of the RC, thus resulting in a wrong determination of the extinction.

To check this hypothesis, possibly caused by a limitation of the method used by Gonzalez et al. (2012) in such regions, we decided to estimate the color excess by using a slightly different approach that takes full advantage of the superior accuracy and depth of this work's photometry. The new approach does not exclusively rely on the RC profiles detected in all tiles, but rather exploits the fact that in the near-IR plane the RC and RGB sequences overlap in color (i.e. they are practically *vertically* aligned).

Specifically, on each observed CMD we identify a region where we find both RC and RGB components. In the CMD, we then create a selection window by extending this region towards redder colors and fainter magnitudes following the reddening vector, which here has been defined by using the extinction law of Nishiyama et al. (2009) ($\mathrm{A_J} = 1.526\mathrm{E(J-K_s)}$ and $\mathrm{A_{K_s}} = 0.528E(\mathrm{J-K_s})$). We then define an auxiliary catalog consisting of only stars enclosed in the selection window. From the auxiliary, we pick a random subsample of stars that is $1/30^{\mathrm{th}}$ of the original, and use the stars (l, b) coordinates to create a Voronoi tesselation (following an euclidean metric approximation $dl^2 + db^2 = 0$), using convex (l, b) hull of the complete catalog as the outer boundary. This results in a division of the (l, b) plane that follows roughly the stellar density in the auxiliary catalog (i.e. the higher the local stellar density is, the smaller the area of the polygons). On average each Voronoi tile includes ~ 30 stars, for which we calculate the median color with a 3-MAD clip (adjusted median absolute deviation, so that for a normal distribution, 1-MAD equals $1\text{-}\sigma$), and then assign this value as the *statistic color* of the Voronoi tile area. For a given VVV field, this method produces a tesselation of the sky area covered by the auxiliary catalog in up to 12,500 tiles (this limit to prevent excessive CPU time usage), each one with its *statistic color*.

We repeat the procedure, from the random sampling of the auxiliary onward, about 600 times, such as each iteration produces a different tesselation with different values of the *statistic color*. Due to the random nature of the pick, we can expect each of these tesselations to have roughly the same properties (e.g. number of stars per tile), thus allowing us to combine them by a simple average to finally obtain a *mean* median color map. Indeed, if there exists a correlation of (l, b) position with color, then it should be reconstructed in the end, with a probe that is comparable to the local stellar density of the auxiliary. Also, by using the color as the proxy for extinction, we take advantage of its higher sensitivity compared to $\mathrm{K_s}$ magnitude alone (i.e. $\mathrm{A_J\text{-}A_{K_s}} = 0.998$ vs. $\mathrm{A_{K_s}} = 0.528$).

The final, and very important step of the whole procedure, is the calibration of the so-derived map in order to convert this statistic color into a proper color excess, $\mathrm{E(J-K_s)}$. As a first approximation, we simply take the difference between Gonzalez et al. (2012) and these mean median color maps, and apply the corresponding additive correction. For the low-to-mid extinction fields this calibration works well, however when applied to central areas (i.e. $|b| \lesssim 2°$) where the absolute and differential extinction are higher, the *local* differences between the two maps are too large. To account for these complicated fields, we decide to use the difference in the RC color determination (as derived by using the method described in §2.6) in the CMDs corrected with Gonzalez et al. (2012) and this new extinction map, for a few fields where both maps still have some general agreement, but allowing for some difference between the two. We recognize that this calibration approach is equally subjected to uncertainties, especially given that foreground disk stars have a different reddening than the bulge population. However, we consider that making the RC coincide in the corrected CMDs is a good enough approximation to properly calibrate the map, as it would produce the final result that the CMDs corrected with Gonzalez et al. (2012) map and the new one, would align at the RC level.

In Figure 2.14 we use the VVV tile b331 as an example to show the selection window, and the resulting CMD when the extinction correction is performed by using the new map. Moreover, a direct comparison of the two maps in the b331 region is also provided to show the superiority of the new map.

In Figure 2.15 we show one of the most extreme discrepancies between Gonzalez et al. (2012) and this map, as well as the difference in the dereddened CMDs when the two maps are used. The new map does not only have a higher spatial resolution, but it appears to better representing the higher-extinction areas of the local map. This is supported by the similar but more compact appearance of the RC distribution in the CMD corrected for the new extinction values.

Finally, the complete extinction map derived for the whole VVV area is shown in Figure 2.16. Its spatial resolution goes from $\sim 2'$ in the peripheral fields down to $\sim 0.3'$ near the Galactic plane. However, it is worth mentioning that the high limit in resolution is mostly due to the constraints imposed on the Voronoi tile number (see above), and it is driven exclusively by the need to keep this calculation within schedule. Therefore, in the future the resolution can be further improved if needed.

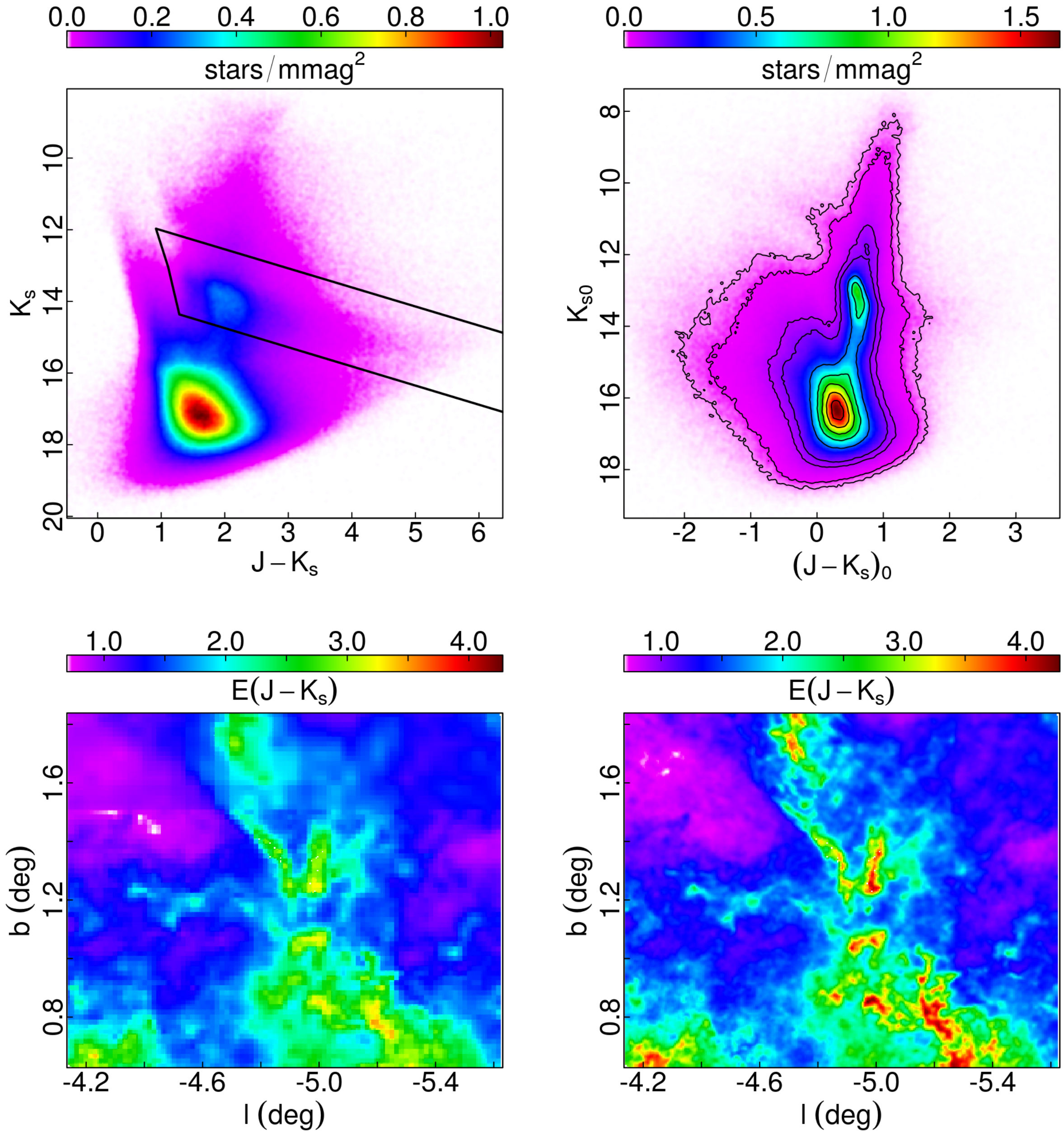

Figure 2.14: Four panels plot exemplifying the adopted procedure to map the color excess for the case of b331 tile. *Upper left*: Observed CMD with the auxiliary selection window (solid black lines) used to derive the color excess (see text). *Upper right*: De-reddened CMD using the new extinction map. Solid black contours are isodensity curves spaced by 1%, 5% and then from 1/12 to 11/12 of the maximum density, in steps of 1/6. *Lower left*: Color excess map for the b331 tile from Gonzalez et al. (2012). *Lower right*: Color excess map for the b331 tile as derived by the method in §2.7.

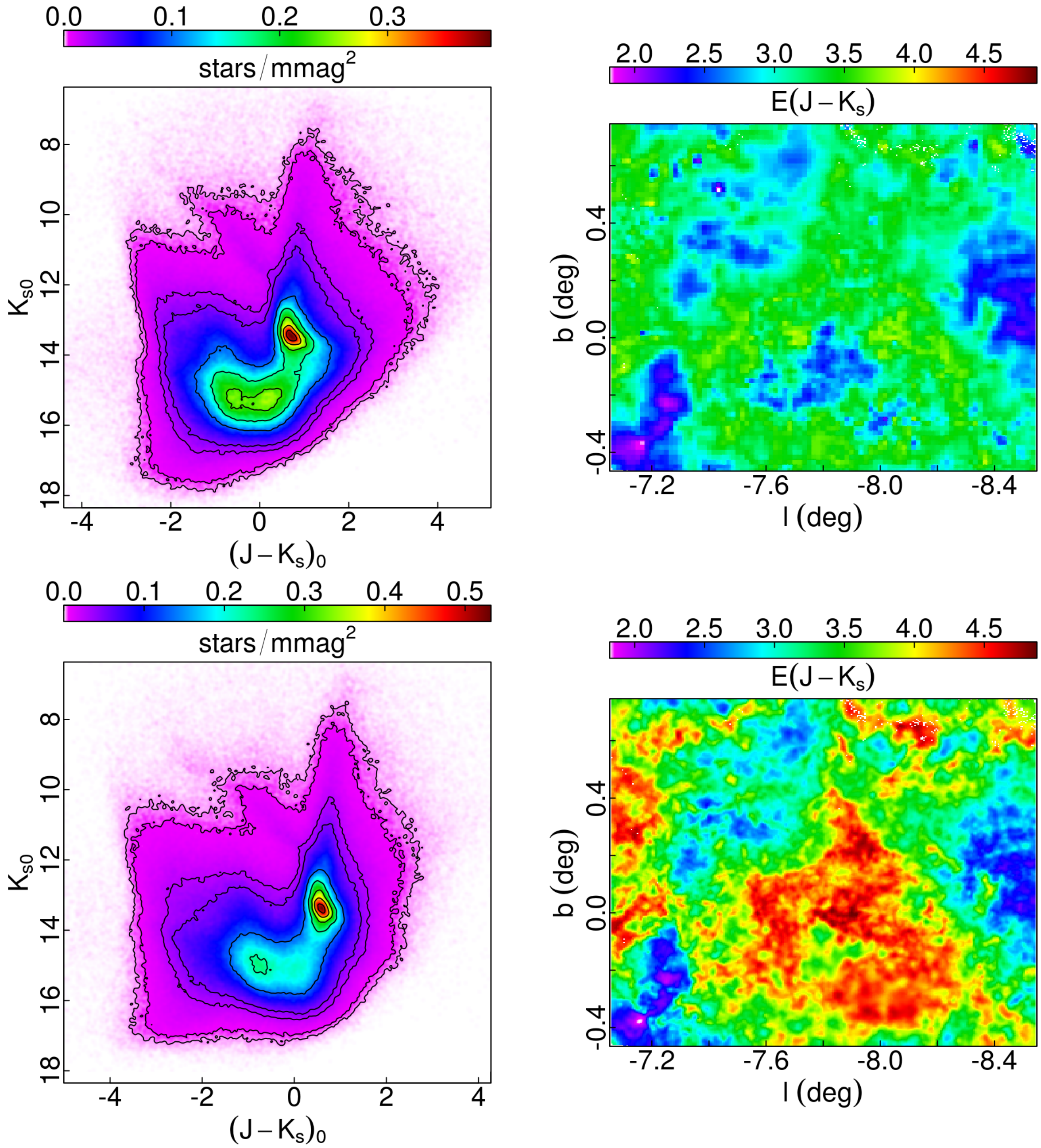

Figure 2.15: Four panels plot showing the comparison of Gonzalez et al. (2012) map and of this work for the b328 field, arguably the most prominent discrepancy in the dataset. *Upper panels:* De-reddened CMD (left) by using the extinction map (right) from Gonzalez et al. (2012). *Lower panels:* Same as in upper panels, but using the color excess map derived in this study. Black contours as in Figure 2.14.

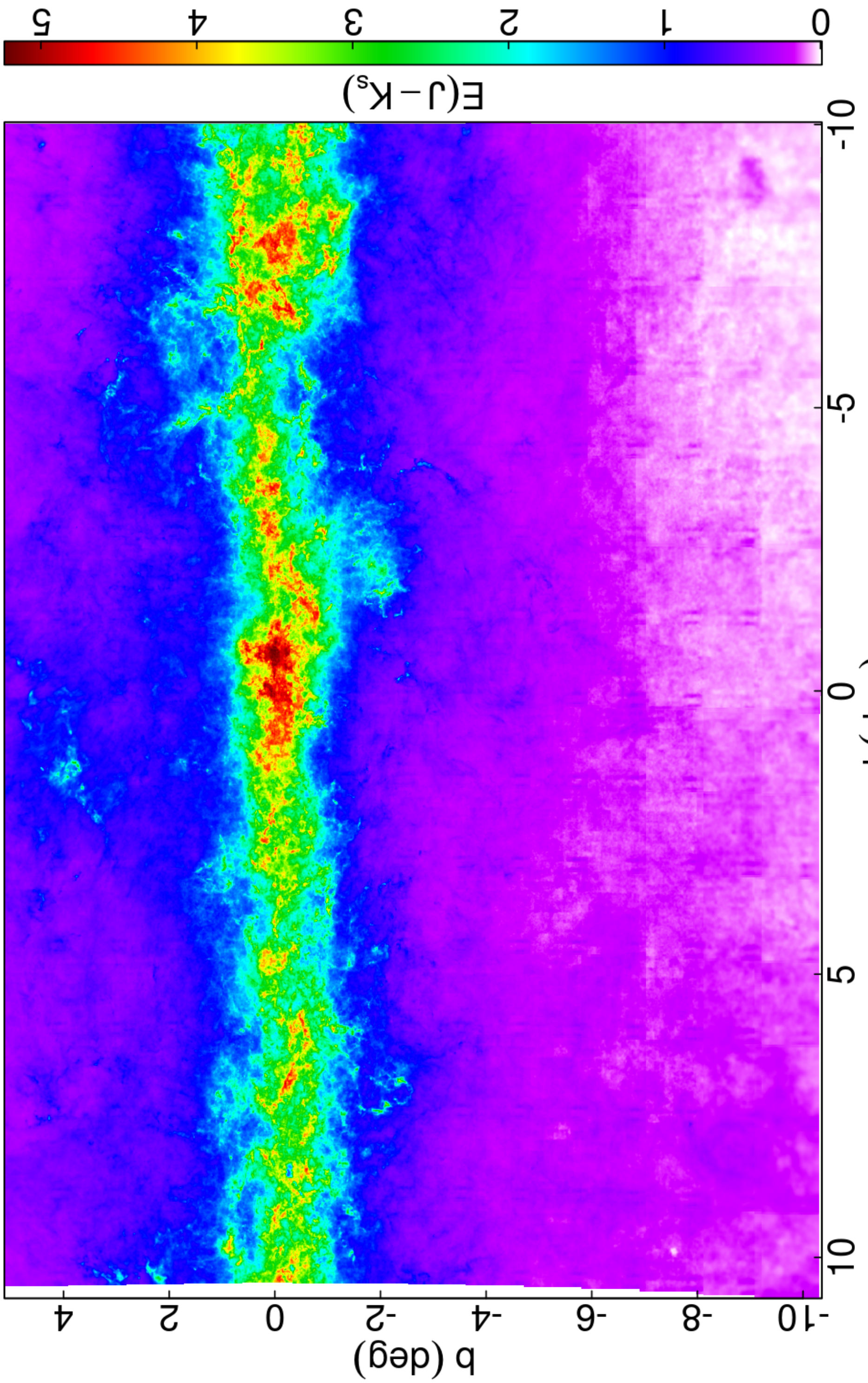

Figure 2.16: Color excess map derived in this work for the whole VVV bulge area. This is mostly in agreement with Gonzalez et al. (2012), with the exception of the high extintion areas. Also, this map has ∼10× higher resolution. However, note the recurring twin line features, especially evident in the low extinction fields ($b < -7°$ and $l < 0°$) where it can be seen as an evenly spaced artifact of slightly increased color excess; this comes from detector #16, which has already been flagged as unreliable in §2.4.

Chapter 3

The bulge clean sample

In this chapter, I describe the method used to decontaminate the observed CMD from foreground disk population by using an independent set of disk fields, which serve as control sample of the disk population. I make a concrete example of one of the fields in the new photometry. The content of this chapter is equivalent to the publication Surot et al. (2018a, submitted).

3.1 Sample- and control-fields

The bulge photometry for a field at $(0°, -6°)$ (b249) has been selected from the new VVV catalogs compilation to serve as a concrete example for the procedure we will be using for the foreground disk decontamination. In addition, 8 disk fields with latitudes in the range $-8° < b < +4°$, and longitude $-30°$ and $+20°$ were observed in Service Mode as part of the programme 095.B-0368(A) (PI: Valenti) by using exactly the same VVV observing strategy. These are the disk control-fields. Their multiplicity, as well as their distribution in the sky is to provide adequate coverage along the minor axis of the disk CMDs, which we expect to vary with distance to the Galactic plane, as well as to have a set at different longitudes where we, of course, we expect no bulge to be present. The variations between control-field CMDs may come from different reddening, population mixtures, geometric distances, stellar densities, etc; we cannot discern the specific reason, but we assume them to be sufficiently similar to the disk population in one of the bulge fields to serve as a representative disk CMD. The control-field images are processed in the exact same way as the main dataset (see Chapter 2), producing photometric $\mathrm{JK_s}$ catalogs for each one, with a corresponding simulation atlas to construct their completeness functions.

In Table 3.1 we list these fields along with their central coordinates, number of detected stars and an estimate of the global color excess from Gonzalez et al. (2012) for b249, and from a new map derived as described in §2.7 for the control-fields.

The simulations show that the photometric catalogs of b249 and the disk control-fields are more than 50% complete above $\mathrm{J} \sim 18.5$ and $\mathrm{K_s} \sim 18$ (see top-right panel of Figure 3.1, and right panels of Figure 3.2). This is a rather important fact, because we expect the old

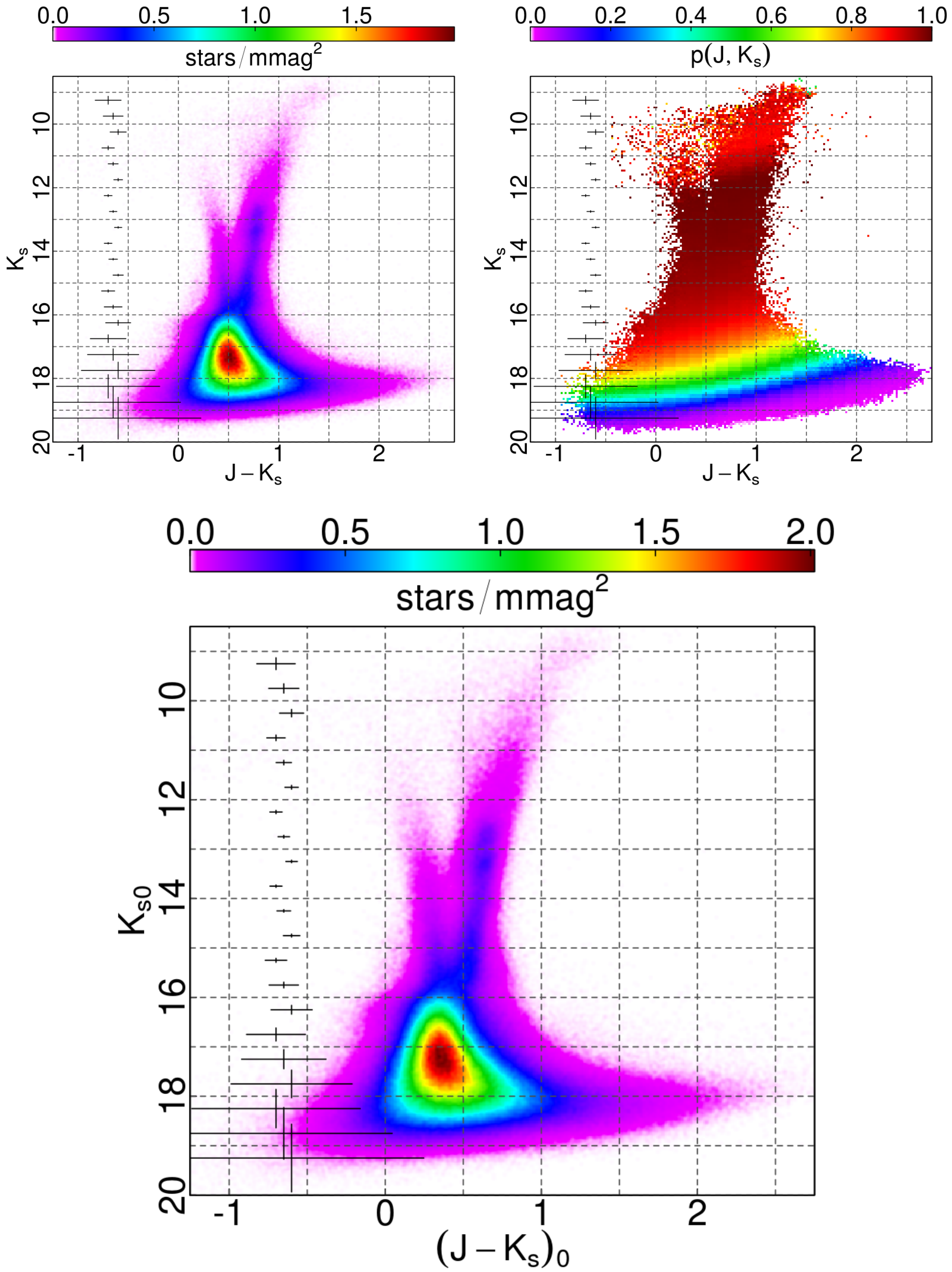

Figure 3.1: Observed CMDs of the VVV field b249 (top-left) shown as a Hess density diagram, with the corresponding photometric completeness map (top-right) as detailed in Section 3.1. Bottom panel shows the reddening-corrected CMD of the same field using Gonzalez et al. (2012) color excess map and Nishiyama et al. (2009) extinction law. Typical color and magnitude errors are shown as crosses at their respective reference K_s level in all cases.

Table 3.1: Example bulge and disk control-fields. Provided are their central coordinates, their average color excess and related standard deviation, as well as the total number of detected stars per catalog. Color excess values are from Gonzalez et al. (2012) for the bulge field and §2.7 for the disk fields.

Name	(l, b)	$< E(\mathrm{J}-\mathrm{K_s}) >^a$	Detected stars
b249	$(-0.45°, -6.39°)$	0.150 ± 0.047	2,728,265
c001	$(-30.00°, -2.97°)$	0.217 ± 0.041	2,069,471
c002	$(-30.00°, -5.97°)$	0.066 ± 0.022	1,153,139
c003	$(-30.00°, -7.98°)$	0.045 ± 0.018	723,786
c004	$(-30.00°, +3.98°)$	0.335 ± 0.070	1,537,790
c005	$(+19.99°, -2.97°)$	0.424 ± 0.078	2,555,073
c006	$(+20.00°, -5.98°)$	0.191 ± 0.041	1,524,750
c007	$(+19.99°, -7.98°)$	0.126 ± 0.028	1,044,536
c008	$(+19.99°, +3.97°)$	0.577 ± 0.066	1,711,455

[a] Color excess from the stellar average and standard deviation over the whole tile.

MS-TO to be around $\mathrm{K_s} \sim 17$, and its critical to have decent completeness ratios at this level ($\gtrsim 50\%$) for age determination.

3.2 The Observed Bulge Color-Magnitude Diagram

The observed $(\mathrm{K_s}, \mathrm{J}-\mathrm{K_s})$ CMD b249 is shown in the left panel of Figure 3.1.

The observed CMD shows a well populated RC at $\mathrm{K_s} \sim 13$ and $(\mathrm{J}-\mathrm{K_s}) \sim 0.8$; a prominent Red Giant Branch (RGB) easily traceable down to $\mathrm{K_s} \sim 16$; and the MS-TO at $\mathrm{K_s} \sim 17$ and $(\mathrm{J}-\mathrm{K_s}) \sim 0.5$. On the other hand, the SGB is barely visible because it is heavily contaminated by the foreground disk population. Indeed, the two vertical blue sequences departing from the bulge MS-TO and RC upwards correspond, respectively, to the foreground disk MS and its RC descendants.

In the magnitude range $10 \leq \mathrm{K_s} \leq 17.5$, the observed spread in all sampled evolutionary sequences is mostly due to the combination of metallicity and depth effect, whereas in the fainter range the contribution of the photometric errors becomes predominant. In b249 the differential reddening is not dramatically large ($\Delta E(\mathrm{J}-\mathrm{K_s}) \sim 0.047$ mag, see Table 3.1), and in fact when we correct for the extinction by using the VVV-based extinction map from Gonzalez et al. (2012), the dereddened CMD shows very similar magnitude spread (e.g. compare top-left and bottom panels in Figure 3.1).

Finally, as expected the characteristic double RC signature of the well known X-shape bulge structure is clearly detected at $\mathrm{K_{s0}} = 12.75$ and 13.27 mag. Indeed, as demonstrated by several authors (see §1.2) the X-shape structure is detected only in the outer bulge, at latitude $|b| > 5.5°$ and longitude $|l| \leq 4.5°$.

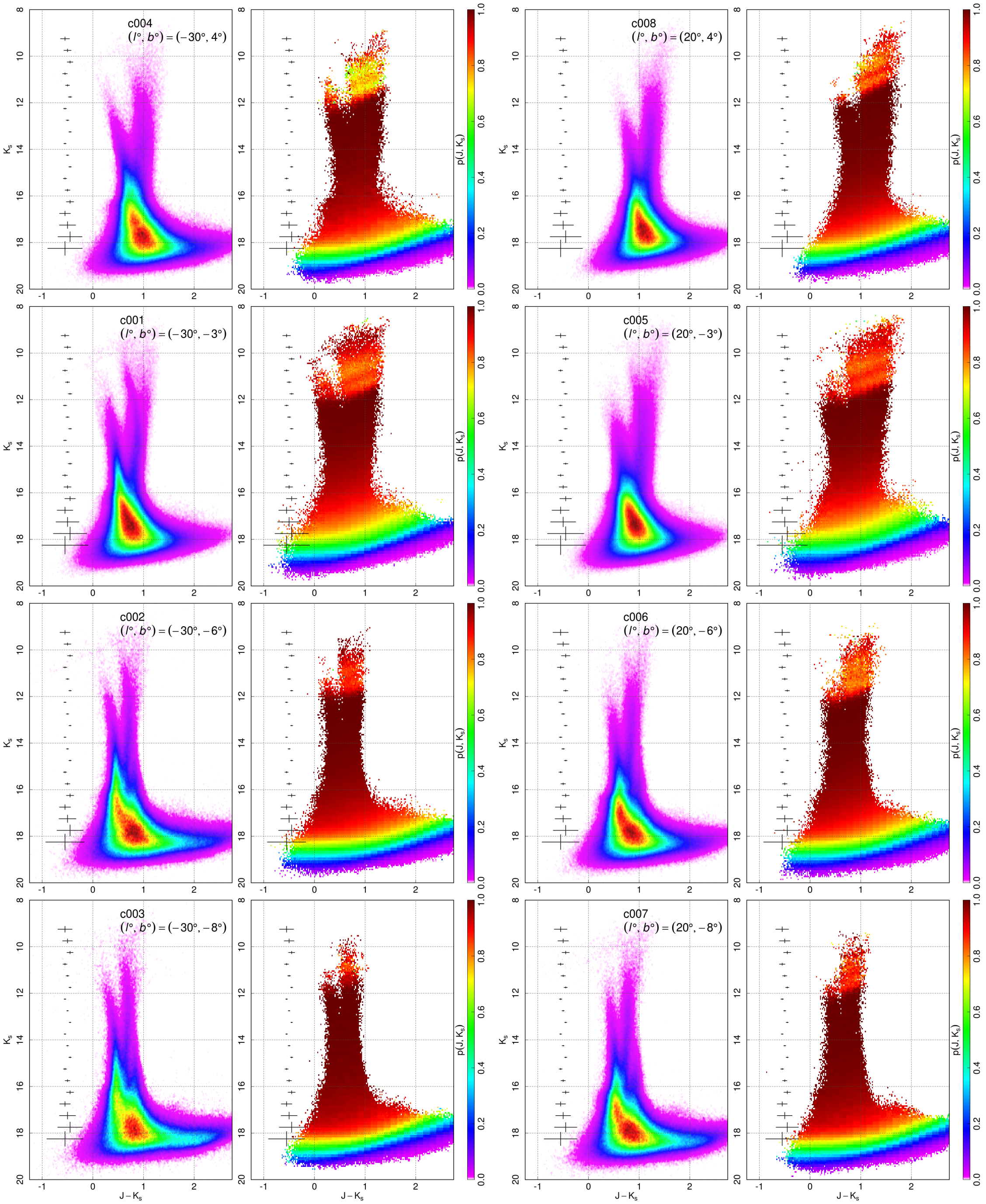

Figure 3.2: Observed CMDs of the 8 disk-control fields (left panels) and the corresponding photometric completeness map (right panels). Typical color and magnitude errors are shown as crosses at their respective reference K$_s$ level.

3.3 Disk decontamination procedure

As shown in Figure 3.1, the MS of the disk hits the bulge CMD exactly on top of its MS-TO, hence preventing any reliable age determination. Therefore, prior to any attempt to age-date the bulge population from its observed CMD, special care must be paid to remove the contribution of the intervening disk population along the line of sight. This can be done either by using proper motions (see Clarkson et al., 2008, 2011; Kuijken & Rich, 2002; Bernard et al., 2018), or statistically with a disk control-field (e.g. Zoccali et al., 2003; Valenti et al., 2013). Both methods require some assumptions, and therefore have their own pros and cons.

In principle, the proper motions selection yields more accurate decontamination, provided that bulge and disk populations have clear distinct kinematics along the line of sight of interest, which is not always the case. In fact, as evident from Figure 4 of Bernard et al. (2018), along different lines of sight the proper motion distributions of disk and bulge largely overlap, therefore some kinematics assumptions (i.e. cuts on the μ_l and μ_b distributions) are needed, and generally at the expense of the final bulge clean sample. In addition, from the observational point of view, the determination of proper motions is very time consuming, and as such this method has been always limited to very small regions (i.e. $< 2\,\mathrm{arcmin}^2$).

On the other hand, the statistical approach best suits the case of large surveyed areas such as that presented here, but it relies on the assumption that the adopted control-field is representative of the disk population along the bulge line of sight. In this respect, the selection of the disk control-field is crucial and must take into account that the contamination of the bulge CMDs from foreground disk stars strongly depends on latitude. Finally, it is worth mentioning that the proper motions provided by Gaia (DR2) do not allow a proper *cleaning* of the bulge CMDs. Being severely limited by both crowding and reddening already at $b = -6°$, the Gaia photometry is too shallow and does not fully sample the old MS-TO, which would at least impose a severe bias on the maximum age we can determine, or even make the age-dating impossible.

3.3.1 Comparable Populations

Figure 3.2 shows the derived Hess density diagram in the $(\mathrm{K_s}, \mathrm{J}-\mathrm{K_s})$ plane of the 8 disk control-fields studied here, together with the corresponding completeness map obtained from the artificial star experiments (see §2.3).

In the blue side of the diagram for $(\mathrm{J}-\mathrm{K_s}) \lesssim 0.5$, one can easily identify the very well populated MS, while the redder vertical sequence corresponds to the evolved RC population. At fixed latitude, the sampled disk population in the fields at longitude +20° and −30° has fairly similar CMD, with the major difference being the overall reddening, which appears to be smaller at −30°. As a consequence, the color of the MS and RC stars is generally bluer that what is observed at +20°.

As expected from an exponential disk density profile, at fixed longitude, the number of detected stars increases in fields closer to the Galactic plane, whereas at given latitude, the fields at +20° are systematically more populous than their counterpart −30° (see Table 3.1).

The first step of the decontamination process is the selection of the field that best represents the disk population observed along the bulge line of sight. This is done by comparing the bright portion of the CMDs ($\mathrm{K_s} \lesssim 15$) in the bulge and disk fields. Specifically, we trace the profile of the young disk MS and the RGB by means of a series of gaussian fits to their $(\mathrm{J}-\mathrm{K_s})$ color distribution per $\mathrm{K_s}$ magnitude bin (see Figure 3.3). It is worth mentioning that these sequences lie on the bright and most complete part of the CMD, and as such have the smallest error and dispersion in general.

A shift in color and magnitude along the reddening vector (see Nishiyama et al., 2009; Gonzalez et al., 2012) is applied uniformly to all disk control-fields to match the profile of the young blue MS with that observed in the b249 field. In doing this, we are ignoring distance distribution differences between the bulge and control fields. However because of the lack of secure and recognizable standard distance features (e.g. a RC) in the disk sequences, there is no way to properly account for them. We compare the relative differences between the profiled young MS in b249 and in all disk fields, and select the one with the lowest dispersion of the residuals, which are in turn defined by the distance of the control profiled young MS, interpolated on the observed bulge counterpart. Following this procedure, the disk field c002 located approximately at the same latitude of the target bulge region turns out to be the most appropriate for decontamination purposes.

After choosing the best candidate control field, the next important step is to make sure that its dispersion in color and magnitude due to the combination of systematics and photometric uncertainties (see §2.3) is comparable to the one observed in the bulge field. We have in principle two kinds of uncertainties. The first is related solely to the PSF-fitting procedure, and to the counts of the individual star profiles in an image taken with the photometric filter M: σ_M (i.e. $\mathrm{M} = \mathrm{J}, \mathrm{K_s}$). This is our photometric error, which is tied to the shape and brightness of the star. The second one comes from the measured dispersion in the completeness experiments: How artificial stars with similar injected magnitude m^{in} disperse into randomly different recovered magnitudes m^{rec}. We call this $\Sigma_M = \Sigma_M^{field}(M)$, which is mostly a function of $\mathrm{J}, \mathrm{K_s}$, unique to each *field* (i.e. detector and image), and likely comprising the systematics in the data. To estimate the latter, for each detector we use a 4^{th}-degree polynomial to fit the binned m_{in} vs. $\mathrm{MAD}(m^{in} - m^{rec})$ profile, where MAD is the adjusted median absolute deviation (i.e. 1-MAD is equivalent to 1-σ from a normal distribution).

We need to take into account differences in observing conditions and crowding for the observed disk and bulge fields, which result in differences in PSF-fitting and the associated error profiles. Given these differences between images as well as when considering individual detectors, we must be sure that the i-th star in the control field catalog, with magnitude M^i, has a similar error than an equivalent star would have in the bulge catalog. To do this, we define a value ς_M^i for the i-th star in the control field, as the maximum between its photometric error, completeness dispersion $\Sigma_M^{\mathrm{c002}}(M^i)$ and the corresponding $\Sigma_M^{\mathrm{b249}}(M^i)$

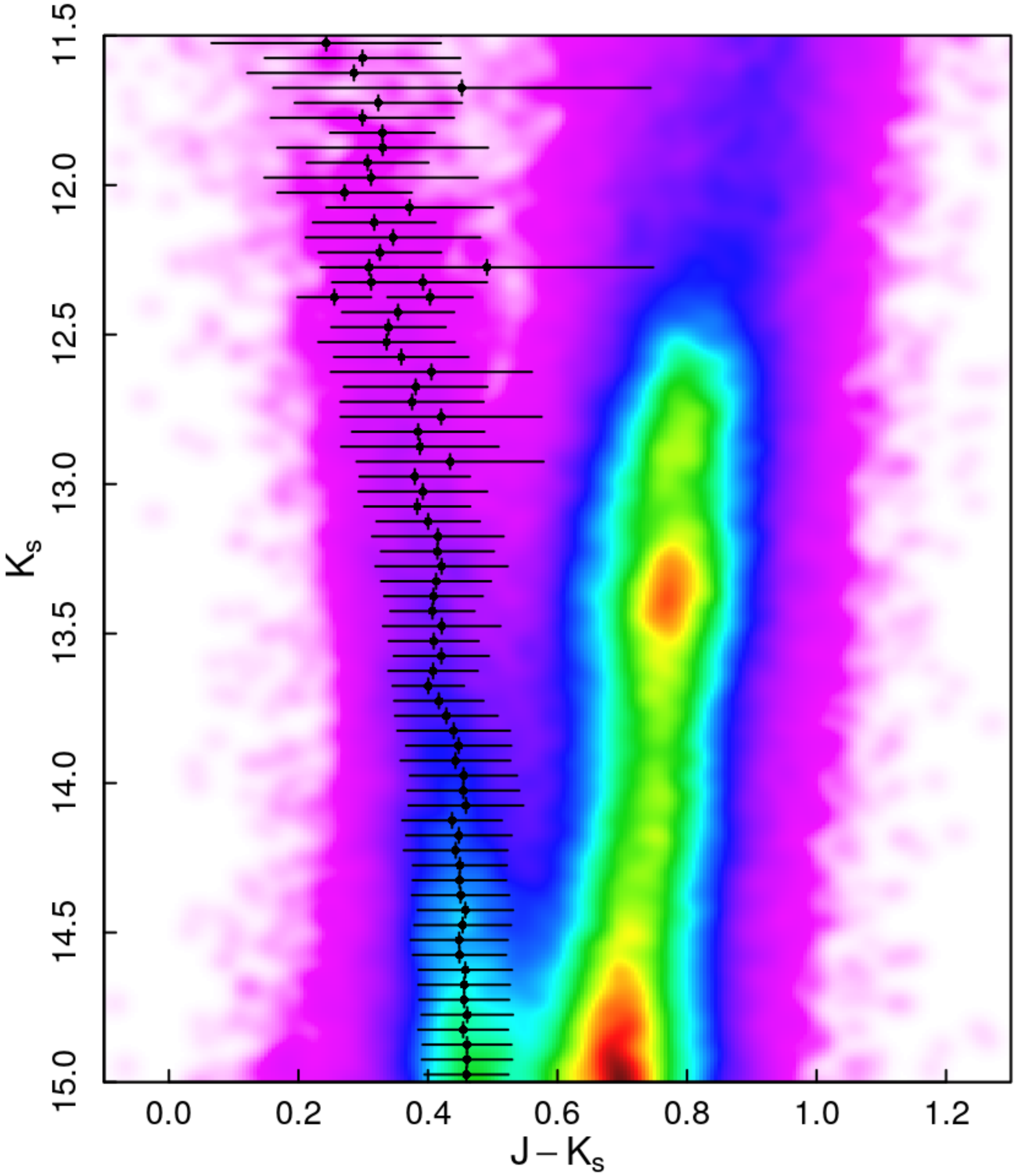

Figure 3.3: Color coded Hess density diagram of b249 compared to the gaussian young MS profile (black dots). Points with crosses refer to the calculated sequence mean color and width from the gaussian fits, and to the K_s bin width used to estimate them.

from the observed bulge field.

$$\varsigma_M^i = \max\left(\sigma_M^i, \Sigma_M^{\mathrm{c002}}(M^i), \Sigma_M^{\mathrm{b249}}(M^i)\right) \tag{3.1}$$

Similarly, as mentioned in § 2.3, each field and detector have their own completeness $p^{field}(\mathrm{J}, \mathrm{K_s})$, therefore a further step to guarantee a proper statistical subtraction is to correct the control field by its completeness and then apply the completeness of the observed bulge field. In practice, this can be achieved by assigning a weight ω^i to the i-th star in the control catalog, defined as:

$$\omega^i = p^{\mathrm{b249}}(\mathrm{J^i}, \mathrm{K_s^i})/p^{\mathrm{c002}}(\mathrm{J^i}, \mathrm{K_s^i}) \tag{3.2}$$

Finally, we must calculate the bulge-to-disk normalization factor, which gives us the number of stars to be removed from b249 for each given disk star observed in c002. To do so, we select a region in the b249 CMD where one is likely to find only the disk population (i.e. $(J - K_s) \lesssim 0.5$, and $K_s \lesssim 16$), as previously done by Zoccali et al. (2003); Valenti et al. (2013). This factor is a single scalar applied uniformly throughout the CMD.

3.3.2 Kernel approximation and subtraction

To take into account the effects of the error bars and systematics in the bulge and disk CMDs, we adopted a bivariate gaussian kernel smoothing map. This is similar to modelling any given star in the $[\mathrm{K_s}, \mathrm{J} - \mathrm{K_s}]$ plane as a bivariate normal distribution, whose centroid is just the color-magnitude position of the star, and its covariance matrix constructed from the errors of J and $\mathrm{K_s}$. We then stack/add all the gaussians, and evaluate the result on a finer grid, so that now the integral of this yields the expected number of stars in any given region of the CMD. As $\sigma_{\mathrm{K_s}}$ and σ_{J}, we take the corresponding ς_M from (3.1), and approaching the problem as if all stars had errors defined by this quantity.

Because the errors and dispersion are a function of the J and $\mathrm{K_s}$ magnitudes for any given star, there is not an unique kernel valid for any given catalog. Therefore we divide the dataset in ς_{J}-$\varsigma_{\mathrm{K_s}}$ bins, calculate the kernel map for each, and add them together.

After all this, the kernel map represents the approximate CMD distribution of the control-field, as if it was observed in the bulge field, considering its incompleteness and different error profiles.

Once the kernel map is constructed, we scale it by using the bulge-to-disk normalization factor (see § 3.3.1) in order to ensure that the expected number of stars in the kernel map and in the observed bulge CMD is the same. This last step also ensure that each color--magnitude bin in the kernel map tells us how many stars we need to remove from the observed CMD to obtain a bulge-only sample. So, for each one of these bins, we extract the corresponding number of stars by randomly picking from the observed catalog entries within. After the removal, we count the number of stars within the window we defined for the bulge-to-disk normalization factor in the CMD, and compare it with the original

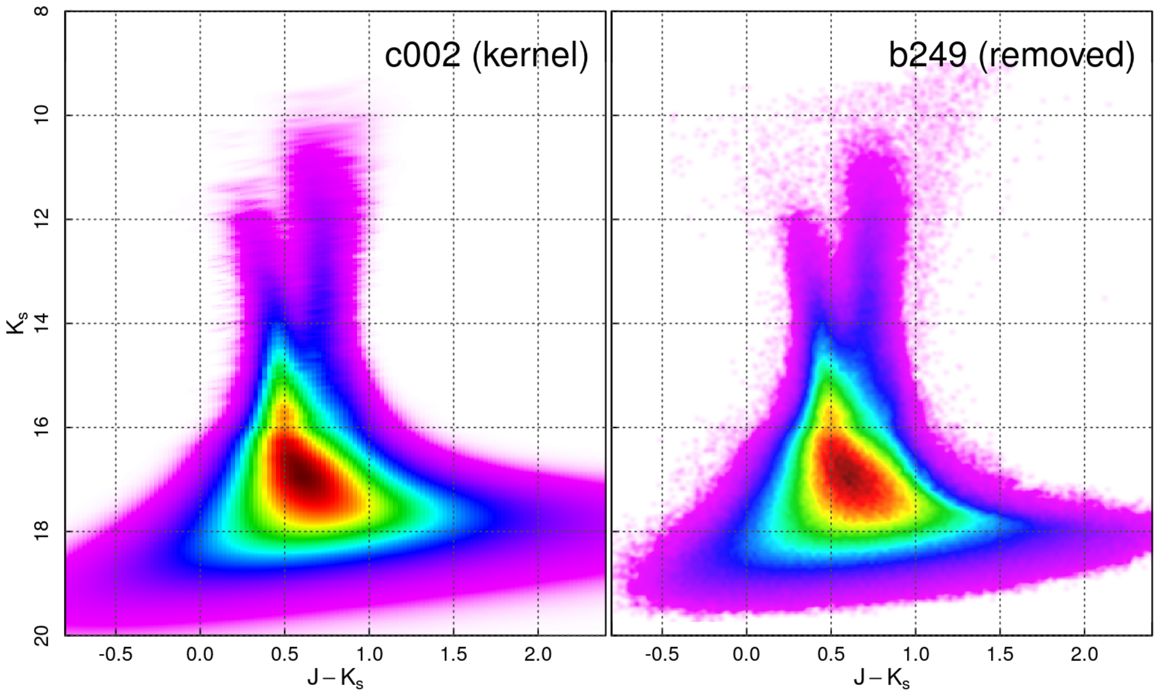

Figure 3.4: *Left*: Intensity kernel map for c002, as constructed from b249 dispersion. *Right*: CMD of the stars removed from b249 by using the kernel map shown in the left panel.

observed catalog in order to get a new scale factor (usually a small correction of the order of 10%) and reapply the subtraction.

The remaining stars represent the effective bulge clean sample.

It is important to note that this procedure yields bulge-like and disk-like catalogs according to their CMDs only. In other words, being in the clean catalog does not mean bulge memberships for the stars in them; if we had kinematic data to distinguish between disk and bulge stars, we would find a mixture of bulge and disk in the clean sample. Nevertheless, the clean catalog CMD would be bulge-like, while the removed catalog CMD would be disk-like. It is very important that we emphasize this property, since it means that we cannot correct for reddening; there are disk stars in the clean bulge sample, which are not affected by the same reddening as the bulge, and thus if *corrected* would only add noise to the CMD.

3.4 The bulge clean sample

We performed the decontamination procedure described in § 3.3 on the observed bulge field b249 by using c002 as disk control-field.

In Figure 3.4 we show the kernel map of c002 (left panel), and the density map of the stars subtracted from b249 (right panel). The overall similarity of the two maps provides a first sanity check, demonstrating that the procedure worked well.

Indeed, for $K_s \lesssim 19$ and $0 \lesssim J - K_s \lesssim 1.2$ the maps are virtually indistinguishable, except for the 2 faintest magnitudes in the plot, where the kernel shows a wing extending redwards that is not reflected in the removed set. In this case, the wing extends towards rapidly declining completeness (i.e. see Figure 3.1), which is not taken into account in the kernel map but only considered in the weight of the entries of the control catalog.

The final result of the decontamination procedure is presented in Fig. 3.5, where we show the CMD of the bulge b249 clean sample, consisting of 1,654,603 stars, which is about 66% of the original catalog.

By removing the foreground disk population, one can now more easily recognize the bulge main evolutionary features: the double RC $\mathrm{K_s} = 12.83, 13.35$ and $(\mathrm{J} - \mathrm{K_s}) = 0.79)$, the RGB $(K_s \lesssim 15.5, (\mathrm{J} - \mathrm{K_s}) \gtrsim 0.5)$, the SGB $(16.5 \gtrsim K_s \gtrsim 15.5$, and $0.4 \lesssim (\mathrm{J} - \mathrm{K_s}) \lesssim 0.7)$, and the hot-spot near $K_s \sim 17$ with a shape resembling a MS-TO. The halos silhouetting the subtracted young disk MS are outliers that could not be removed completely. However, their signal in the Hess density diagram is very weak (i.e. ~ 4000 stars, $< 0.2\%$ of the maximum density value, and $\sim 11\%$ of the original observed in the same region), therefore they can be safely neglected. The blue feature near $(\mathrm{J} - \mathrm{K_s}) \sim 0.1$ and $K_s \sim 16.5$ is likely an artefact due to stars mostly located at a corner of detectors 2, 8 and 16. The diagnostic values (shape and χ^2 from PSF-fitting) of these artefact have different distributions to that of normal stars, but they still overlap, making an usual cut (e.g. in χ^2) ineffective to clean them. This feature was of course present also in the observed CMD (i.e. Figure 3.1), but since it is not real nor present in the control field, it became highlighted after the decontamination.

Finally, in Fig. 3.5 we also show a collection of BaSTI isochrones for the MR régime from GIBS ($[\mathrm{Fe/H}] = +0.08 \pm 0.16$) with ages 5, 7.5 and 10 Gyr, and also MP ($[\mathrm{Fe/H}] = -0.35 \pm 0.17$) for 11 Gyr. It is evident that any attempt to deriving the age of the bulge population cannot rely on simple isochrones fitting because the observational effects introduce a color and magnitude spread in the CMD larger than that produced by the age and metallicity on the isochrones. As is detailed in §4.1, the use of synthetic population models accounting for observational effects represents instead a more adequate approach.

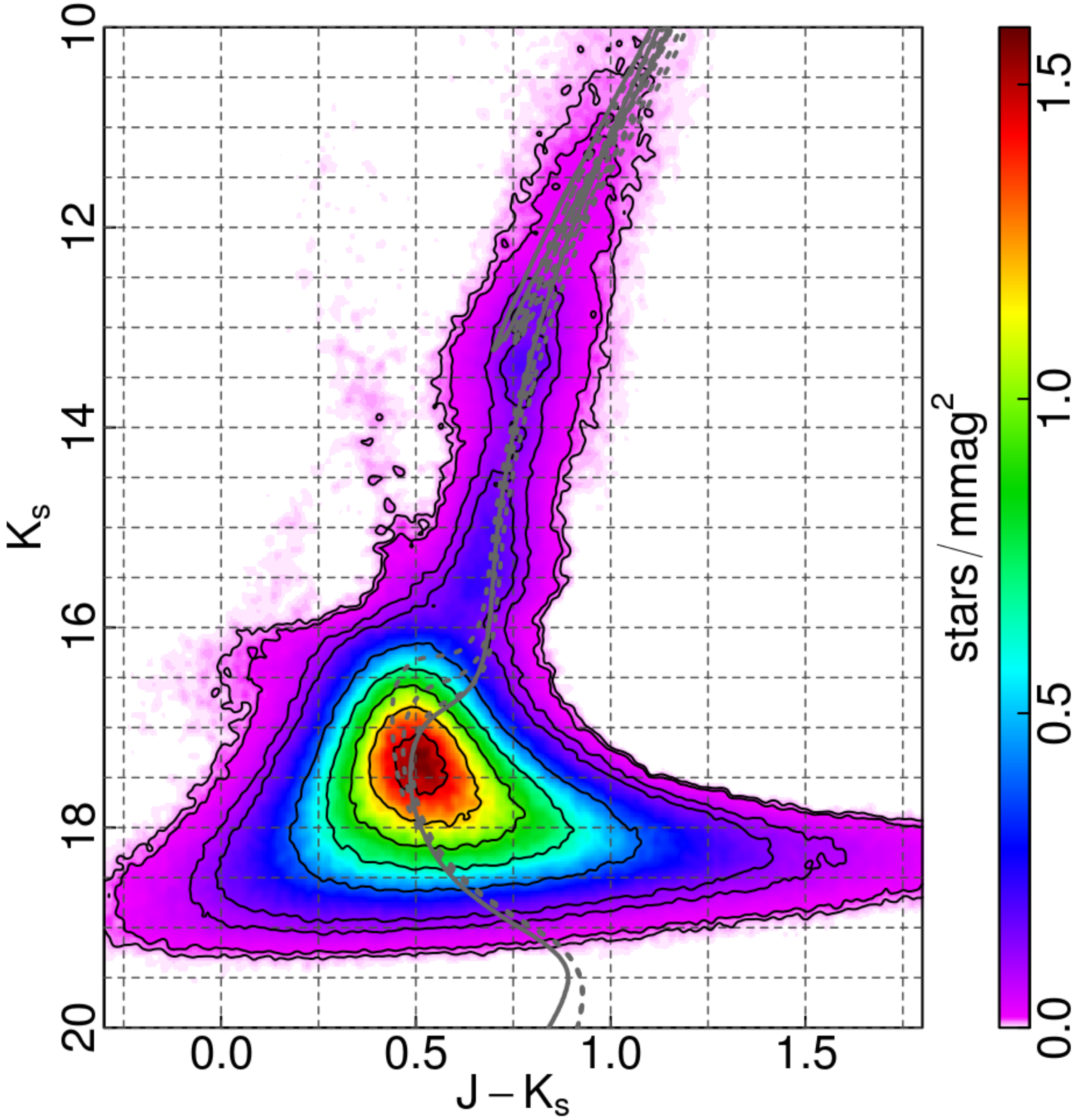

Figure 3.5: Hess diagram of the bulge b249 field as statistically decontaminated from the foreground disk population. Solid black contours are isodensity curves spaced by 1%, 5% and then from 1/12 to 11/12 of the maximum density, in steps of 1/6. Also plotted are BaSTI isochrones for ages (bluest to reddest) 5, 7.5, 10 and 11 Gyr, following the metal--poor régime from GIBS for the oldest (grey lines), and metal-rich for all others (dotted line). The isochrones have been shifted so that their RC and RGB loosely match the observed ones.

Chapter 4

Mapping the bulge stellar age

In this chapter I focus on the determination of stellar population ages in 12 bulge regions, sparsely located within the area mapped by the VVV, through the comparison between synthetic and observed CMDs. First, I describe the method used to simulate synthetic population catalogs carrying out the same observational effects of the observed bulge fields, then I present the adopted procedure to infer the stellar ages.

To tackle the problem of constraining the age of the bulge fields I have followed two different approaches. One method is to produce synthetic populations with MDFs spectroscopically inferred by the GIBS survey but different ages mixtures, whereas the second is to use the IAC-POP/Minniac suite (Aparicio & Hidalgo, 2009; Hidalgo & Aparicio, 2016) to find the optimal solution that matches the observed and synthetic CMDs with no particular assumption on the age and metallicity spread. I discuss advantages and disadvantages of both approaches, as well as their limitations and present these in the context of fields with different extinction and crowding, hence different photometric completeness. Finally, I use the results I obtained for the selected fields to build the first age map of the Milky Way bulge. I also compare the age-map and individual points with N-body simulations of an evolved disk galaxy.

The content of this chapter has been partially published in Surot et al. (2018a, submitted).

4.1 The case of b249

We start by developing a proof-of-concept. Specifically, we use b249 field again as a test case to show the comparison of the bulge clean sample with synthetic populations models, and the selection of the best-fit model. A discussion on what is needed to improve the fit in terms of age is also provided.

As shown in the previous chapter, simply fitting isochrones to the clean sample does not yield meaningful results because of the spread in color and magnitude induced by the observational effects around the expected MS-TO (see Figure 3.5), as well as the nominal increase in dispersion with fainter $\mathrm{K_s}$ magnitudes. In addition, because we are studying a complex stellar population over a large surveyed area, the metallicity and large distance spread further complicate the analysis, with a dispersion in color and magnitude that cannot be qualitatively taken into account by using only isochrones. Instead, we resort to the comparison of the bulge clean sample with synthetic populations of known age and metallicity.

4.1.1 Simulation of synthetic populations

To create a *realistic* model dataset to be directly compared to the observed bulge clean sample we must introduce the observational effects in the simulations, i.e. *dispersing* each artificial star according to the photometric errors, systematics, reddening and distance spread etc. In other words, we need to take into account all the effects that transform the true brightness of a given star located in a particular patch of the sky into a pair of $\mathrm{JK_s}$ magnitude obtained following the reduction procedure described in §2.

One way of achieving this is using a model that relates the observed magnitudes to the true ones (i.e. gaussian errors, shot noise, crowding, etc). However this implies a rather perfect and extensive knowledge of all processes involved in the magnitude extraction, and the feasibility of implementing this into the synthetic populations.

On the other hand, to bypass the problem that we do not have such model, a more empirical approach is to simply let the data *tell us* how this transformation from true to recovered magnitudes works. The key ingredient to successfully simulate the observations is a specialized form of the completeness experiments from §2.3. As described in Appendix A, we can use the relation between (binned) injected vs. recovered magnitudes to approximately emulate the observational effects.

For this purpose, we add ten times as many artificial stars per detector with a color and magnitude distribution constrained by the *injection window* shown in Figure 4.1, which defines the locus where a complex stellar population, with metallicities $0.0001 \leq Z \leq 0.04$ and ages between 30 Myr to 13.5 Gyr, is expected to be. Note that the injection window has been further expanded ($\sim 30\%$) in size to account for spread in distance and reddening, and divided into smaller subsections (e.g. bright stars, RC, MS, MS-TO, faint end) to increase the relative density of injected stars over key or incomplete features (see Figure 4.1). The hexagonal injection grid in XY remains exactly the same as described in §2.3[1].

We need this enhanced number of artificial stars (about a million per detector) because the denser the injected CMD is, the more accurately we can disperse the stars and hence minimize the noise we add through this process. In particular, a sufficiently dense injected CMD means we can pick a set of injected $\mathrm{JK_s}$ magnitudes in the artificial star atlas within a very small color-magnitude bin, and still get enough stars to have a robust estimation of how the injected magnitudes in that bin get dispersed into recovered magnitudes. In simpler terms, we want to have at least 10 stars within a very small range in injected color and magnitude, small enough to be comparable to the precision at which we can define

---

[1] To run these CPU intensive simulations we used resources of the Computational Center for Particle and Astrophysics (C2PAP). https://wiki.tum.de/display/c2pap2018/C2PAP

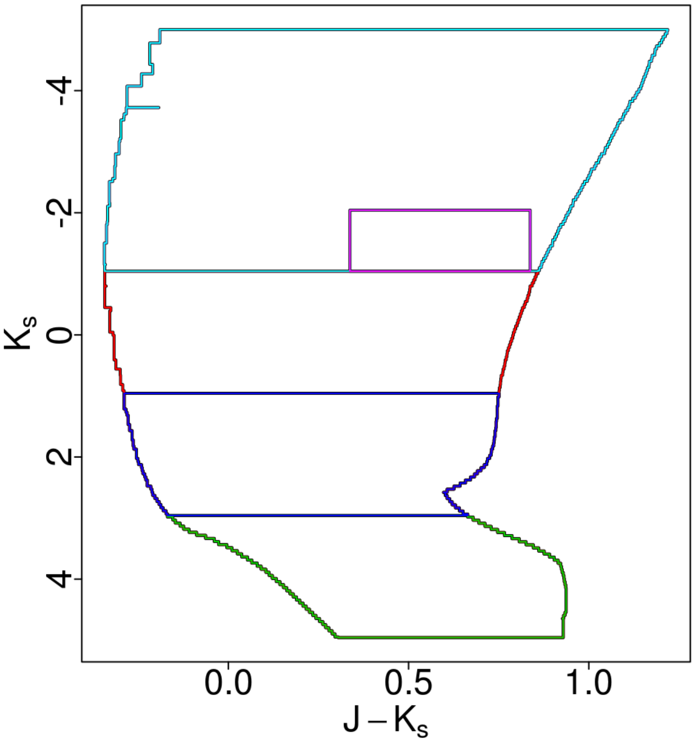

Figure 4.1: Injection windows for the simulation experiment. Each sub-window has a different relative density of injected stars. We have chosen to enhance density on the RC (magenta) and MS-TO (blue) areas, while reducing the number of injection in the less important (for us) bright stars (cyan).

the magnitudes in our catalogs (i.e. of the order of 0.001 mag). This allows us to add the photometric and systematic errors, as well as completeness considerations into the JK_s magnitudes of a synthetic catalog, producing a new set of recovered JK_s that would look like as it was actually observed.

Now we have two ways of defining a synthetic population. Both methods carry their own differences and limitations, which can potentially lead to different results. Following is a brief description of each method, as well as the reasoning behind the final decision of using one over the other.

The first method makes use of the BaSTI (Pietrinferni et al., 2004, 2006, 2013, 2014) isochrones, and creates the population as a series of points along the isochrone dispersed into a number of stars N, with the corresponding mass and the IMF from Calamida et al. (2015). Specifically we repeat (A.2) N times for each point in the isochrone. This method has the advantage of providing an accurate representation of the bulge metallicity distribution (Ness et al., 2013a; Gonzalez et al., 2015b; McWilliam, 2016, and references therein) because we can use a set of isochrones spanning a broad metallicity range ($-3.6\,\mathrm{dex} < [\mathrm{M/H}] < +0.5\,\mathrm{dex}$), including α-elements enhanced and solar scaled régimes.

We can create whatever complex mix of populations with accuracy and complete control on the number of stars in the final product, with the ability to track both RC and MS-TO stars from their theoretical values given by the isochrones, to the final $\mathrm{JK_s}$ values after the dispersion by the observational effects.

On the other hand, we are unable to properly add the contribution of unresolved binaries because of the limited mass range, and the procedure to disperse isochrones according to the field of interest several times such as to cover a relatively large metallicity and age grid can be very time consuming.

The second method exploits the IAC-STAR (Aparicio & Gallart, 2004) stellar population code. Under the assumption of uniform star formation, the code is used to create an atlas of synthetic stars of ages between 30 Myr and 13.5 Gyr, and metallicities $0.0001 < Z < 0.04$.

Specifically, by adding 35% unresolved binary fraction and using the IMF from Calamida et al. (2015) while linearly interpolating the slope coefficients according to this binary fraction, we obtain in just one run a full-blown synthetic population atlas, where each entry is a single star/observation, with its own $\mathrm{JK_s}$ magnitudes, mass, age and metallicity. Beside the ability of taking into account the unresolved binaries fraction, this approach has the additional advantage of being less time consuming because once the atlas is dispersed we can derive all possible combinations of populations mixes easily, and thus allowing for quick comparison between models and observations.

However, in this case the drawback is represented by the metallicity range available to the code, which is limited to $[\mathrm{Fe/H}] \lesssim 0.42$ dex and solar scaled enrichment. In the context of bulge metallicity distribution (see for instance right panel in Fig.1.2), this implies that we lack a proper representation of the population with metallicity in the most 0.2 dex metal-rich bin of the whole bulge distribution. Nevertheless, because the difference in color and magnitude of MS-TO stars with metallicity $[\mathrm{Fe/H}] = 0.4$ dex and 0.5 dex are $\Delta(\mathrm{J}-\mathrm{K_s})_{\mathrm{MS-TO}} \lesssim 0.006$ mag and $\Delta\mathrm{K_{sMS-TO}} \lesssim 0.035$ mag (for 7 Gyr), which is well within the error budget, we argue that the use of a metallicity range slightly narrower on the metal-rich side has a negligible impact of the age determination. At the level of RC, the differences are higher, $\Delta(\mathrm{J}-\mathrm{K_s})_{\mathrm{RC}} \sim 0.02$ mag and $\Delta\mathrm{K_{sRC}} \sim 0.05$ mag, which are both of the order of the uncertainties at these levels. Yet, for the purposes we use the RC, these differences are dwarfed by the much larger dispersion from distance, differential reddening and the rest of the effective metallicity distribution (see §4.1.2). which can compound to a dispersion of the order of $\sigma_{\mathrm{K_s}} \sim 0.2$ in the general case. In addition, although the fraction of MR stars increases towards the Galactic plane, the current metallicity restriction yields a *loss* of population in average of ∼ 17% and ranging between ∼ 1-25%, within the bulge region where we restrict the age determination (i.e. $|b| \gtrsim 3.5°$).

Finally, it is fair mentioning that because a simple stellar population born from this atlas is defined within a given age-metallicity bin, the number of stars in it depends directly on the width of this bin. In other words, any given simple stellar population will always have a non-zero spread in age and/or metallicity, and aiming for an increasingly sharp definition in age and metallicity will necessarily incur in poorer statistics from the reduced number of stars.

We have ultimately decided to use the second method to build the synthetic populations used to compare with observations. The main reason is because the presence of unresolved binaries in a purely old population may appear in a CMD as if there was a younger component added into the mix. By using the supported unresolved binary fraction from the IAC-STAR code, even though we ignore the exact binary ratio of the observed field, a typical number (35%) is enough to produce more realistic results.

On the other hand, to address the possible problem related to the lack of α-elements enhancement in the IAC-STAR code, for the representation of the bulge MP old component (see §1.1), we have recurred to a simple shift in metallicity, given the approximation:

$$[\mathrm{M/H}] \approx [\mathrm{Fe/H}] + [\alpha/\mathrm{Fe}] \tag{4.1}$$

Where the members are, from left to right, relative total metal abundance, iron abundance and α-elements to iron. Although we acknowledge that isochrones following this equality do differ between each others, we argue that this approximation is sufficiently good in the magnitude range (or evolutionary phases) relevant for the age determination, and we will be using this relation only on the metal-poor ($[\mathrm{Fe/H}] \lesssim 0$) and old ($\gtrsim 10\,\mathrm{Gyr}$) populations. We show in Figure 4.2 a comparison between two coeval isochrones of 10 Gyr, one α-enhanced and the other solar scaled with equaled [M/H] to solar value, as given by (4.1). The maximum difference is in color for the RC ($\Delta(\mathrm{J}-\mathrm{K_s})_{\mathrm{RC}} \sim 0.026\,\mathrm{mag}$) with minimal magnitude difference ($\Delta\mathrm{K_{sRC}} \sim 0.012\,\mathrm{mag}$). At the MS-TO, we see $\Delta(\mathrm{J}-\mathrm{K_s})_{\mathrm{MS-TO}} \sim 0.008\,\mathrm{mag}$ and $\Delta\mathrm{K_{sMS-TO}} \sim 0.03\,\mathrm{mag}$. We note that these differences may change with age and composition and may increase at higher metallicities, but these differences are at or well below the error budget (see Figure 2.7). Furthermore, considering all the *blur* added to the CMD from considerations in §4.1.2, the relative noise added from this approximation becomes secondary.

With this, we can emulate the effects of α-enhancement of +0.31 dex in a given population of metallicity [Fe/H], by simply taking a subset of the IAC-STAR atlas that has a higher metallicity by a factor equivalent to the enhancement.

4.1.2 Metallicity, reddening and distance dispersion

Having decided how to construct the synthetic simple stellar population, we can now create whatever mix we want/need. In particular for this proof-of-concept, we adopt the spectroscopic MDF provided by the GIBS survey (Zoccali et al., 2017) based on 213 RC stars observed in the b249 field. Here we just remind that the MDF of bulge fields as obtained from different surveys (see §1.1.2) are best represented by two gaussians defining a MP and MR component. For the specific case of b249, the MR distribution peaks at $[\mathrm{Fe/H}]_{\mathrm{MR}} = +0.08 \pm 0.16\,\mathrm{dex}$, while the MP at $[\mathrm{Fe/H}]_{\mathrm{MP}} = -0.35 \pm 0.17\,\mathrm{dex}$. Moreover, to further constraining the synthetic populations, we adopt the 1:1.2 ratio of MP to MR, as suggested by the MDF, with α-elements enhancement of +0.31 for the MP population

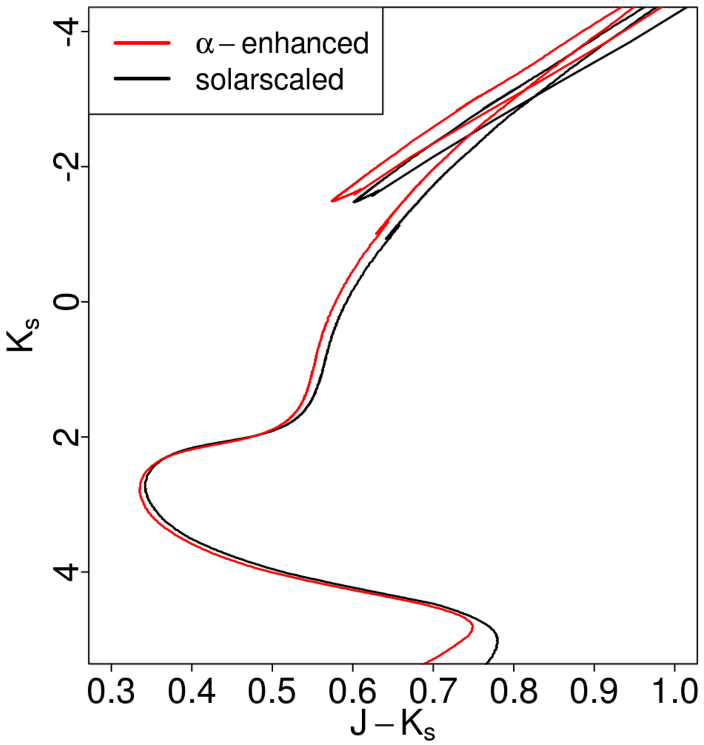

Figure 4.2: Comparison between α-enhanced (solid red line) and solar scaled isochrones (solid black) from BaSTI of 10 Gyr and with equaled solar [M/H] using (4.1).

(Ness et al., 2013a; Gonzalez et al., 2015b; McWilliam, 2016, and references therein). Note that as just detailed in §4.1.1, the considerations of an α-enhanced population is purely an approximation given by (4.1).

Differential reddening is an important factor that we must take into consideration in the bulge area. Now we take the chance to remind the reader that when mentioning *the observations* we are actually referring to the decontaminated bulge sample obtained by applying the method in §3. We must note that this observation is affected by the reddening in the original field, and also due to the final caveat pointed out in §3.3.2, it cannot longer be corrected for extinction. As such, in order to incorporate the reddening into the analysis, instead of correcting the observations, we redden the synthetic population before dispersion. In particular, we define a color excess value for each star in the synthetic population catalog by random draw from the color excess of the stars in the observation, as obtained with the extinction map in §2.7. Then we redden the JK_s values using the reddening law from Nishiyama et al. (2009) accordingly.

To account for the field depth (i.e. distance dispersion), we exploit the fact that RC stars are optimal distance candles, therefore the width of their distribution provides information on the distance spread probed in the observed field. Specifically, we have used the method in §2.6 to fit at least 2 gaussians to the RC area, including a third for the RGB-bump. For each RC-gaussian we estimate a $\sigma_{\mathrm{K_s}}$, which should be decomposed as the equation:

$$\sigma_{\mathrm{K_s}}^2 = \sigma_r^2 + \sigma_A^2 + \sigma_P^2 \tag{4.2}$$

Where σ_r, σ_A and σ_P are respectively, the gaussian spread introduced by distance dispersion alone, from differential extinction, and from population-related parameters (e.g. age, metallicity, etc). We can isolate $\sigma_A^2 + \sigma_P^2$ from the synthetic populations previous to any dispersion, and after applying a randomly drawn extinction. Then σ_r can be calculated from a quadratic subtraction. Finally, to emulate the distance dispersion on the synthetic population we add grey (same shift in J than in $\mathrm{K_s}$) gaussian noise, with variance σ_r^2.

We take the chance to note that even though the right hand side of (4.2) should also include photometric and systematic terms, we argue that the associated errors at the RC level are small enough to provide a negligible contribution (see Figure 2.7).

The last remaining step is to match the position of the RC ($\mathrm{K_s}$-magnitude and color) in the observed and synthetic catalogs. To do this, for each gaussian from the RC fitting of the observations, we create a synthetic population with the steps above, disperse it, and obtain a fit to the RC of this synthetic population. We then add $(\mathrm{J} - \mathrm{K_s})$ and $\mathrm{K_s}$ values to the synthetic population to match the RC to the corresponding RC component in the observations. Lastly, we combine both using the relative ratio of the RC in the observations.

The b249 field is located in the region where the X-shaped of the bulge reveals as a split in the RC distribution (see §1.1.1). Here we opt to assume that the populations from either RC are identical, regardless from their actual origin. This is mostly to simplify our calculations, however it should be stressed that so far there is no evidence suggesting otherwise.

In Figure 4.3 we demonstrate the effect of this dispersion method, from the purely theoretical synthetic population (top left panel), with distance and reddening additions (top right panel), to the actual dispersed CMD. In particular, we show the case of an isochrone for a 7 Gyr old population having a MDF defined from GIBS in the MP régime. It must be clear that this dispersion is unique to the field b249, as it not only has a particular RC profile and extinction, but it also provides its own signature uncertainties and $\mathrm{JK_s}$ dispersion in the completeness experiments.

Also in Figure 4.3, we have also dispersed an equivalent synthetic population from the IAC-STAR atlas, and following the discussion in §4.1.1, we show the difference between the dispersion of a synthetic population built from an isochrone and from the output of IAC-STAR code (see bottom panel), providing the evidence we needed to decide on the IAC-STAR atlas as our source of synthetic populations from here on out. In principle, what is shown in the bottom of Figure 4.3 is the signal in $\sigma_{|\Delta N|}$ from the 35% unresolved binary fraction, plus the age width necessary for a population from the IAC-STAR atlas and the approximation regarding α-enhancement. Note that the *hotspot*, the point of highest stellar density in both the original synthetic population and the dispersed version mostly coincide in position, meaning that regardless of the observational effects, it provides a good way to judge at a glance the observed population.

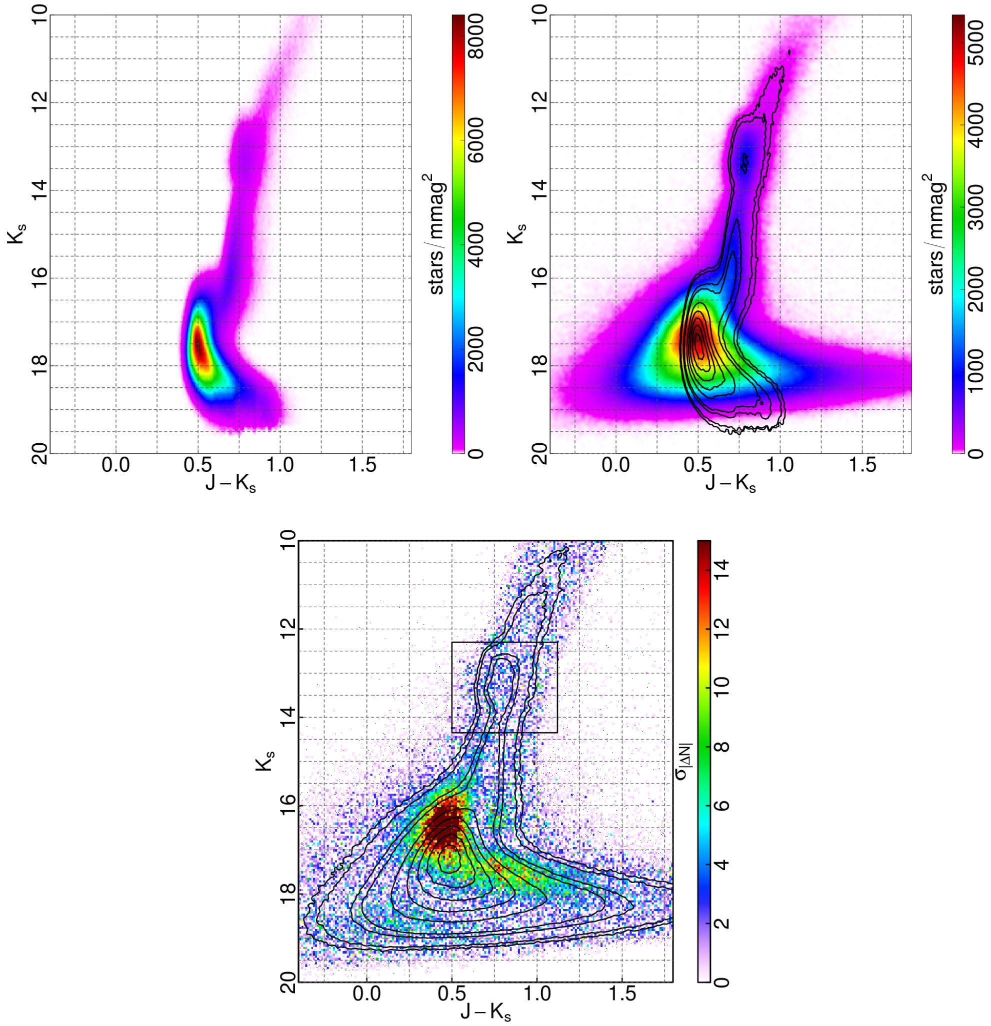

Figure 4.3: Sample dispersion from a 7 Gyr MP population from b249 data. Top two panels show (left) the Hess diagram of the synthetic population resulting from the application of distance and extinction distribution draws to a series of isochrones of 7 Gyr, that are distributed in metallicity according to b249 GIBS MDF MP component, and (right) the result of dispersing said population given the guidelines in §4.1.1. The contour corresponds to the undispersed population. The bottom panel shows the difference between this isochrone-based population to the equivalent that is extracted using a subset of the IAC-STAR atlas we have at our disposition. The signal observed here is mostly related to the unresolved binary fraction that is handled by IAC-STAR, but also likely related to the small age dispersion needed to extract this atlas.

4.1.3 The atlas

With all these considerations, we follow with a detailed description of the main IAC-STAR atlas that we will be using and referring to throughout this work.

As mentioned in §4.1.1, the atlas consists of a composite synthetic population created with a uniform SFH across all permissible ages and Z in the model by IAC-STAR using BaSTI libraries. These BaSTI libraries are similar to the set we have described in §4.1.1, but they carry the metallicity limitation of $Z < 0.04$. The bolometric calibrations to the VISTA photometric system ($\mathrm{ZYJHK_s}$) are done internally. The faintest magnitude for the synthetic population calculation is set to $M_{\mathrm{K_s}} \approx 7$, and the number of surviving stars in the atlas (effectively, the number of entries in it) is 150 million, which is a sub-sample from 1.5 billion total calculated. This atlas is universal (i.e. acts simply as the model we use), and has been calculated only once.

The resulting synthetic catalog is, however, useless without further tailoring it to the data. Indeed, we must apply the distance and reddening considerations described in §4.1.2, which for this case are done based on b249, but must be re-performed on a field-to-field basis, and accounting even for the RC split due to the bulge X-shape (double gaussian, formally bimodal or not) when necessary. After these considerations, we proceed to assign a completeness value to each entry based on the specialized completeness tests, and then use these to simulate the observational effects pertaining to each particular field (see Appendix A). Throughout this process, we are making the assumption that the completeness, and the associated dispersion through observational effects, does not change with XY position in the image. This approximation is founded in a negligible XY variation in these quantities discovered in early tests, with the exception of areas near to very bright stars, which were in turn estimated to be negligible for practical and general purposes in the extensive fields we work with.

The ultimate product of this atlas processing is a catalog with magnitudes ranges (and RC) roughly equivalent to the referenced field, together with similar dispersion and differential reddening. Each entry would have $\mathrm{JK_s}$ magnitudes, along with a corresponding age and Z value.

4.1.4 Comparing model to observation

Theoretically, once the metallicity, α-enhancement, distance, and reddening of the synthetic population are constrained, as well as a given binary fraction and IMF are assumed, the age becomes the only free parameter. Hence, in principle we could let the age vary until we find the best match to the observed clean sample.

According to the models, the observed RC shape suggests that the MP component must be quite old, between 11 and 12 Gyr, therefore in the simulations we allow only the age of the MR component to vary. Note that this is also in line with all previous studies (see §1.2) that found the MP bulge stellar population to be consistently older than ∼10 Gyr. Indeed, if a significant fraction of a younger population is present then it is likely to be more metal-rich than the older one.

We start by a set of six simple scenarios, which are based on observations available in the literature (Zoccali et al., 2017; Bensby et al., 2017):

- **S1**: MP = $(11 \pm 0.3)\,\mathrm{Gyr}$, MR = $(10 \pm 0.3)\,\mathrm{Gyr}$
- **S2**: MP = $(11 \pm 0.3)\,\mathrm{Gyr}$, MR = $(7.5 \pm 0.3)\,\mathrm{Gyr}$
- **S3**: MP = $(11 \pm 0.3)\,\mathrm{Gyr}$, MR = $(5 \pm 0.3)\,\mathrm{Gyr}$
- **S4**: age-metallicity distribution from Bensby et al. (2017) as obtained from their Figure 14 (i.e. from individual stars, see right panel of Fig.1.5).
- **S5**: MP = $(11 \pm 0.3)\,\mathrm{Gyr}$,
  MR = $40\%(10 \pm 0.3)\,\mathrm{Gyr} + 60\%(7.5 \pm 0.3)\,\mathrm{Gyr}$
- **S6**: MP = $(11 \pm 0.3)\,\mathrm{Gyr}$,
  MR = $60\%(10 \pm 0.3)\,\mathrm{Gyr} + 40\%(7.5 \pm 0.3)\,\mathrm{Gyr}$

Where it is present, the $\pm 0.3\,\mathrm{Gyr}$ denotes a flat age distribution around the alluded central age, and for all simulations but S4 we adopt the MDF spectroscopically derived by the GIBS survey (Zoccali et al., 2017) that is best represented by two gaussians for the MR and MP components respectively. In addition, as mentioned before, we adopt the MR:MP ratio found in GIBS implying that the number of RC stars in the MR and MP domains has the ratio 1.2:1.

The results of the simulations for the six scenarios are shown in Figure 4.4, where in the left panels we compare the Hess density diagrams of the synthetic population with the isodensity contours corresponding to the clean observed sample as derived in Figure 3.5.

To assess the quality of the match between simulations and observations and deriving the best-fit model, we create for each simulation the corresponding residuals map (see right-hand panels in Figure 4.4). Specifically, the noise of the observed CMD has been first modeled with a bootstrap approach. We repeatedly ($\sim 10,000$ realizations) take a random resample of the complete observed catalogs, and save the residual between the subtraction of the original and resampled CMD density for each iteration. This effectively produces a residual distribution per color-magnitude bin of the observed CMD, which is used to measure any significant deviation when comparing the synthetic populations by means of:

$$\sigma_{|\Delta N|} = \frac{|hN_{sim} - N_{obs}| - |\bar{N}|_{boot}}{\sigma_{boot}} \tag{4.3}$$

Where N_{sim}, N_{obs} and $|\bar{N}|_{boot}$ are respectively, the number of stars in the simulation, number of stars in the observations and mean of the bootstrap distribution, for any given color-magnitude bin. h is a scale factor, which we define simply as mean value of N_{obs}/N_{sim} in a box surrounding the RC area of the CMD. σ_{boot} is the standard deviation of the bootstrap distribution at the corresponding color-magnitude bin.

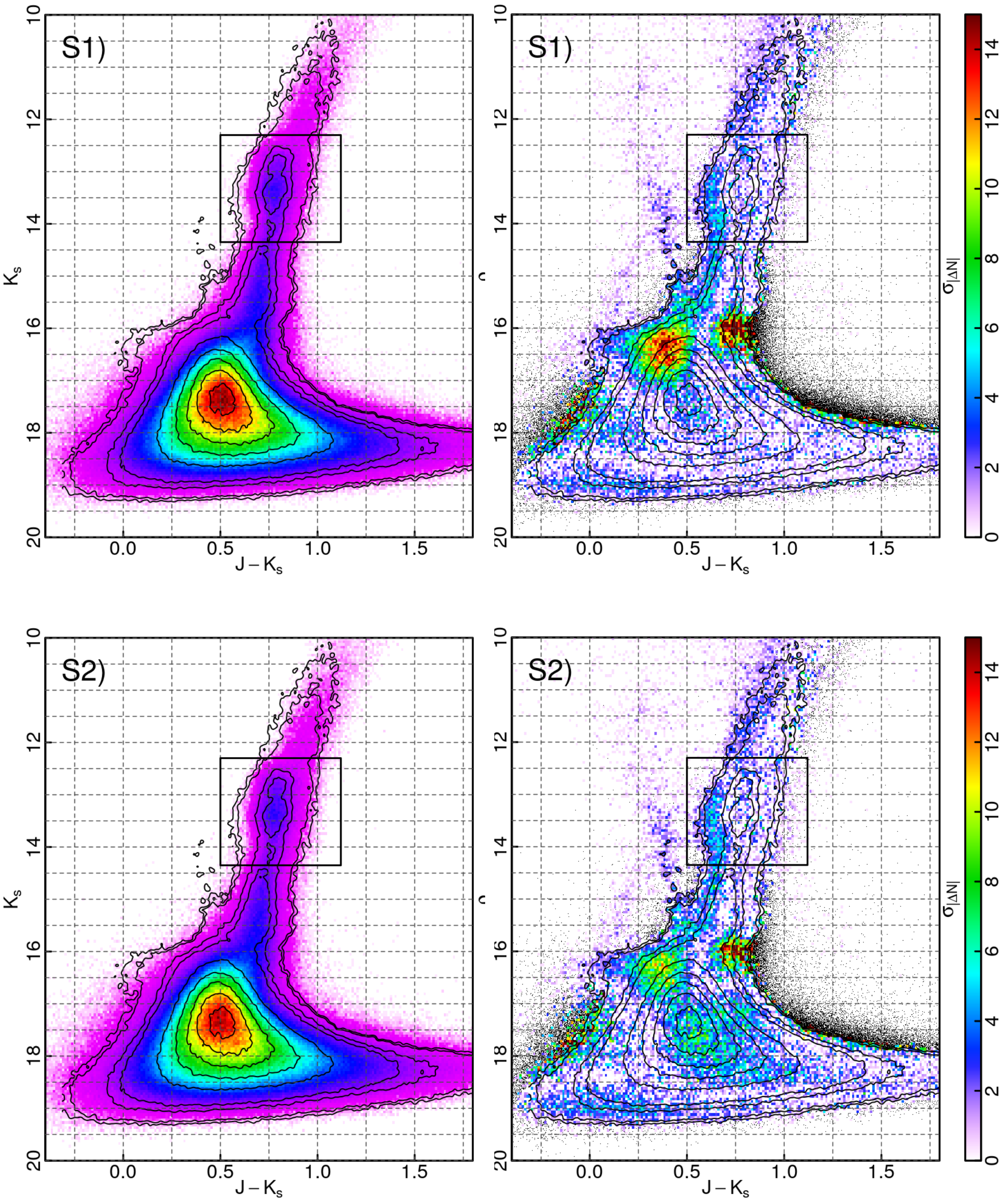

Figure 4.4: Right-panels: synthetic CMDs corresponding to the six scenarios described in § 4.1 compared to the isodensity curves (solid black contours) of the observed clean sample as derived in Fig. 3.5. Right-panels: residuals map providing the discrepancy (e.g. the quality of the fit) between the synthetic and observed CMD. Significant mismatch between the observations and simulations corresponds to $\sigma_{|\Delta N|} \gtrsim 7$. Regions of the CMD populated exclusively by simulated stars are marked with black dots. The box marks the region of the CMD used define h in 4.3

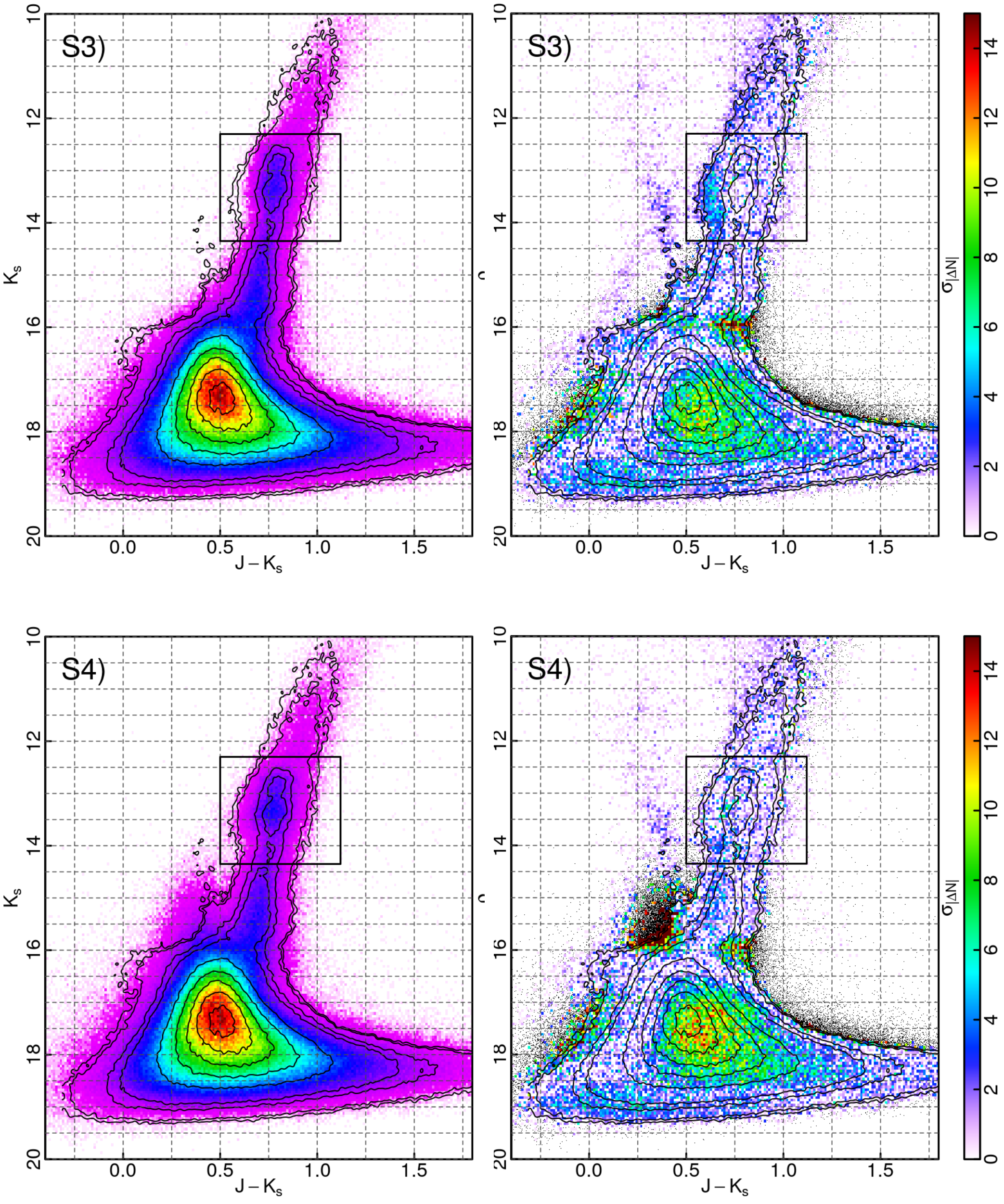

Figure 4.4: (continued)

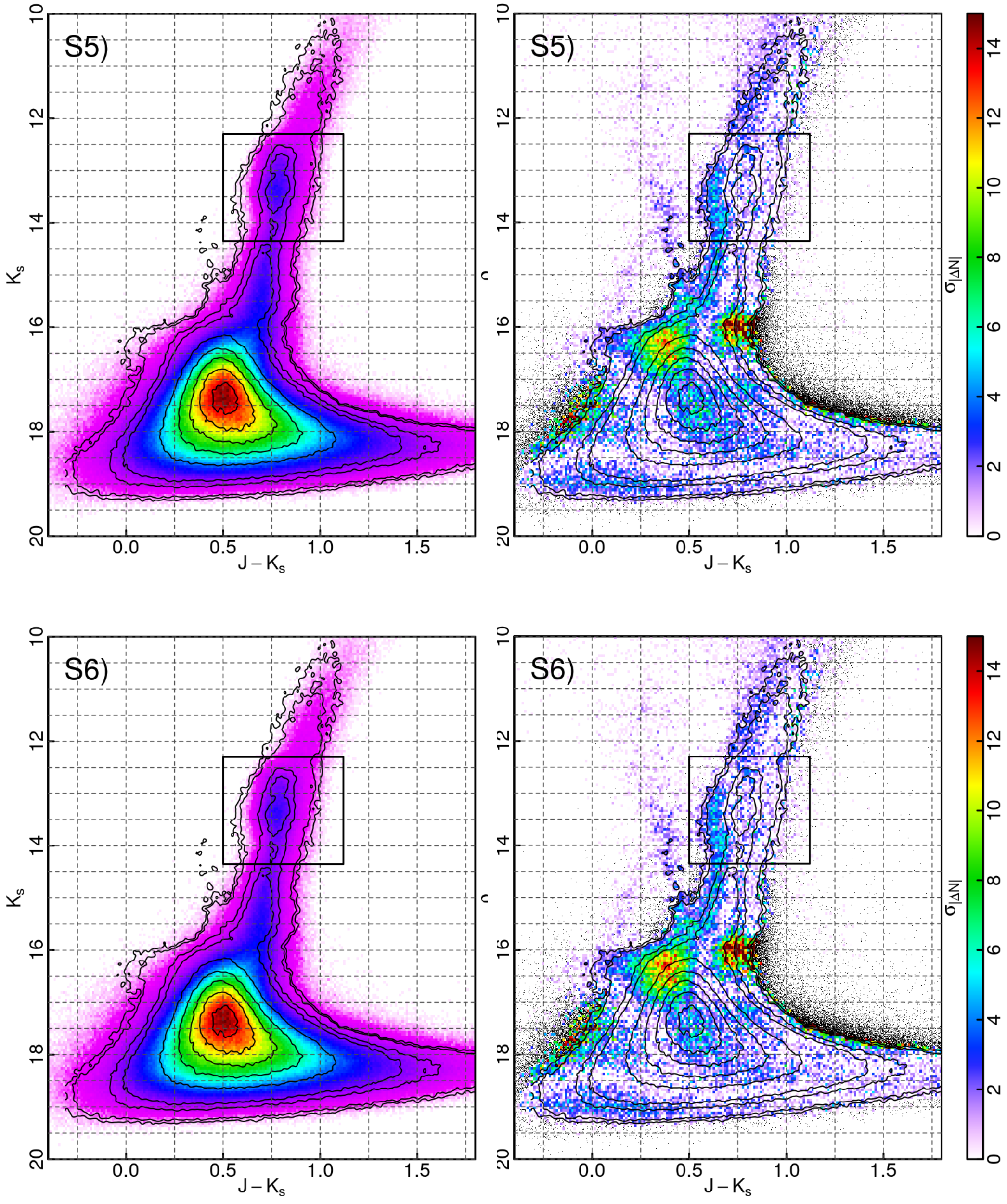

Figure 4.4: (continued)

Following this approach, the perfect match between simulation and observation should have a residuals map that is characterized only by noise, hence by the lack of any structures.

The residual maps shown in Figure 4.4 have been scaled to the same color-magnitude window and identical σ ranges, hence they can be directly compared against each other. Because for $\sigma_{|\Delta N|} \lesssim 6$ there seems to be no structure to the residual map, but rather what seems like a noisy pixel-to-pixel variation, to be conservative the signal of a given feature in the map is considered significant if $\sigma_{|\Delta N|} \gtrsim 7$ (i.e. from green to red according to the adopted color code in Figure 4.4). In addition, it is worth mentioning that because the residuals map by construction measures the absolute difference between simulation and observations in each color-magnitude bin, any difference (i.e. excess or deficit of stars per color-magnitude bin) always shows up as a positive $\sigma_{|\Delta N|}$ (i.e. $\sigma_{|\Delta N|} > 0\ \forall(\mathrm{J}, \mathrm{K_s})$). In other words, from the residuals map only we cannot know whether a given structure is an excess or deficit of stars in the simulations compared to the observations. The answer is therefore provided by the comparison between the isodensity contours of the observed CMD over plotted onto the simulation (i.e. left sub-panels in Figure 4.4).

From Figure 4.4 we can rule out the possible presence in the bulge of a significant fraction of intermediate-young populations (i.e. $\lesssim 5\,\mathrm{Gyr}$). In fact, the residuals map of S3 and S4 shows a significant ($\sigma_{|\Delta N|} \gtrsim 8$) mismatch around the expected MS-TO (the roundish structure that coincides with the highest isodensity contours). In addition, the S4 scenario predicts the presence of a large number of stars brighter than $\mathrm{K_s} \sim 16$ and $0.25 \lesssim \mathrm{J} - \mathrm{K_s} \lesssim 0.5$. which are not observed (shown as small black dots in the residuals map of S4 in Figure 4.4).

On the other hand, the case of a purely very old bulge, represented by simulation S1, provides a good match of the region around the MS-TO, but significantly ($\sigma_{|\Delta N|} \gtrsim 12$) underestimates the number of stars observed at $16 \lesssim \mathrm{K_s} \lesssim 16.5$ and $0.25 \lesssim \mathrm{J} - \mathrm{K_s} \lesssim 0.5$ (reddish spot in the S1 residuals map in Figure 4.4). The region at the base of the RGB, $(\mathrm{J} - \mathrm{K_s}) \sim 0.75$ and $\mathrm{K_s} \sim 16$, is neither well reproduced, but the presence of this mismatch in all simulations suggests that it is an artifact caused by the decontamination procedure. In fact, it corresponds to the bright end of the local M dwarf distribution clearly observed in the disk fields as the reddest vertical sequence around $(J - K_s) \sim 1$. As such, even if its intensity varies across the simulations, we refrain from taking it into account for the selection of the best-fit model.

When considering a slightly younger age (i.e. $\sim 7.5\,\mathrm{Gyr}$) for the MR component, as in S2, S5 or S6, the overall match between the synthetic and observed population further improves, while the region around the MS-TO is still well matched. Indeed, the deficit of synthetic stars present in S1 is considerably reduced, up to a factor of ~ 2 in the S2 case. This would make S2 the best-fitting scenario, however we should stress that in all simulations presented here we have ignored the presence of BSS even though they have been observed in bulge fields (Clarkson et al., 2011).

To qualitatively constrain the BSS position in the $[\mathrm{K_s}, \mathrm{J} - \mathrm{K_s}]$ plane, we have used the near-IR CMD of the bulge cluster NGC 6624 from Saracino et al. (2016), which includes BSS identified from UV and optical (Ferraro *private communication*). When accounting for the difference in distance and reddening between the cluster and the b249 field, we found that the BSS are approximately located in the region where S1, S2, S5 and S6 show a deficit of simulated stars with respect to the observed ones. Therefore, which simulation among scenarios S1, S2, S5 and S6 best-fits the observed CMD, depends upon the number of BSS present in the field.

According to Clarkson et al. (2011), the bulge field BSS frequency ($\mathrm{S_{BSS}}$), defined as the number of BSS scaled to the number of RC stars, is between 0.3 and 1.23, while for the clusters Ferraro et al. (2003) found $0.1 \lesssim \mathrm{S_{BSS}} \lesssim 1$. However, based on a photometric study of a sample of globular clusters and dwarf spheroidals Santana et al. (2013, 2016) found that the number of BSS grows almost linearly with the total stellar mass of the system, therefore the BSS frequency in dwarf spheroidals is much higher than in clusters. In addition, when considering that the dynamical state of the bulge is expected to be more similar to that of dwarf spheroidals rather than clusters, it is plausible to believe that the BSS frequency provided by Clarkson et al. (2011) could be an underestimation for the bulge.

For the case of the b249 field, $\mathrm{S_{BSS}} = 1.23$ would imply the presence of $\sim$32,000 BSS. Of course, to properly take into account the BSS in the simulation we would need to have robust information on their density distribution per color-magnitude bin, which at the moment is still lacking. In principle, this can be obtained by using a large and statistically robust sample of observed BSS (Ferraro et al. *in prep*). Here we just stress that taking into account a population of $\sim$32,000 BSS uniformly distributed within the region defined by the cluster NGC 6624, would have the effect of removing completely the mismatch between the observed and simulated CMD for the S2. On the other hand, higher BSS frequency values $\mathrm{S_{BSS}} = 1.66, 2.82, 3.03$ need to be assumed to remove the stars deficit highlighted in the residuals map of scenarios S5, S6 and S1, respectively Finally, the S3 and S4 scenarios are incompatible with any value of BSS frequency.

The results from S5 and S6 with BSS addition would be in excellent agreement with the very recent study by Renzini et al. (2018) based on very deep HST CMDs of four fields located along the bulge minor axis and $-2° \lesssim b \lesssim -4°$. By using a combination of UV, optical and near-IR filters they have photometrically tagged all bulge field stars, and compared the luminosity function of the most MR and MP with simulated old and intermediate-age population. They found that MR and MP populations appear essentially coeval and consistent with a $\sim$10 Gyr old population.

Because BSS mimic a rejuvenated population due to the mass transfer, ignoring their presence could partially be one of the reasons that led previous studies to advocate for the evidence of very extended star formation in the bulge (e.g. Bernard et al., 2018). Therefore, including BSS in the simulation of synthetic CMDs could potentially reduce, or even remove, the tension between different studies based on the photometric approach.

On the other hand, this alone still does not reconcile the discrepancy between the photometric and spectroscopic age measurements.

In fact when we allow for the presence of a significant fraction (i.e. $> 20\%$) of intermediate--young stellar population (i.e. > 5 Gyr as in scenarios S3 and S4) the synthetic CMD does not provide a reasonably good fit of the observations.

It should be stressed here that the comparison between simulations and observations has been performed on the properties of the entire CMD, not only in terms of color spread of the MS-TO, as done in some previous studies (e.g Haywood et al., 2016).

Stars as young as 1 Gyr up to ~ 3 Gyr occupy a region in the CMD that is not populated in the observations, even considering the CMD before decontaminating it. Because the observed bulge sample is statistically very robust ($> 1.6 \times 10^6$ stars) due to the large surveyed area ($\sim 1.8\,\mathrm{deg}^2$), even a small fraction (i.e. $\gtrsim 10\%$) of such young component, if present, would have been detected in the observed CMD, providing they are not in the disk control-field exactly with the same proportion (which is very unlikely). This means that we can safely discard the presence of relevant components within that age range.

4.2 Extending the study to other fields

With the ultimate goal of studying the possible age variation across the bulge we have selected few fields sparsely distributed in the outer and inner regions, where a rather low and stable reddening is found.

For each field, we apply the decontamination procedure defined in §3, and disperse the IAC-STAR atlas to produce a set of synthetic populations that carry the same completeness, photometric and systematic uncertainties of the observed field as described in §4.1.1.

The age of the observed population in each field is constrained following two different approaches. The first method is very similar to that applied on b249, the proof-of-concept in §4.1, therefore using the MDF from the closest GIBS field to constrain the metallicity of two synthetic populations (i.e. MR and MP component). Such components are then reproduced by mixing an 11 Gyr MP population with a set of younger populations for the MR component, taking also into account the BSS contribution.

The second method relies completely on the IAC-POP/Minniac suite to reconstruct the star formation history with no particular assumption on the observed population, hence both metallicity and age are free parameters.

In the following sections, we present and discuss the results of these experiments.

4.2.1 Selected fields

In addition to b249, we select 12 fields for which the corresponding photometric catalog is deep enough to sample the old MS-TO, and thus allowing for a proper age determination. The fields have been selected to coarsely map as much as possible the entire VVV bulge area (see Table 4.1), but also based on their global extinction properties. Specifically, we have chosen tiles showing little differential reddening (i.e. $\Delta E(\mathrm{J}-\mathrm{K_s}) \lesssim 0.1\,\mathrm{mag}$) to ensure reliable disk-decontamination results. Indeed, if the reddening variation across a given tile is small, then we expect the reddening of the bulge and disk components observed across the line of sight to differ by a single value of $E(\mathrm{J}-\mathrm{K_s})$, and therefore ensuring that the considerations described in §3.3.1 hold true.

Table 4.1: Summary of the selected fields for which we estimate the stellar ages. Provided are the tile ID, sky position, mean and standard deviation extinction from §2.7, the mean $\mathrm{K_s}$ of stars with a 50% completeness and finally the total number of stars within the corresponding catalog (without completeness correction).

Name	(l, b)	$< E(\mathrm{J} - \mathrm{K_s}) >^a$ (mag)	$\mathrm{K_s}(p = 0.5)$ (mag)	Detected stars
b243	$(-9.25°, -6.41°)$	0.113 ± 0.024	18.52	1,740,675
b247	$(-3.39°, -6.41°)$	0.105 ± 0.027	18.26	3,367,866
b249	$(-0.45°, -6.41°)$	0.152 ± 0.049	18.03	2,498,831
b256	$(+9.81°, -6.41°)$	0.188 ± 0.034	18.30	2,389,120
b259	$(-6.33°, -5.32°)$	0.206 ± 0.034	18.04	2,757,108
b278	$(+0.98°, -4.23°)$	0.281 ± 0.055	17.25	3,713,572
b283	$(+8.28°, -4.23°)$	0.227 ± 0.042	17.65	3,221,126
b287	$(-6.34°, -3.14°)$	0.446 ± 0.091	17.43	3,301,236
b293	$(+2.42°, -3.14°)$	0.273 ± 0.052	16.82	4,193,637
b306	$(+0.95°, -2.05°)$	0.469 ± 0.111	16.28	4,536,525
b363	$(+2.42°, +2.32°)$	0.731 ± 0.093	16.91	4,463,307
b384	$(-7.79°, +4.51°)$	0.251 ± 0.059	18.23	3,104,244
b396	$(+9.75°, +4.51°)$	0.372 ± 0.056	17.81	2,151,730

[a] Color excess from the stellar average and standard deviation over the whole tile.

Figure 4.5 provides a visual reference of the location and extension of the sample fields by showing the position of the selected tiles within the extinction map already presented in Figure 2.16.

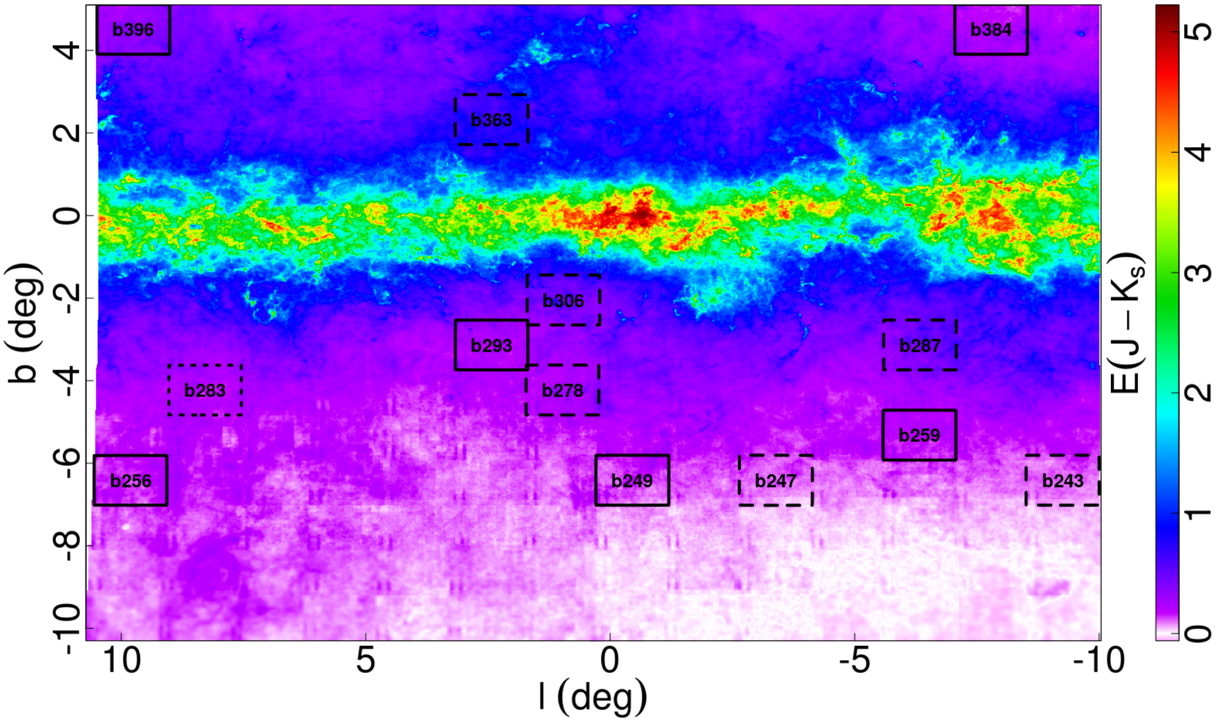

Figure 4.5: Same as Figure 2.16 but highlighting the position of the selected fields where the age determination is provided. The boxes represent the actual coverage of the tiles named within. Fields for which the age estimates are derived by using SFH reconstruction and GIBS prior methods are marked as solid boxes. Dashed and dotted boxes when only GIBS prior, and only SFH reconstruction is used, respectively.

Given the high resolution extinction map (see §2.7) we have at disposal, instead of working with entire tiles we could have extracted subsample of stars from a given region where the reddening is particularly low and stable. However, we must warn that such approach would have a number of undesirable consequences. For instance, if the reddening changes considerably across the tile, it means that the photometric completeness also varies spatially, therefore by using a subsample of the catalog would inevitably require special considerations when dispersing the synthetic atlas.

Another important consideration for the field selection is the actual signal of bulge stars in a given tile, which can be judged at a glance by the number of RC stars in the field CMD. In Figure 2.13 we showed the RC star density dataset from Valenti et al. (2016) for the inner bulge ($|b| < 4°$) and complemented here to cover the VVV bulge area with data from this work. There it can be seen how quickly the RC star number decreases as we move out from the Galactic center and plane. In the case of b249 at $b \sim -6°$ (see Table 4.1) we are already at the level of $\sim$20,000 RC stars, which we take as our standard of quality. At $l \sim 0°$, the number of RC stars drops to $\sim$13,000 at $b \sim -7.5°$, and to $\sim$3,000 at $b \sim -10.0°$. We are thus limiting our selection of fields to $|b| \lesssim 6°$, because having a weak bulge star signal, as traced by the RC star counts, leads to a poor decontamination where the uncertainties of the method are dominant in the result.

Finally, we must also take the completeness level into consideration, even though this criterion in practice is coupled with the extinction one. We stress again here that we want to have the old (>10 Gyr) MS-TO sampled within the 30% completeness contour, without reddening corrections. This is because otherwise the IAC-POP/Minniac method prefers younger solutions, regardless from the actual dominant presence of old stars, essentially because it cannot see the defining feature of the old MS-TO.

4.3 Using the GIBS MDF prior

As mentioned before, in the following we repeat what done for the proof-of-concept, i.e using the GIBS MDF as a prior to construct the synthetic populations. The MDF not only pertains the distribution of the population metallicity, but it also defines the ratio of MP-to-MR stars, which does have an indirect effect on the derived age given that we let the age vary only for the MR component. We apply this method to all fields in Table 4.1 except b283, for which the nearest GIBS field is rather anomalous (MP : MR $\sim$ 5 : 1, instead of the much more common MP : MR $\sim$ 1 : 1)

4.3.1 Building the synthetic sample populations

To exploit the possible presence of age variation larger than what we have found in b249, we perform fits much like in S4, but with MR components of 3, 5, 7.5 and 10 Gyr simultaneously, together with the base 11 Gyr MP. All components are modelled as 600 Myr wide uniform distributions, centred at their respective target age (i.e. 3 ± 0.3 Gyr, 5 ± 0.3 Gyr, and so on). We also allow for a BSS contribution by using the general locus defined previously, but shifting it in color and magnitude so that its relative position to the observed RC is always the same. This is to account for (mean) distance and reddening differences between the sample fields.

Then, for each field we have a set of 8 independent synthetic populations: 4 for each metallicity component, with various different number of stars within.

It is important to keep in mind the limitation in metallicity mentioned in §4.1.1. For b249 the corresponding GIBS MDF is well within the limits imposed by the IAC-STAR atlas, however in several other GIBS fields, the MR MDF extends considerably beyond that $[\mathrm{Fe/H}] \lesssim +0.42$ restriction. For b249, for instance, the population loss due to this restriction is of the order of 1%, while most other fields in Table 4.1 lose 10-20%, and four of them (b256, b278, b293 and b306) lose 20-40% in the MR component distribution. In practice, this means that the GIBS MDF cannot be fully reproduced for the MR component, and for example, if a gaussian MDF of mean metallicity μ_M and variance σ_M^2 *lost* its 20% most metal-rich wing, then its new mean metallicity μ'_M would become $\mu'_M \approx \mu_M - 0.35\sigma_M$.

Now, since the MP:MR ratios defined in GIBS are based on RC stars, we need to determine the RC for each population (see §2.6), calculate the number of RC stars N_{RC}, and mix the MP+MR sets so that $N_{\mathrm{RC,MP}} : N_{\mathrm{RC,MR}}$ equals MP:MR from GIBS in all mixes. Even though the individual components are corrected (i.e. the relative number of RC stars are what the GIBS prior defines, regardless of the loss), the resulting global MDF ends up being different to the one listed in GIBS data, but that particular should be of little consequence for the fits.

Finally, the population sets are normalized so that the individual MP components in each one has the same number of stars in their RC.

To account for BSS, an extra component is added in the form of a uniform distribution about the BSS locus, normalized so that it has the same total number of stars as the observed RC. Onward and for simplicity, we will refer to the individual synthetic population mixes (MP+MR) by the age of the MR component (3, 5, 7.5 and 10 Gyr), but bear in mind that there is always an 11 Gyr MP component in all of them.

4.3.2 Fitting an age for the MR component

The fitting procedure is done interactively and iteratively. We start by using only the 10 Gyr MR component to define JK_s offsets to match observed and simulated RCs (interactive). A fit is then done to find a set of scalar values $\{\alpha_i\}$ that relate the 2D histograms of decontaminated observed CMD, the shifted simulation, and the BSS locus set. This is done along all possible values of the 2D CMD histograms, unlike the previous fits in the proof-of-concept (see §4.1), that used only a portion of the RC area. We expect the fit to readily and adequately reproduce RC and MS-TO areas of the observations simultaneously.

The scalar values are set to be always positive $\alpha_i > 0\ \forall i$, and in the case of the BSS an additional constraint is set so that $\alpha_{BSS} = \mathrm{S}_{\mathrm{BSS}} < 1.23$, which is the same limit imposed in §4.1.4 for the proof-of-concept, as the maximum BSS-to-RC stars ratio from Clarkson et al. (2011), with $\mathrm{N}_{\mathrm{BSS}} \lesssim 1.23 \times \mathrm{N}_{\mathrm{RC}}$.

The residual between the observation and the synthetic simulation is then converted into a bootstrap map constructed in the same fashion as detailed in §4.1. If this CMD, constructed only from > 10 Gyr populations, displays a significant discrepancy with the observations then we proceed with the next iteration, this time adding a 7.5 Gyr component to the fit and repeating the procedure once again (i.e. MR 7.5 and 10 Gyr, plus 11 Gyr MP and BSS, all with their own α_i value).

If the residual in the new case is not satisfactory, then we add the next younger component and repeat until we have either reached an adequate residual or added all available components (3, 5, 7.5 and 10 Gyr MR) to a simultaneous fit. In some cases this procedure does not completely erase the discrepancy between observed and simulated, even if a very young (∼ 3 Gyr) population is added. However, when the discrepancies between the observed and simulated CMDs occur sufficiently close to the vestigial disk sequence, they

Table 4.2: GIBS MDF prior fitting results summary. Detailed are the tile ID, position, mean age (plus-minus its standard deviation), and f_{young}, the fraction of stars younger than 6.5 Gyr necessary for the fit (see text). Relevant values have been corrected for incompleteness.

Name	(l, b)	$< Age >^a$ (Gyr)	f^a_{young}
b243	$(-9.24°, -6.37°)$	10.87 ± 0.70	-
b247	$(-3.36°, -6.38°)$	9.47 ± 1.77	-
b249	$(-0.45°, -6.38°)$	9.43 ± 1.99	-
b256	$(+9.80°, -6.39°)$	10.25 ± 1.24	-
b259	$(-6.29°, -5.30°)$	9.45 ± 1.82	-
b278	$(+0.99°, -4.23°)$	8.87 ± 2.49	-
b287	$(-6.29°, -3.11°)$	8.03 ± 3.41	0.19
b293	$(+2.43°, -3.12°)$	9.06 ± 2.89	-
b306	$(+0.97°, -2.03°)$	7.90 ± 3.90	0.39
b363	$(+2.41°, +2.32°)$	7.65 ± 3.73	0.45
b384	$(-7.76°, +4.49°)$	9.54 ± 1.90	-
b396	$(+9.74°, +4.49°)$	10.38 ± 1.36	-

[a] From all stars in the simulation with $p > 0.3$.

can be at least partly be considered as artifacts induced by an imperfect decontamination, rather than actual signals from a young population component.

The results of the fits are given in Table 4.2, where we provide for each studied field the mean age (taken as the mean age of all the stars in the simulation with completeness above the 30% level, and corrected for completeness) with its standard deviation. In addition we list the relative percentage of stars younger than 6.5 Gyr (f_{young}) corrected for completeness.

The residuals between the observed and best-fit model CMDs are shown in Figure 4.6. In the residual map of all fields one can appreciate the persistent disk CMD vestiges that remain after the decontamination, as a thin projection of the young MS at $(\mathrm{J} - \mathrm{K_s}) \sim 0.5$ mag and $\mathrm{K_s} \lesssim 16$ mag. In addition, we always note a relatively significant roundish feature concentrated near the blue bright end of the MS, and again notably close to the vestigial disk sequence. We have assumed in the fit that this is caused by a deficit of young stars in the synthetic CMD, but due to its particular placement, we cannot discard that it may be at least in part related to a decontamination issue. Nevertheless, it seems to be within acceptable levels ($\sigma_{|\Delta N|} \lesssim 7$) for almost all the fields in Figure 4.6.

There are also evident excesses of simulated stars at the red and/or blue edges of the MS locus. These are likely produced due to an imperfect decontamination. Indeed, due to the rapidly increasing errors towards faint $\mathrm{K_s}$ and redder colors, the decontamination procedure will inevitably remove stars around the edges of the CMD. These artifact is often paired with another excess near the red *knee* at the base of the RGB, most likely caused by the local K- and M-dwarf population present in the control disk fields (see §2.4.1).

In b243 and b247, the two fields with the lowest bulge signal, we can also note a relatively small yet extended discrepancy in the faintest part of the CMD ($\mathrm{K_s} \gtrsim 18$). We assure that this difference is related to nothing else but the shift that was applied to the already dispersed synthetic CMDs at the time of RC matching. To be more specific, since the dispersion is done at a very specific $\mathrm{JK_s}$ reference, it is also tied to a very specific completeness effect. For instance, if we shift the synthetic upwards (i.e. brighter $\mathrm{K_s}$), the stars in the faint limit of the CMD would become brighter, thus improving their completeness relative to the observed CMD and changing their dispersion properties in general. In the fitting procedure, these shifts are applied without such considerations because are thought to be sufficiently small to produce negligible effects. However the variation of the completeness in the peripheral fields at the faint limit is so strong (compare completeness gradient in Figure 2.8, panels for b208 and b292) that this assumptions breaks down moderately. Nevertheless, it should be noted that the described discrepancy is still below the value at which we consider a signal to be significant (i.e. $\sigma_{|\Delta N|} \sim 7$).

When excluding the strong residuals in Figure 4.6 mentioned above and likely introduced by the decontamination procedure, there is a general lack of additional significant signals above the noise pattern, thus suggesting that in most cases the age mix of the synthetic populations provides a good representation of the observed bulge stars.

However, some notable deviations from the general good agreement between the synthetic and observed CMDs are the central-most fields, b293, b306 and b363, where not only there appear to be considerable differences in the MS area, but also around the RC. More specifically, the discrepancies are located between ~0.5-1 mag fainter than the RC overdensity. Most evident in b306 and b363, this feature below the RC is likely not related to an actual population difference, but to an improper modelling of the RC. Possibly, we would need more than just the RGB-bump to justify that difference.

Additional strong discrepancies arise in b306, where despite the youngest MR component (3 Gyr) being dominant, it was not enough to reconcile with the observations, even with BSS considerations. In addition, a new feature appears at the faint end of the CMD, which can be only partially explained by some completeness mismatch from the shift applied in the fitting procedure. Indeed, it is still too strong and localized to be disregarded as such. For the time being, we refer to them as *bad fits*, but we have found an alternative explanation regarding unaccounted effects caused by the highly crowded fields near the Galactic center, which we explore in §4.5.1.

4.3.3 About the effect of BSS and short discussion

As discussed earlier (see §4.1.4), the effect of adding BSS to the fit essentially covers roughly the same discrepancy than adding a younger component would. That is, we can get similar residuals of the fit with BSS, than a fit without BSS but overall younger age.

Even a moderate BSS frequency ($S_{BSS} < 1.23$) can supply for a significant fraction of young stars in the fit. For the peripheral fields (roughly within 3.5 deg from the Galactic center), it can reduce the mean age of the mix by up to 1 Gyr, and also completely removing

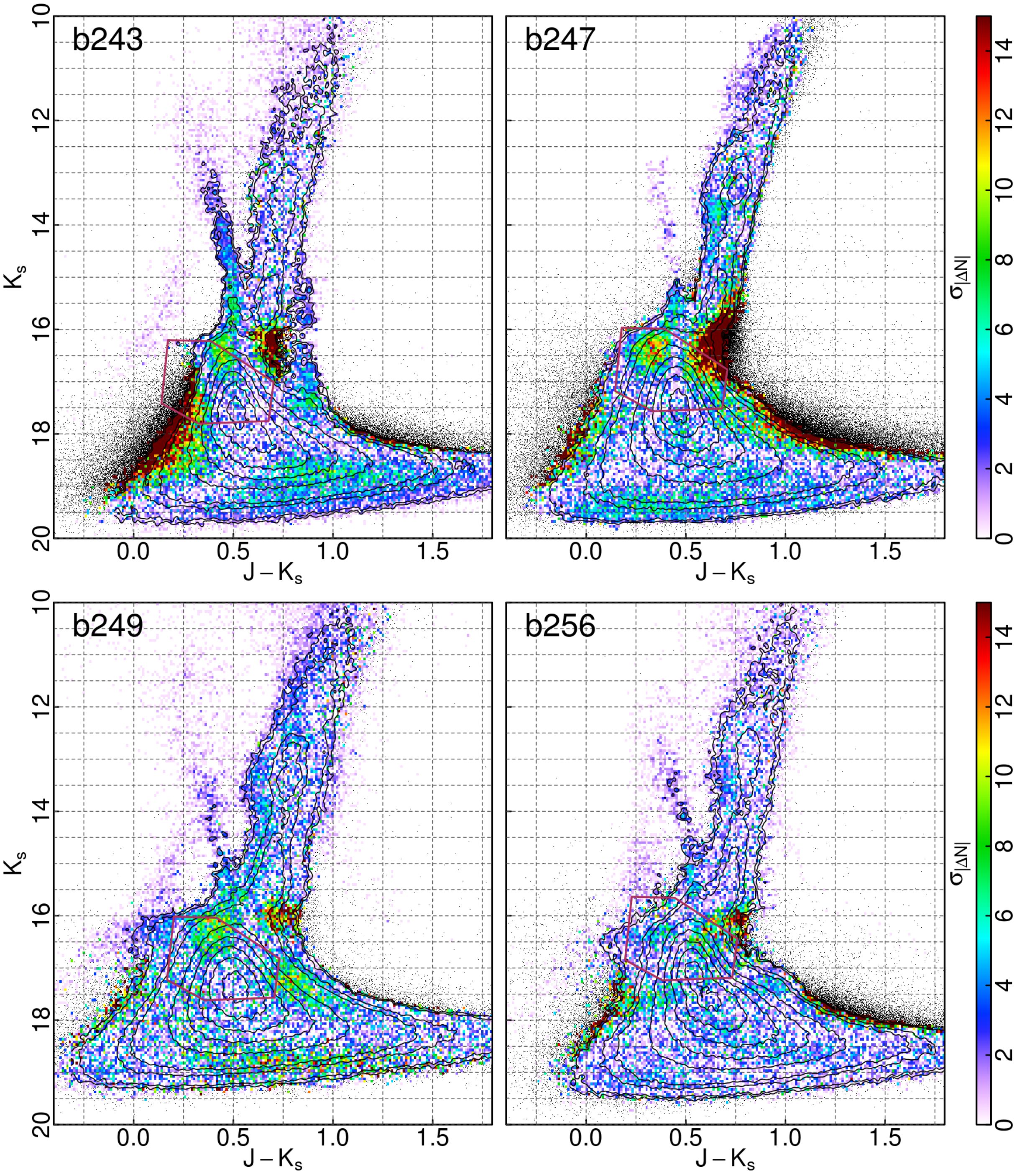

Figure 4.6: Observations vs. Simulations with GIBS MDF prior, fitting a MP component of 11 Gyr plus a mix of MR down to 3 Gyr (see text). The color coded maps are constructed in a similar fashion as reported in §4.1 and shown in the right panels of Figure 4.4. The solid lines follow the isodensity contours of the observed decontaminated CMD and the black dots display the stars from the synthetic population where no stars are present in the observed decontaminated CMD. Also included in maroon is the locus of the BSS, shifted to match the same relative difference to the observed RC in each case.

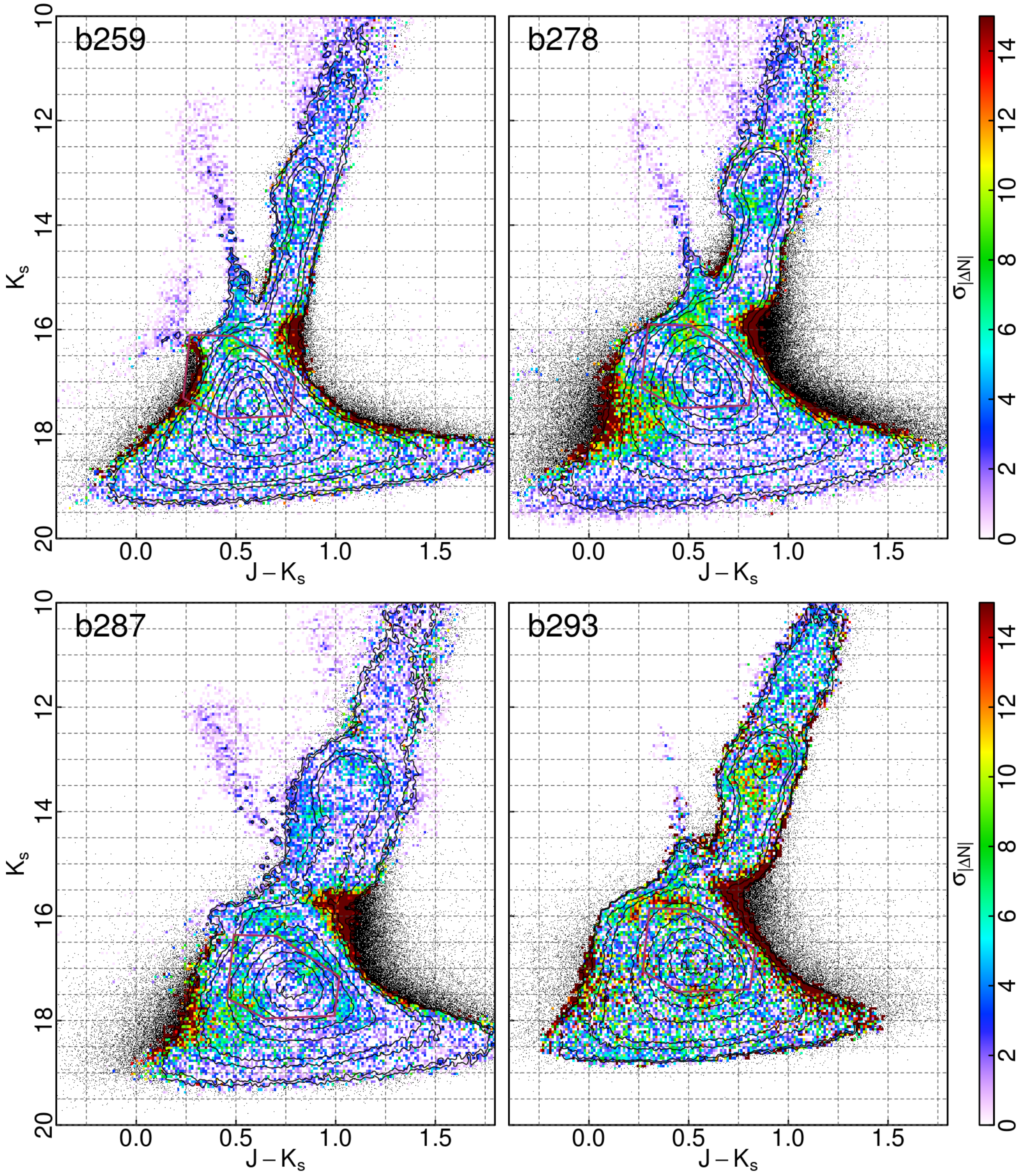

Figure 4.6: Observations vs. Simulations with GIBS MDF prior (continued).

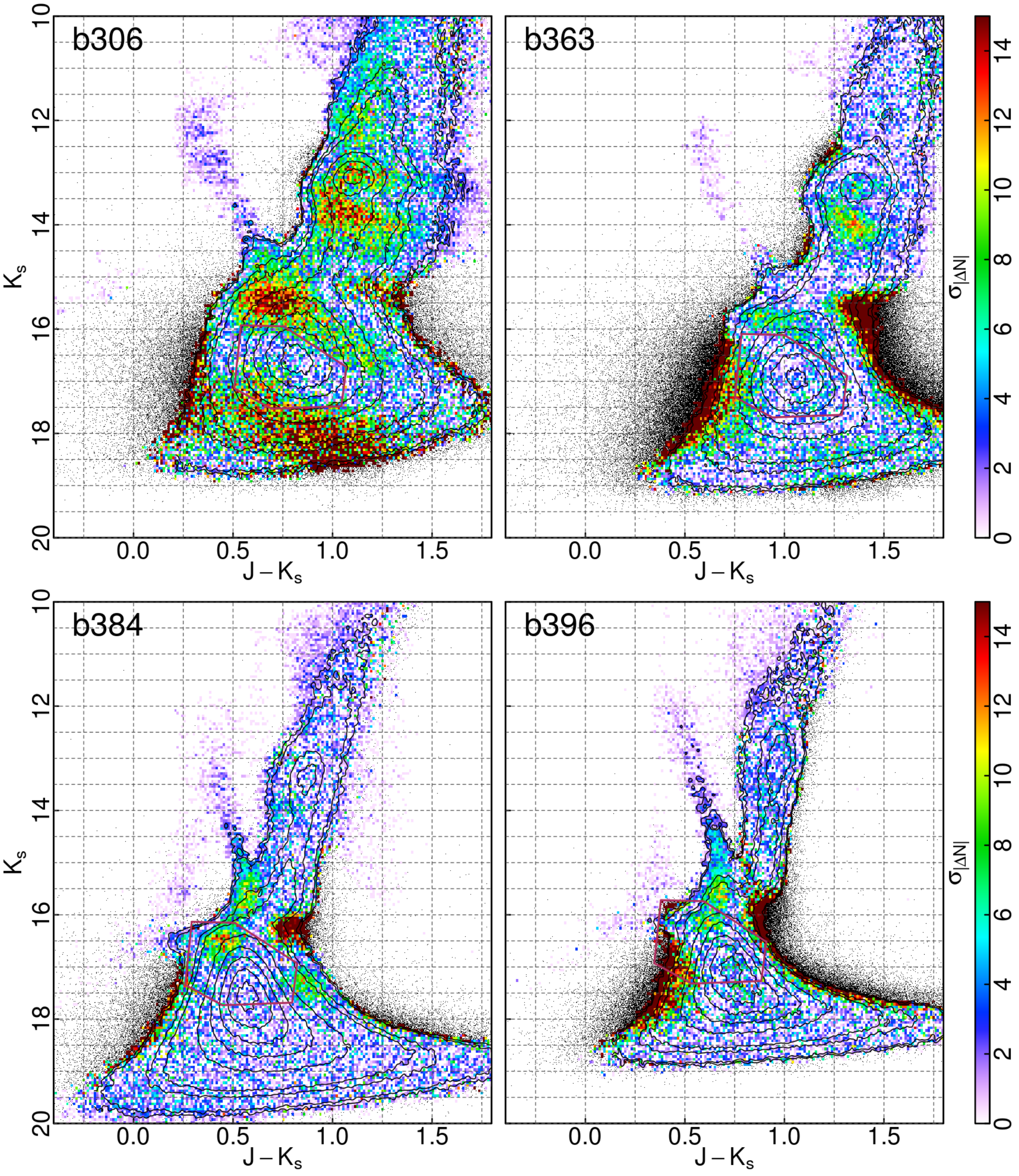

Figure 4.6: Observations vs. Simulations with GIBS MDF prior (continued).

the strong discrepancy that would require the presence of a population younger than 7 Gyr.

However, for the three innermost fields, the locus of the BSS falls near the *hotspot* in the Hess diagram, rather than in the blue and bright edge of the MS-TO apparent location, thus reducing its effect in mitigating the need of a young population.

For b293, the selected limit for S_{BSS} is still sufficient to create a comparatively similar residual to that of a mix that would include $\sim 37\%$ of stars younger than 7 Gyr.

We ought to reiterate here, that the approach we use to account for BSS is quite approximate, and a more detailed understanding of this population would be required in order to produce more deterministic results. However, because their presence in the bulge has been observed and it is also expected by stellar evolution theory we argue that studies aimed at deriving stellar ages cannot simply ignore the contribution of BSS. The current uncertain approach is still more physically realistic and valid than a method that completely ignores their presence.

4.4 Reconstructing the SFH with IAC-POP/Minniac

In the following sections we present the determination of the stellar age in the same fields by using a complete ignorance model provided by the IAC-POP/Minniac suite, where metallicity and age are left to vary in the fitting procedure, and therefore with no particular assumption attached to them. In principle, the results of this approach produce reconstructed SFHs of the studied fields. However, because the selected fields are only marginally eligible for such reconstruction due to the completeness restrictions, and the lack of α-enhancement tracks for the metal-poor populations, we have opted to use only the marginalized age distribution provided by the code byproducts. Nevertheless we do show the complete result here, together with the respective residual map in a similar construction as previously done in §4.3.2.

A detailed description of the IAC-POP/Minniac suite is given by Aparicio & Hidalgo (2009); Hidalgo & Aparicio (2016), however here we provide a brief description on how the code works, what it does and what we can expect from.

4.4.1 General principles of the code

The IAC-POP/Minniac suite can take an atlas of synthetic populations with a convenient SFH, $\Psi(t, Z)$, and fit it to observed CMDs. One of the strengths of the code is the ability of generating not *the* solution for the ensemble, but rather providing an average solution from a set of small perturbations of a central set of parameters.

The individual solutions are handled by a genetic algorithm that probes the sample space given an initial grid of ages and metallicities provided by the user. The perturbed solution comes from small (also input) changes in the age-metallicity grid, and color-magnitude shifts, which should in principle help to provide a rather optimized solution with respect to the restrictions of the initial parameter choice. The results are expected to have less dependence on the possible sub-optimal choice of the grid position, or distance and reddening calibrations done to match observations with the synthetic population atlas.

Each set of perturbations then produces a solution, which can then be smoothed (averaged) to get the most adequate solution in terms of color-magnitude shift, and a higher resolution in age-metallicity space.

Together with other sub-products, the main result of this algorithm is a surface in age-Z, that can be translated into a SFH by means of the mass integral from the atlas. It is then possible to get the marginalized distributions of age and Z individually, which are what we used in this work.

The uniform SFH function we mention is in practice the IAC-STAR atlas we describe in §4.1.3 and previous sections, which again, carries not only the model information but considers several observed characteristics of the field it refers to (distance dispersion, differential reddening, etc).

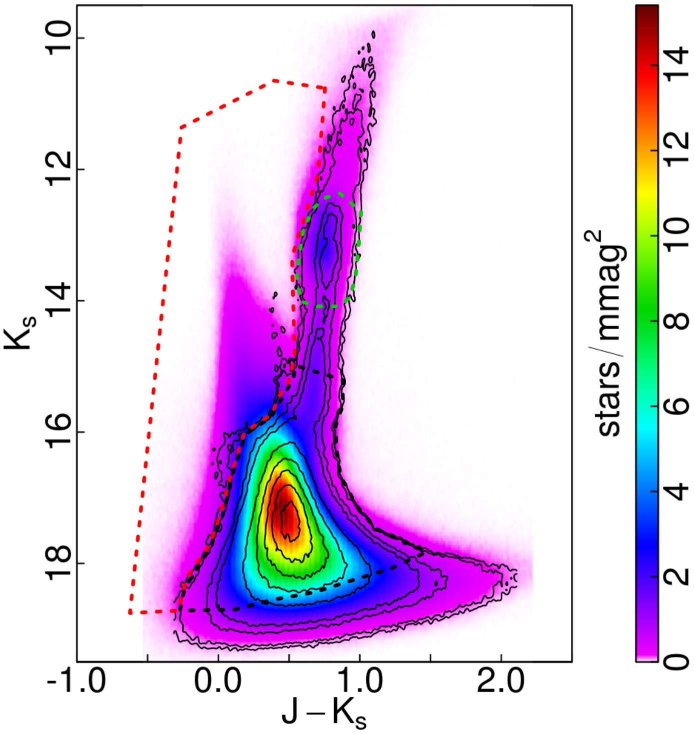

Figure 4.7: Bundle selection example for b249. The Hess diagram is from the processed atlas. The solid contours are from the observed decontaminated CMD for b249. The black dashed line defines the main bundle containing MS-TO locus, portion of RGB and limited by the faint end by the 30% completeness limit. The exclusion bundle, taking out the empty space where no stars are observed is marked with the red dashed line, while the RC area is enclosed in green.

4.4.2 The constraints

IAC-POP/Minniac works better when limiting its working phase space. Age and Z are as broad as possible, but instead of providing as input the whole observed+synthetic CMD ensemble we can make intelligent cuts in the color-magnitude space for both. This is meant to account for the exponentially increasing number of stars as K_s becomes fainter, and the subsequent change in the minimum bin size in color-magnitude which would contain a significant number of stars for a 2D histogram comparison.

For example, we can limit our input to the MS-TO sequence locus, or even better, to the general area in the CMD where we expect the MS-TO to be. The main *bundle* (i.e. constraint) is mostly limited by the outer contour of the observed decontaminated CMD, by the 30% completeness line on the faint end, and by a short section of RGB at the bright end. This usually means a bright limit at $K_s \sim 15$.

We can also add an exclusion bundle, which would tell IAC-POP/Minniac what is absolutely out of the question. That is, we can select and cut out the areas of the CMD, where we have no stars in the observations, but we know there can be from the synthetic atlas. This effectively introduces an educated bias into the reconstructed SFH, because we can choose an empty section in the observed CMD that also limits the minimum age expected in the result.

As a third bundle, we choose a small area surrounding the observed RC. This contributes only minimally to the age-Z solution, but hopefully it limits the possible shifts in color-magnitude of the perturbed solutions, and from the fitted composite population. Additionally, it help finding the old metal-poor component we need to match RC shapes.

An example of this bundle set is shown in Figure 4.7 for the case of b249.

4.4.3 Reconstructed SFH of the sample fields

We perform the SFH reconstruction only on 9 fields listed in Table 4.1 (i.e. b293, b249, b256, b259, b283, b306, b363, b384, b396), mostly because of time constrains. For these fields we produce 24 perturbed solutions from a combination of color-magnitude shifts, and small changes in the age-Z grid. These solutions are then smoothed out via averaging into a final SFH reconstruction, presented in Figures 4.8 to 4.15.

For most of the peripheral fields (b249, b256, b259, b384) the results provided by the SFH reconstruction are generally good, as one can seen from the residual maps. The residual maps of these fields display some of features discussed in §4.3.2 that are likely caused by the decontamination procedure, rather than by a mismatch of populations with different age and/or metallicity (i.e. the vestigial young disk MS, excess simulated stars around the red edge of the CMD, K+M dwarf sequence signal, etc). We must clarify here, that the actual fitting is done wholly on IAC-POP/Minniac side, but since the code can add small shifts in color and magnitude by default, we had to recenter the RC between observation and solution CMDs for all cases for sake of comparison. Moreover, due to the nature of the IAC-POP/Minniac fitting, it would favor reduced discrepancies in the $K_s \gtrsim 16$ region, often incurring in marked and unacceptable RC discrepancies. For this reason, we have reverted to the RC normalization as we did for the proof-of-concept simulations in §4.1.4. Both post-fitting touches (RC shift and re-normalization) and the color-magnitude shifts applied by IAC-POP/Minniac (compounded by the limitation imposed by the bundling) are possibly responsible for some of the marked discrepancies for $\mathrm{K_s} \gtrsim 16$ areas in some fields (e.g. b283, b396). However, as we have no access to the fitting procedure itself, we have tried to minimize the residuals in the decontaminated observed CMD, while trusting that the IAC-POP/Minniac suite has done its job at finding the solution within its parameters. All peripheral fields are found to be mostly old (>10 Gyr) with some secondary slightly younger component, but still older than ~ 7 Gyr.

When moving to inner fields this method does no longer provide satisfactory results as the corresponding residual maps are particularly bad, highlighting strong mismatches between the observations and the simulations all around the CMD. Indeed, we have purposely excluded b306 and b363 fields from the sample because of exceptionally bad residuals, leaving only 7 fields with acceptable solutions.

We use the case of b293, one of the innermost fields in Table 4.1, to justify the adopted completeness limit (i.e. $\geq 30\%$ completeness), and to demonstrate what are the effects when a more conservative limit is assumed on fields with marginal old MS-TO completeness. In Figure 4.8 we show the results of the SFH reconstruction of this field. Taking a 30% lower limit in completeness produces a solution in age which is about 60% older than ~6 Gyr, with important contributions of a component somewhat younger than 5 Gyr. However, when the fainter limit of the main bundle is set to the 50% completeness the solution in metallicity remains roughly the same, but the age distribution changes drastically (see Figure 4.9) displaying almost no stars older than 6 Gyr. The residuals in both cases are rather imperfect, worse in Figure 4.9, but overall acceptable and similar.

In light of this example, where a small change in the completeness limit produces such a sensitive variation in the age solution, we have opted to keep throughout the experiments a fainter limit of 30%.

When comparing the results obtained with the SFH method shown in Figures 4.8 through 4.15, and summarized in Table 4.3, to the GIBS prior set, we find an overall good agreement in terms of age distribution, however the comparison in terms of metallicity is not straightforward. This stems from the fact that due to the approximation we had to adopt for the α-enhancement, the MP and MR components from GIBS are not strongly bimodal in [M/H] space (and thus in Z space).

Although for the peripheral fields the two methods provide solutions that suggest a predominant old (>10 Gyr) component, with traces of younger wings, the metallicity distributions are not really consistent. In fact, when the SFH reconstruction method is used, the derived MDF varies from almost exclusively metal-rich (b283 in Figure 4.13) to mostly metal-poor (b256 in Figure 4.11). Of course, this can be the consequence of the age-metallicity degeneracy, or even to the actual resolution we can expect to have in metallicity when this method is applied (i.e. how different is an simple stellar population of a given age and metallicity, to another with slightly different parameters). Nevertheless, we should once again point out that the lack of a bimodal MDF given by a MR and a MP components in the SFH plots is not consistent with what observed spectroscopically by

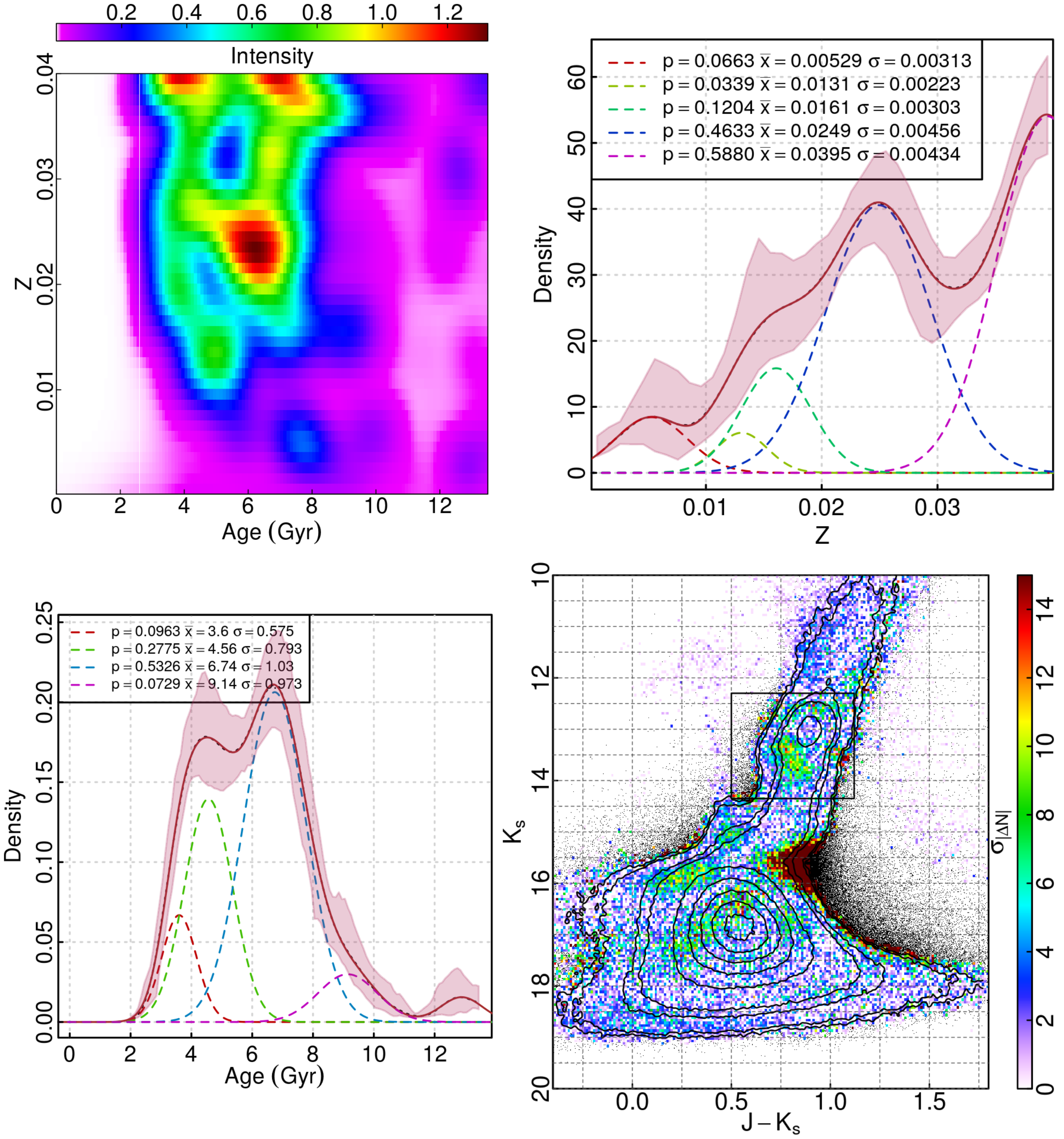

Figure 4.8: (*Top left*): SFH reconstruction detail for b293 with completeness margin down to 30%, showing a color coded map in age-Z plane representing the SFH surface, normalized as a distribution. (*Top right*): Metallicity (Z) marginalized distribution from the SFH reconstruction. (*Bottom left*): Age marginalized distribution. (*Bottom right*): The significance residual map, as defined in §4.1.4 and shown in Figure 4.4; thin solid lines follow the isodensity contours of the decontaminated observed CMD; black dots emerge where in the CMD areas where there are no stars in the decontaminated observed CMD to compare with; thick solid line box marks the area over which h is defined, as per §4.1.4

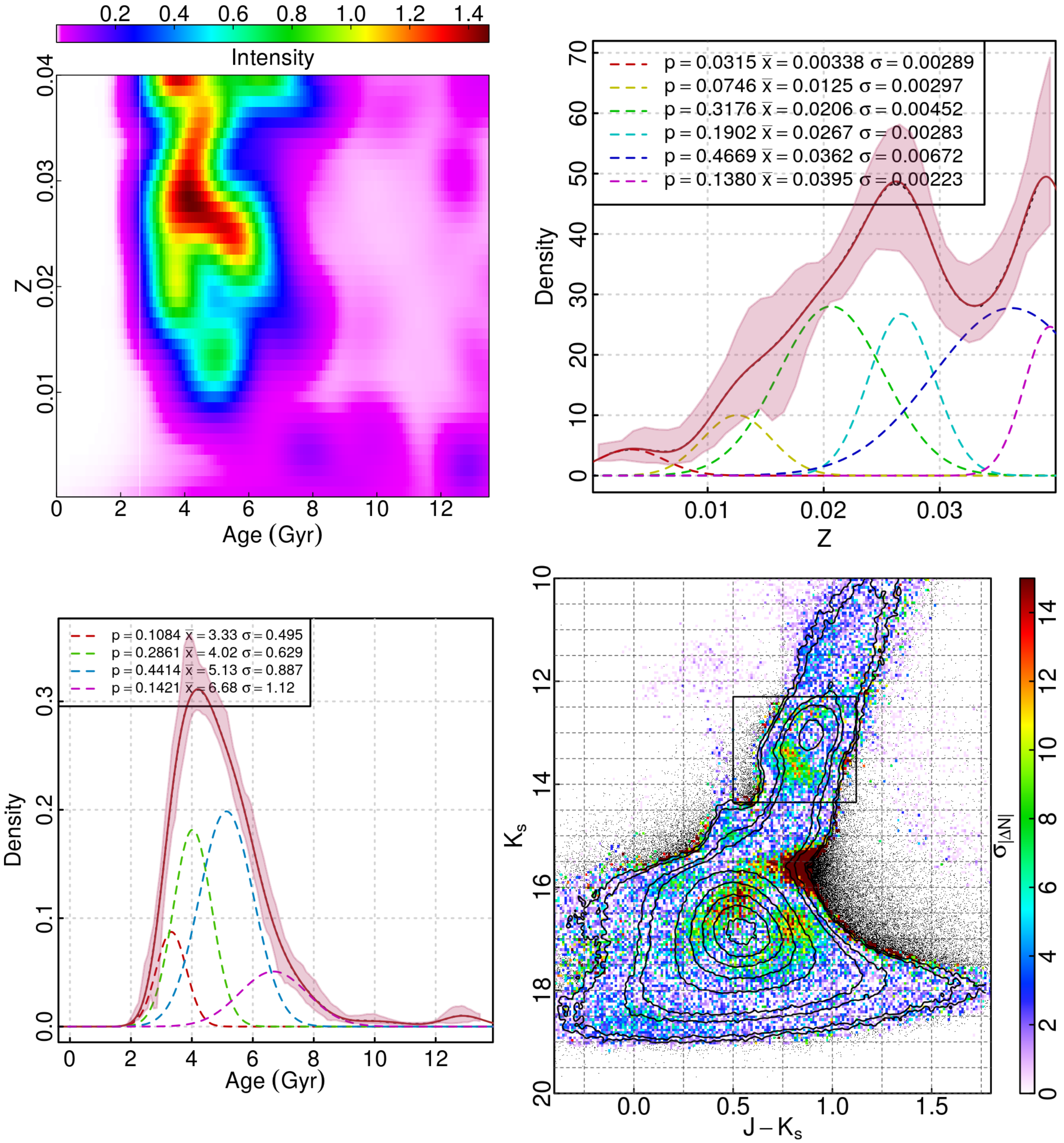

Figure 4.9: Same as Figure 4.8, but with a bundle allowing only down to 50% completeness for b293.

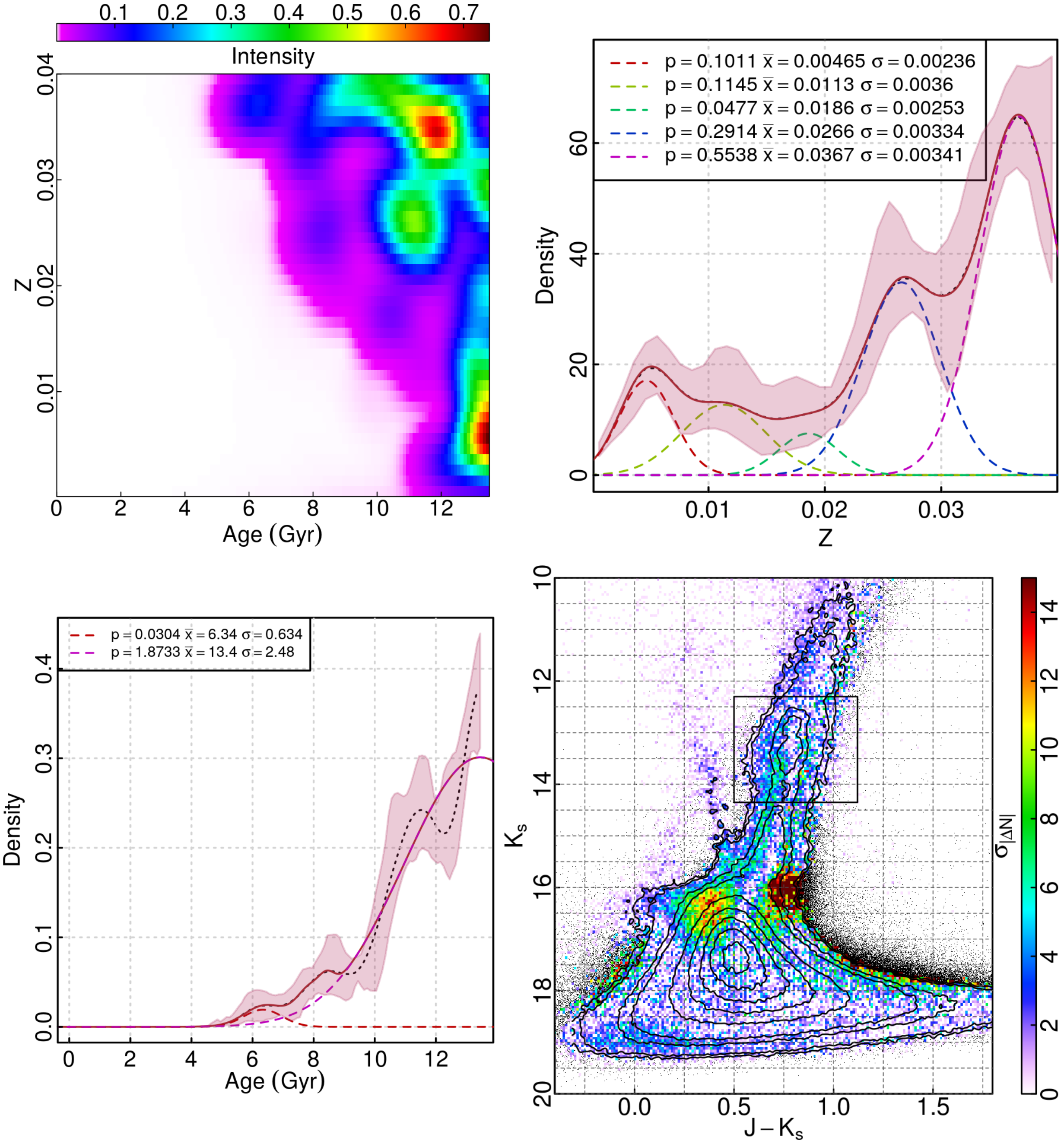

Figure 4.10: Same as in Figure 4.8, but for for b249.

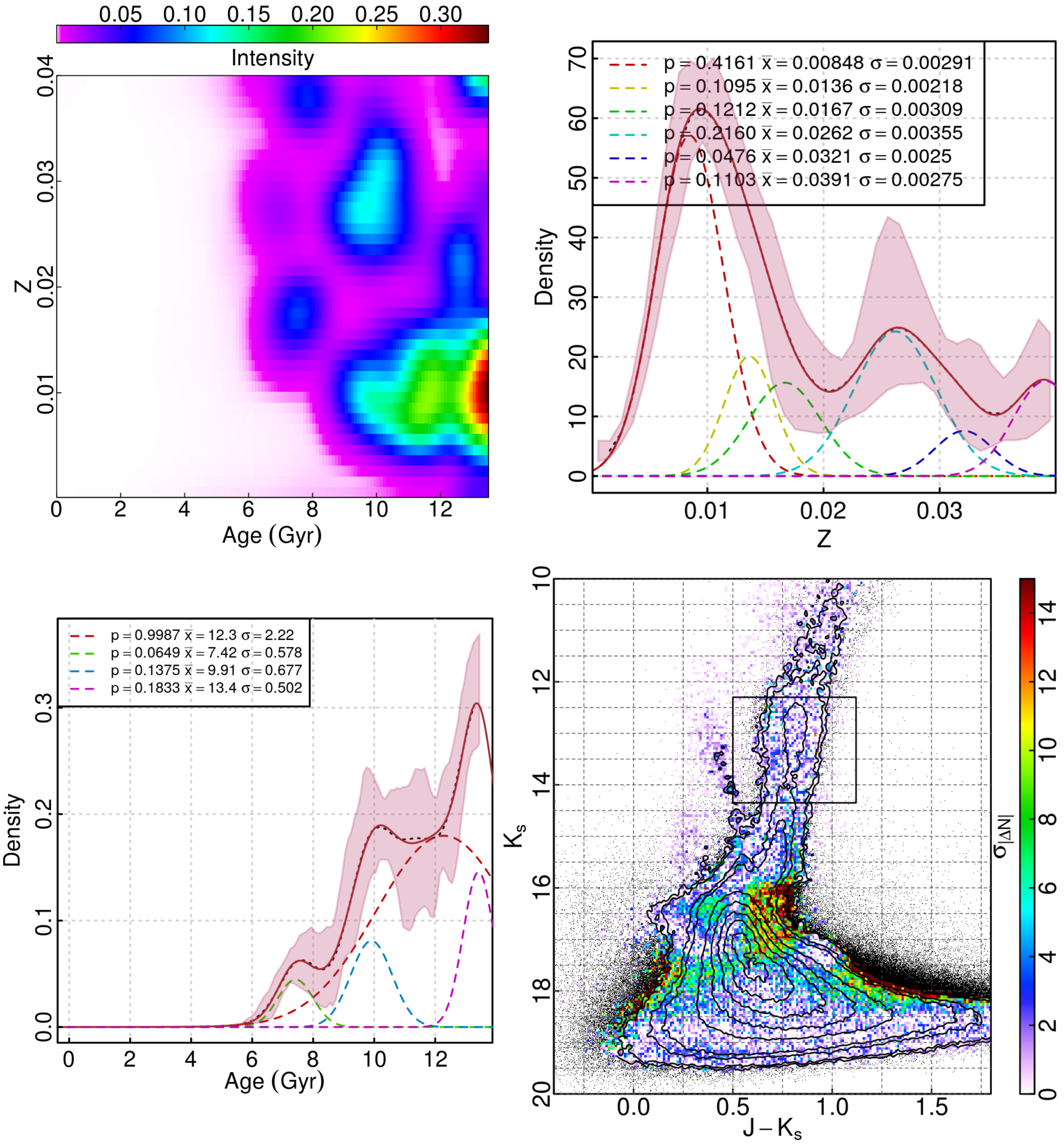

Figure 4.11: Same as in Figure 4.8, but for b256.

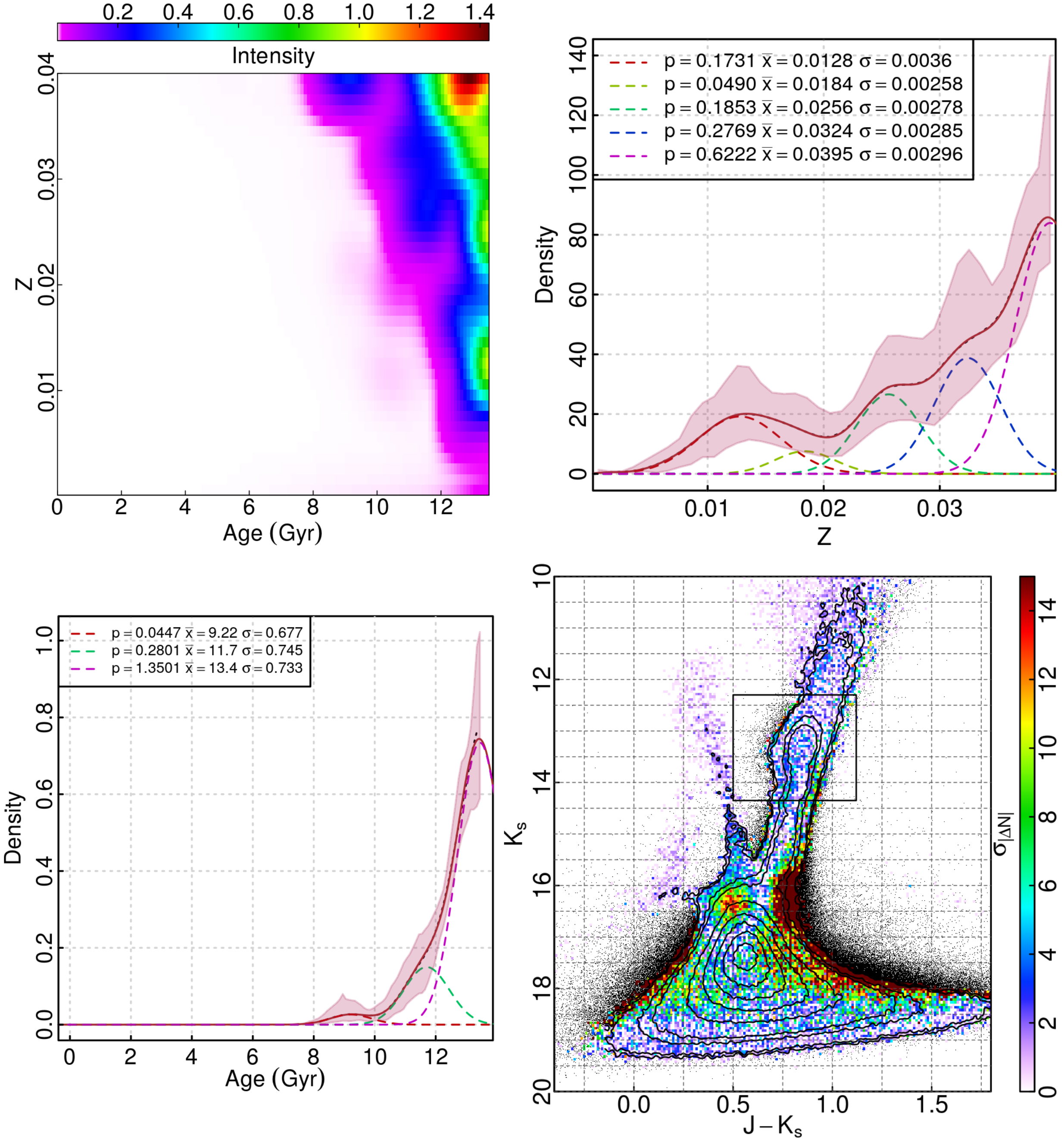

Figure 4.12: Same as in Figure 4.8, but for b259.

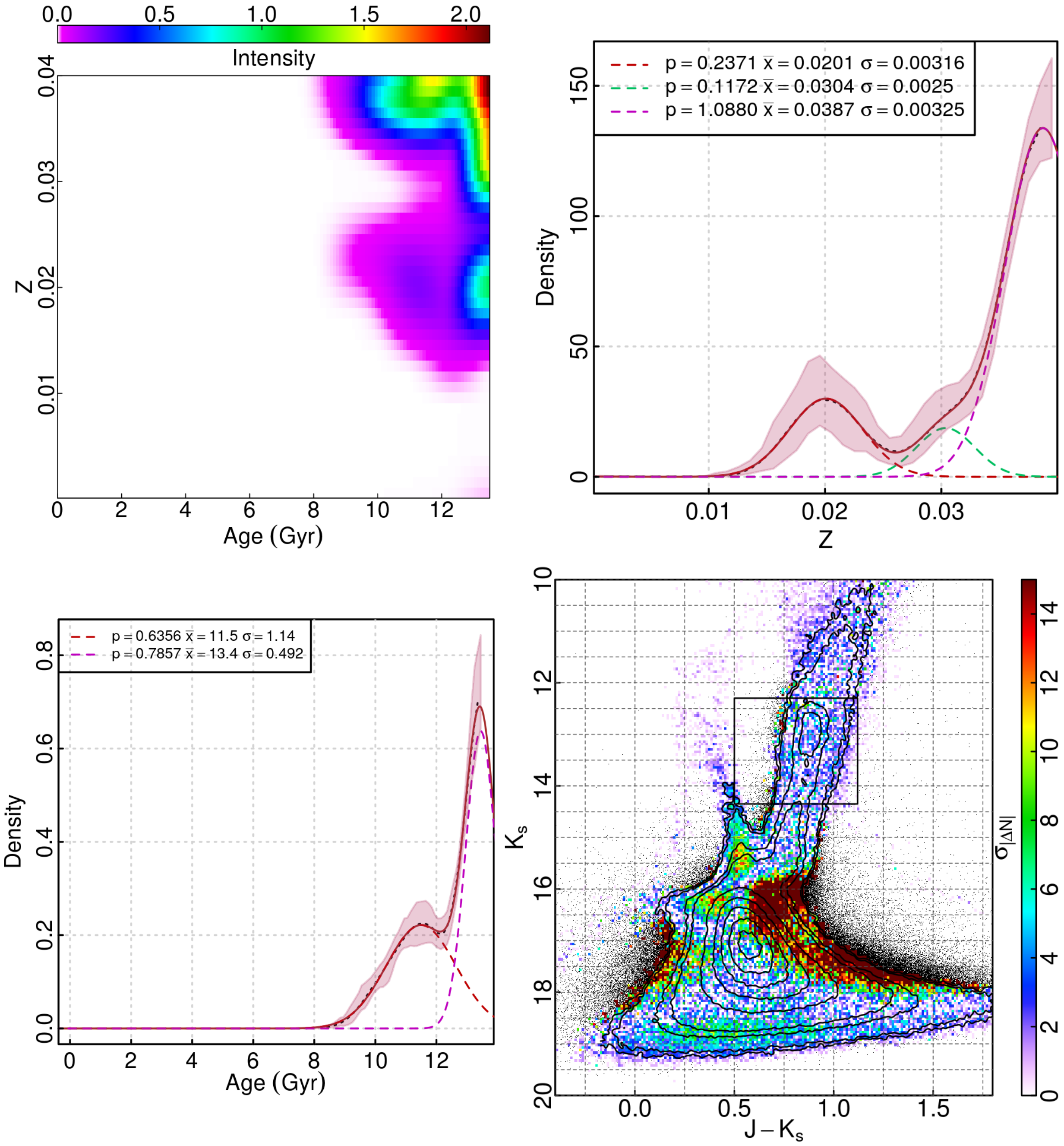

Figure 4.13: Same as in Figure 4.8, but for b283.

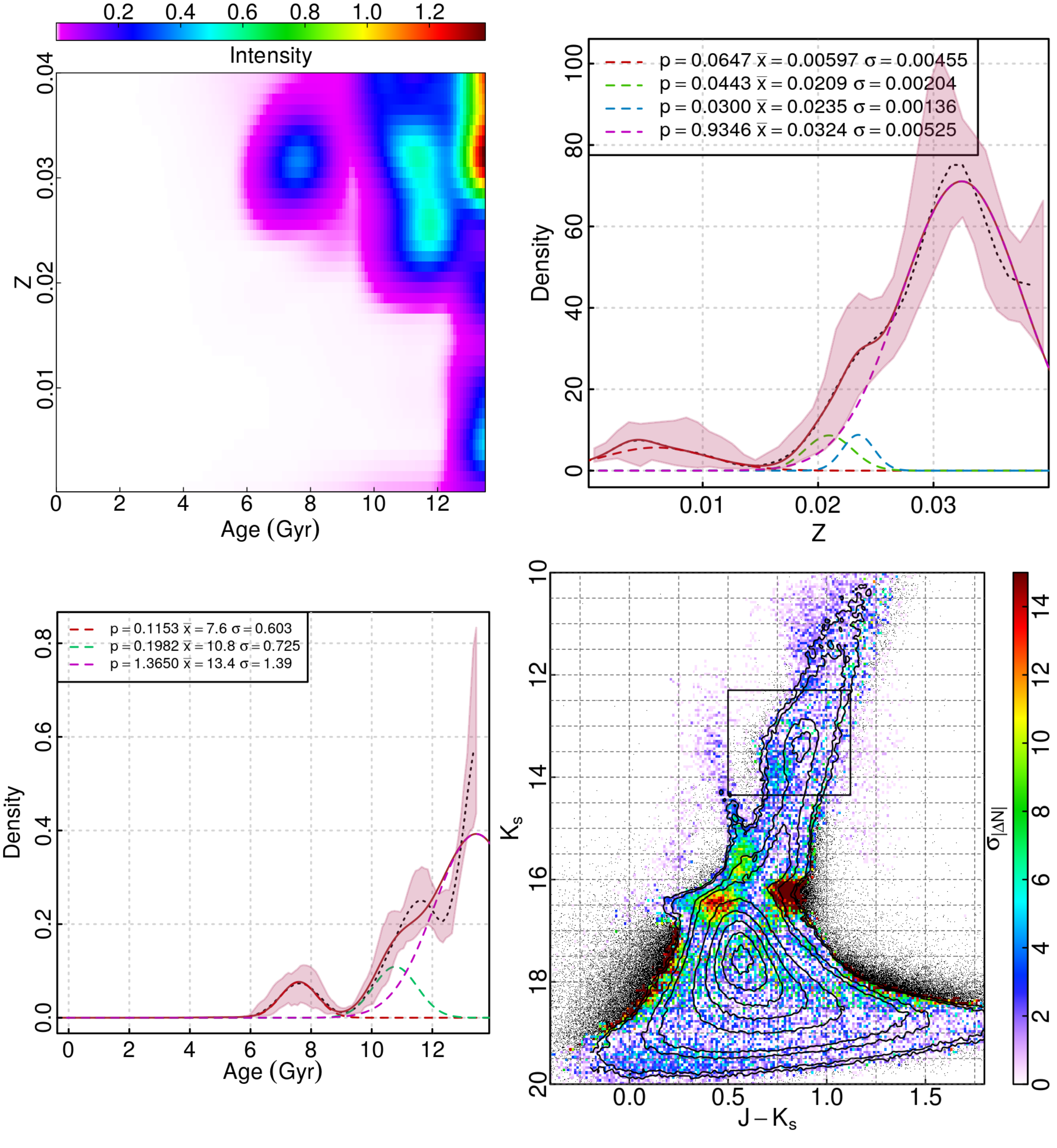

Figure 4.14: Same as in Figure 4.8, but for b384.

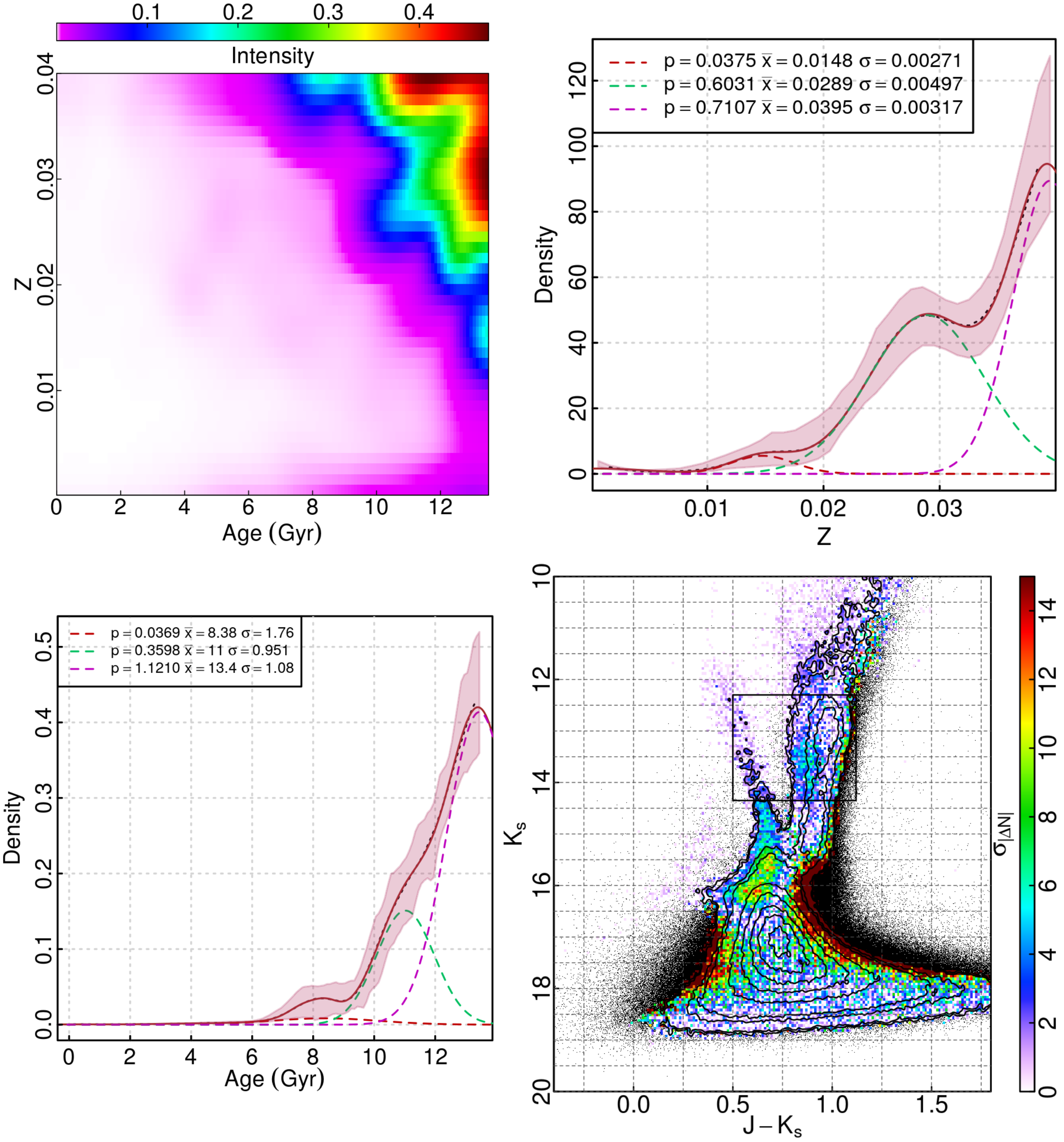

Figure 4.15: Same as in Figure 4.8, but for b396.

Table 4.3: Summary of the SFH reconstruction ages for 7 fields with acceptable residuals (see text). The presented ages and error come from the mean and square root of the variance for each marginalized age distribution.

Name	(l, b)	$< Age >^a$ (Gyr)
b249	$(-0.45°, -6.38°)$	11.23 ± 1.79
b256	$(+9.80°, -6.39°)$	10.94 ± 1.80
b259	$(-6.29°, -5.30°)$	12.37 ± 1.03
b283	$(+8.28°, -4.20°)$	12.06 ± 1.15
b293	$(+2.43°, -3.12°)$	6.14 ± 1.93
b384	$(-7.76°, +4.49°)$	11.51 ± 1.78
b396	$(+9.74°, +4.49°)$	11.65 ± 1.59

[a] As integrated from their marginalized age distribution.

many surveys (including GIBS).

With the exception of b256 and b293 fields, the results suggest that whatever young component there is, it is more metal-rich than the older one. Finally, considering some of the rather poor fits evidenced by the residual maps in Figures 4.8 to 4.15 we think that the ignorance model as applied by the IAC-STAR and IAC-POP/Minniac suites, is not adequate for the age determinations in the VVV fields, most likely, because it needs a deeper coverage of the oldest MS-TO and more accurate photometry at that level. The method using the GIBS MDF prior, although less sophisticated, has proven to be more reliable.

4.5 An age map for the MW Bulge

The results obtained with the GIBS MDF prior have been used to construct the first mean age map of the whole bulge.

As done in Valenti et al. (2016), we have assumed a 4-fold symmetry with respect to the Galactic plane and the bulge minor axis in order to quadruple the total number of datapoints (i.e. fields) by reflecting their l and b coordinates around the Galactic center. If the reasonable assumption of a rather symmetric distribution, where the age distribution of the bulge in one (l,b) quadrant is only a reflection of any of the two contiguous ones is true, then forcing this 4-fold symmetry on the datapoints has the effect of increasing the fidelity of the reproduced map, by means of an higher signal to noise (when reflections are close enough to each other) and by improving the sampling in (l,b). Additionally, such a symmetry assumption allows for a straightforward interpolation for the age map reconstruction. We have then used the same mapping method described in §2.7 (i.e. stacking Voronoi tesselations defined by random draws) to interpolate the age values between the gaps left by the data, and smoothing the interpolated values by a simple mean around a

2 degree radius. The result of this procedure is shown in Figure 4.16.

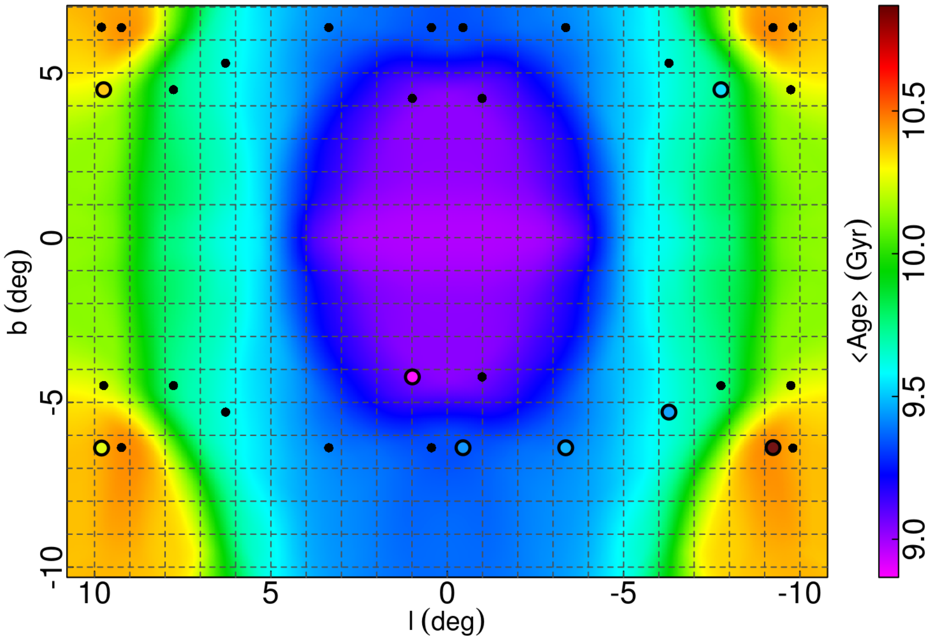

Figure 4.16: Mean age map of the MW bulge as derived by using the GIBS MDF prior. The big circles mark the position of the selected 8 fields for which we have a direct determination of the stellar ages through the GIBS MDF prior method. The small black dots refer instead to the reflection of the observed fields with respect to the *l* and *b* axis resulting from the imposed 4-fold symmetry. Note that the color of the filled points may differ from the background map, because the latter is produced from an average of the closest few of the former, rather than a point-by-point interpolation.

When building the map we have decided to use only the outer fields (i.e. $|b| \gtrsim 3°$), for which we do have robust age estimates as demonstrated by the lack of significant mismatch between the observed and simulated CMDs (see residuals map presented in Figure §4.6).

Although the innermost regions are poorly constrained by the data, the map in Figure 4.16 suggests the presence of a very mild age gradient of about 0.16 Gyr/deg towards the Galactic center, with the outer fields being slightly older (~ 1-1.5 Gyr) than those closer to the center.

If we consider the results from the SFH reconstruction in §4.4.3 that are displayed Table 4.3, we can appreciate that this method suggests a very old bulge ($\gtrsim$ 11 Gyr), with the exception of b293, which lies right at the margin of the exclusion zone of $|b| < 3°$ we have defined as the limit for the age determination to produce reliable results. These resulting ages (minus from b293) are in general older than the results from the GIBS prior set, by 1-2 Gyr, and when put in similar map than Figure 4.16, they show no true age gradient with (l,b). However, it is also true that the poor sampling provides poor constraining of a spatial gradient in this case, together with several artifacts in the map, and that by construction the GIBS prior set cannot be older than $\sim 11\,\mathrm{Gyr}$. Another characteristic of the SFH reconstructions, as mentioned already in §4.4.3, is the seemingly inconsistent derived MDF; we should expect that some of the age variation obtained is tied to these metallicity differences across the fields, due to the age-metallicity degeneracy present when using CMDs to define these quantities in a stellar population.

We would need more fields to properly compare both the GIBS prior and SFH reconstruction sets in terms of spatial age distribution, but we can conclude that in conjunction, these results do point towards an old ($\gtrsim 9.5\,\mathrm{Gyr}$) bulge population, with little to no need for anything younger than $\sim 7\,\mathrm{Gyr}$ to explain the observations. This at least in the outer area $|b| > 3°$.

Regarding the inner $|b| < 3°$ region, Figure 4.16 hints towards a slightly younger bulge around the Galactic center than in the outer area. Here we do have some overlap with the data from Bensby et al. (2017), even if just partway, and if we were to agree with their findings, then we should expect a *rejuvenated* bulge near the Galactic center. But again, their age estimates are much too extreme to be compatible with the ones presented in this work, even considering b293 ($l \sim 2°, b \sim -3°$) in the GIBS prior.

4.5.1 Misshapen stars in crowded fields

For the innermost fields it was generally impossible to find satisfactory solutions (i.e. good residual maps) that did not require some young ($< 7\,\mathrm{Gyr}$) component, be it in SFH or GIBS prior methods. Being this finding rather controversial, for these fields we decided to inspect every step of the procedures, from the photometry, to the decontamination, to the dispersion of the synthetic populations.

Nothing unusual was found for the dispersion of the observational effects, but it was rather clear that the CMD of the disk control-field used for the decontamination was not properly overlapping with that of the original bulge field. Even the point at which the disk blue plume diverges from the rest of the CMD was too bright in the central bulge fields with respect to the control-fields. This led to a previously ignored factor, which is the stellar quality of the entries in the catalogs.

In §2.4 we briefly explained how some photometric criteria are used to improve the quality of the resulting CMDs before performing the decontamination procedure. However, for these problematic cases, the quality filters used are simply not enough. This is evident from the J vs. $s(\chi^2 - 1)$ distribution, where there is a significant contribution of a non--standard category, such as heavily blended or elongated entries. In these cases the first filter (σ_s clipping) eventually removes a considerable number of normal star-like entries near the RC and red-faint corner of the CMD before efficiently removing the unlikely stars around $\mathrm{K_s} \sim 16$. The second filter (3D histogram) would require very aggressive cleaning of the $> 6\%$ quantiles, to have a significant effect, point at which the relative distribution of *bona fide* removed stars in the CMD is no longer uniform.

For such extreme cases (i.e. innermost fields), we tried to define an *aperture* Φ, which would be simply a fit of one (or more) gaussians to the $s(\chi^2 - 1)$ distribution for stars with $14 > \mathrm{J} > 12$, where we have noted that there are mostly well-behaved stars (i.e. with a symmetrical $s(\chi^2-1)$ distribution around 0, meaning roundish and rather well fitted). We then use this aperture to assign weights to all the stars in the catalog $\omega_i = \Phi(s_i(\chi_i^2-1))$, based on their quality index, and then build a clean catalog by interpreting this weight as the probability for the particular entry to form part of the new cleaned catalog.

In practice, this ends up removing an important fraction of the original catalog, but most stars within very nominal parameters survive, making it a *clean* sample. However, due to the selective removal, that is generally stronger near $\mathrm{K_s} \sim 16$ (and barely reaches the faintest region of the CMD), this aggressive filter would also likely affect the shape of the CMD, which goes against the definition of a simple cleaning we give in §2.4.

Nevertheless, we have applied this filter, with a simple gaussian aperture of

$$\Phi(s(\chi^2-1), \mu=0, \sigma=0.2) \tag{4.4}$$

where μ and σ are the true mean and standard deviation of the normal distribution, respectively. The results are displayed in Figure 4.17 for b293 and Figure 4.18 for b306.

In the case of b293 and b306 fields, when we clean the original raw catalogs by using this new filter, reapply the decontamination procedure and re-run the GIBS MDF prior fitting, we obtain substantially different results. Specifically, there is no longer any need for stars younger than 10 Gyr in the MR component (although we do account for BSS in the regular fashion). However the residual show an unacceptable discrepancy at the RC level and a new one near the blue edge of the CMD at $\mathrm{K_s} \sim 17$ (see bottom left panel in Figure 4.17 and Figure 4.18). Concerning the RC discrepancy, we know that it does not impact the age determination, except for the MP requirement of an old population (see §4.1). The discrepancy showing on the blue edge of the CMD resembles similar cases in peripheral fields (see Figure 4.6, panels b243, b278 and b396, among other milder non-related cases).

These *unlikely* stars revealed once the aperture filter is used could be the result of unaccounted blendings, or caused by a bad sky subtraction. The latter is often present where the crowding is extreme and the background sky monitoring is obtained through too few jittered images on-target, rather then from off-target positions to relatively sparse fields.

Without more precise knowledge of the nature of these unlikely stars, or even a model (or an aperture for them), they cannot be unambiguously removed from the raw catalogs, nor be included into the considerations for the synthetic population simulation (if they are not already being accounted for in the observational effects estimation). Thus, we close this discussion here, giving an alternative explanation for the relatively young bulge we have derived from §4.5, but without completely discarding the age gradient suggested by Figure 4.16 (i.e. younger mean population closer to the center).

4.5.2 Comparison with N-body simulations and conclusions

The age map we present here is the first of its kind for the bulge and as such it is interesting to compare it with the corresponding predictions of N-body simulations and models. For this purpose, we have been kindly provided a simulation set from Debattista et al. (2017).

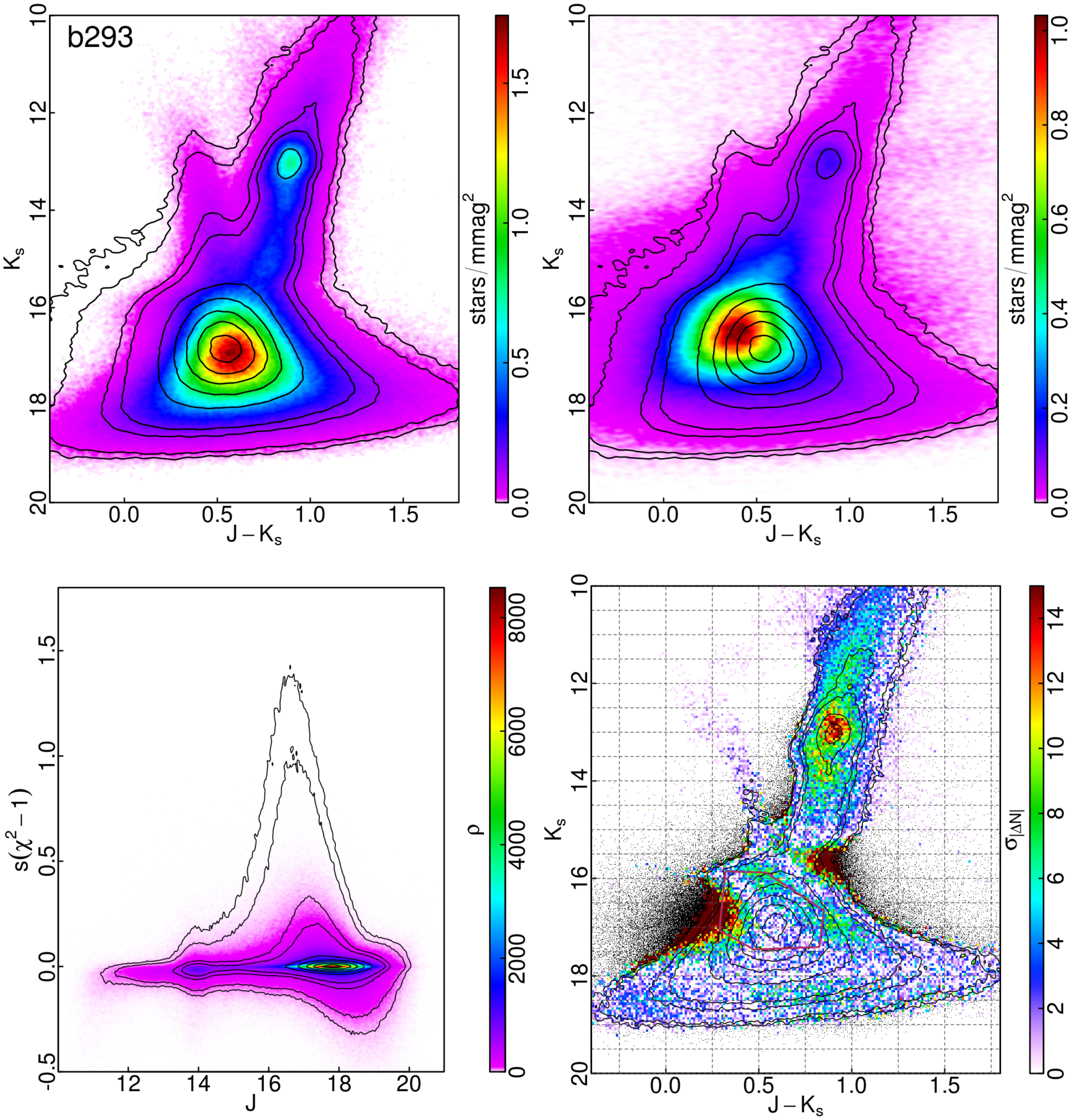

Figure 4.17: Aperture cleaning applied to b293. *Top-left*: Hess diagram of the cleaned CMD and contour of the raw catalog. *Top-right*: Complement of top-left panel, showing the removed stars from the original raw catalog ($\sim$50% of the original). *Bottom-left*: $s(\chi^2-1)$ distribution for this field, color background is after cleaning, contour is before. *Bottom-right*: Residual $\sigma_{|\Delta N|}$ map for the cleaned field, using purely old populations ($>10\,\mathrm{Gyr}$).

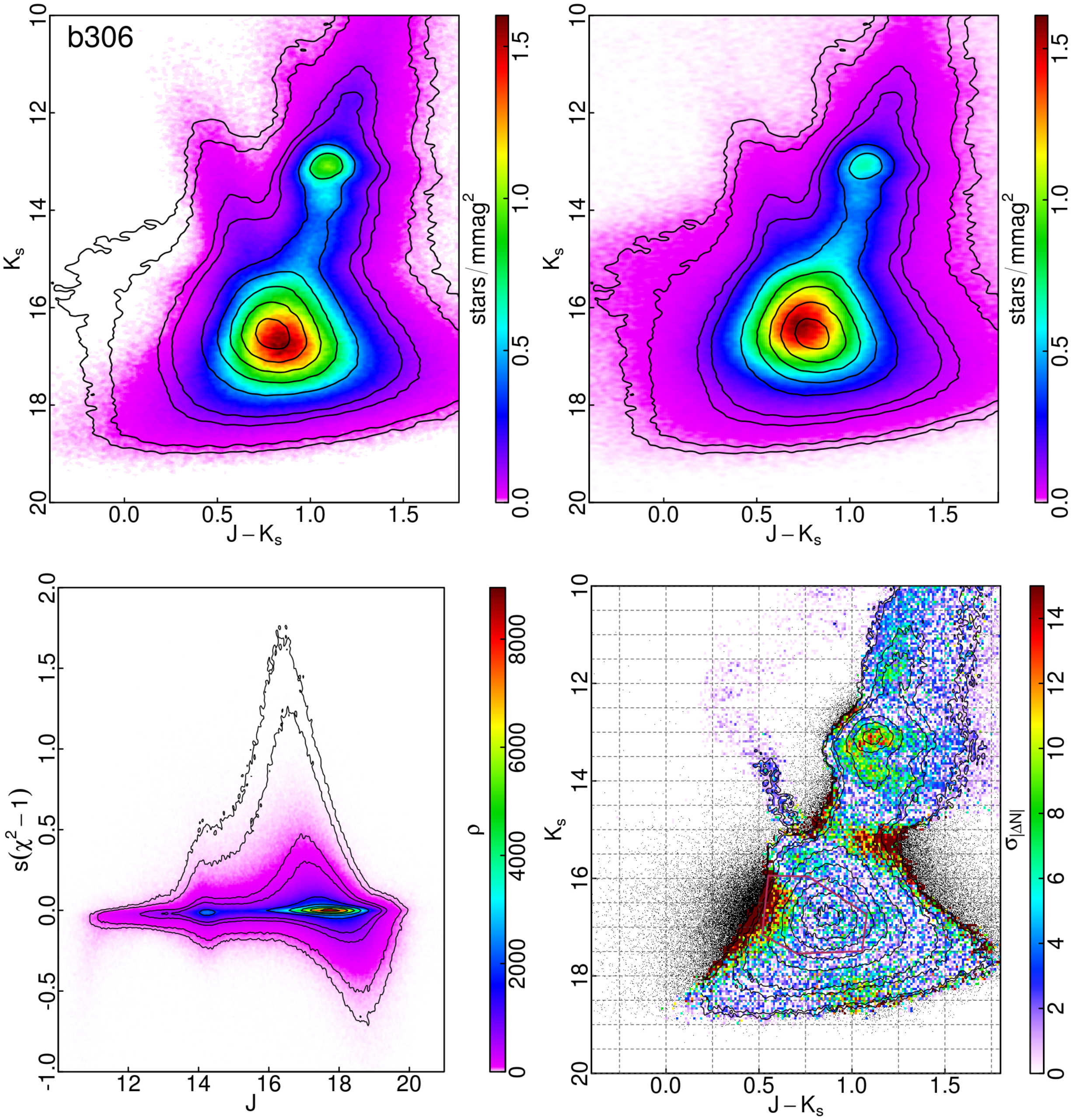

Figure 4.18: Aperture cleaning applied to b306. *Top-left*: Hess diagram of the cleaned CMD and contour of the raw catalog. *Top-right*: Complement of top-left panel, showing the removed stars from the original raw catalog (∼45% of the original). *Bottom-left*: $s(\chi^2-1)$ distribution for this field, color background is after cleaning, contour is before. *Bottom-right*: Residual $\sigma_{|\Delta N|}$ map for the cleaned field, using purely old populations ($>10\,$Gyr).

We first scale the XYZ dimensions of the simulation to match the appearance of the star density in our observations, as well as the bar feature in the simulation being contained within the central 4 kpc of the Galaxy. A scale factor of 1.3 seems to be enough to roughly satisfy these conditions. Also needed, in this particular simulation, is the scale up of the age of the stars. To roughly match the oldest results in the observed map, we have added 1.5 Gyr to the ages of all the stars in the N-body simulation. Finally, to obtain only a bulge map we have limited the sample in the simulation to be at most 4 kpc from the center.

The result of the projection, and of averaging the stellar ages to produce a map is shown in the upper panel of Figure 4.19. For an easy comparison between the N-body simulations and the observations, in the same figure we also show the map derived in this work (see bottom panel), both with the original colored circles marking the datapoints in the restricted ($|b| > 3°$) GIBS prior set. In the peripheral fields, observations and simulations show similar overall trend, with about uniformly old stars (> 10 Gyr) for $|b| > 3°$. Both maps do agree in a gradient towards younger ages in the center, although the central most areas in the N-body simulations predict a much younger mean age than we have even been able to find in the observations, even considering the central-most field results ($|b| < 3°$) in the GIBS prior set. However, due to the caveats discussed in §4.5.1, it is likely that the gradient present in the observations, with a rather steep decrease to younger stars towards the center and plane of the galaxy when considering all the results, is mostly driven by defects in the data, rather than to true age variation. Thus, we cannot ascertain that the young feature visible in the observation maps reflects the predicted young gradient in the simulations.

With the above considerations, it seems to be an agreement in the areas where we have data (see big colored circles in the maps), or at least when the mean ages are regarded. If we go to the details, however, we are missing the slight mean age increase that is seen in the simulations surrounding the Galactic center, seen a the central ~ 5 deg slightly darker *halo* around the Galactic center in the top panel of Figure 4.19, and in fact, from the datapoint we have at $b \sim 5°$, we find stars becoming younger than in the outer fields. Of course the scales are not comparable, and given one map is a perfect representation of a model and the other is an estimate from observations, we are bound to find disagreements. That said, if we were to simply construct an age map from the N-body simulation data, but restricted to the same field position and size that we have in the observations, then this map would be very similar in shape but the overall age gradient we would obtain would be reversed in sign (younger in the outer bulge, older in the center). However, not only we lack resolution (fields are too widely distributed) and robustness (only 8 effective datapoints) to make a comparison to assess the detailed differences between the two sets, but also we have no data in the critical $|b| < 2°$ area, where the N-body simulation shows a deviation from a uniformly old ($\gtrsim 10$ Gyr) bulge.

Another useful diagnostic is the comparison between the age dispersion values ($\sigma_{\rm Age}$). In Figure 4.20 we show, side by side, the $\sigma_{\rm Age}$ map for both the N-body simulation and the map from GIBS prior.

Overall, GIBS prior and the simulation from Debattista et al. (2017) seem to agree also on the age dispersion level, with differences of about 0.5 Gyr in $\sigma_{\rm Age}$ which are quite small

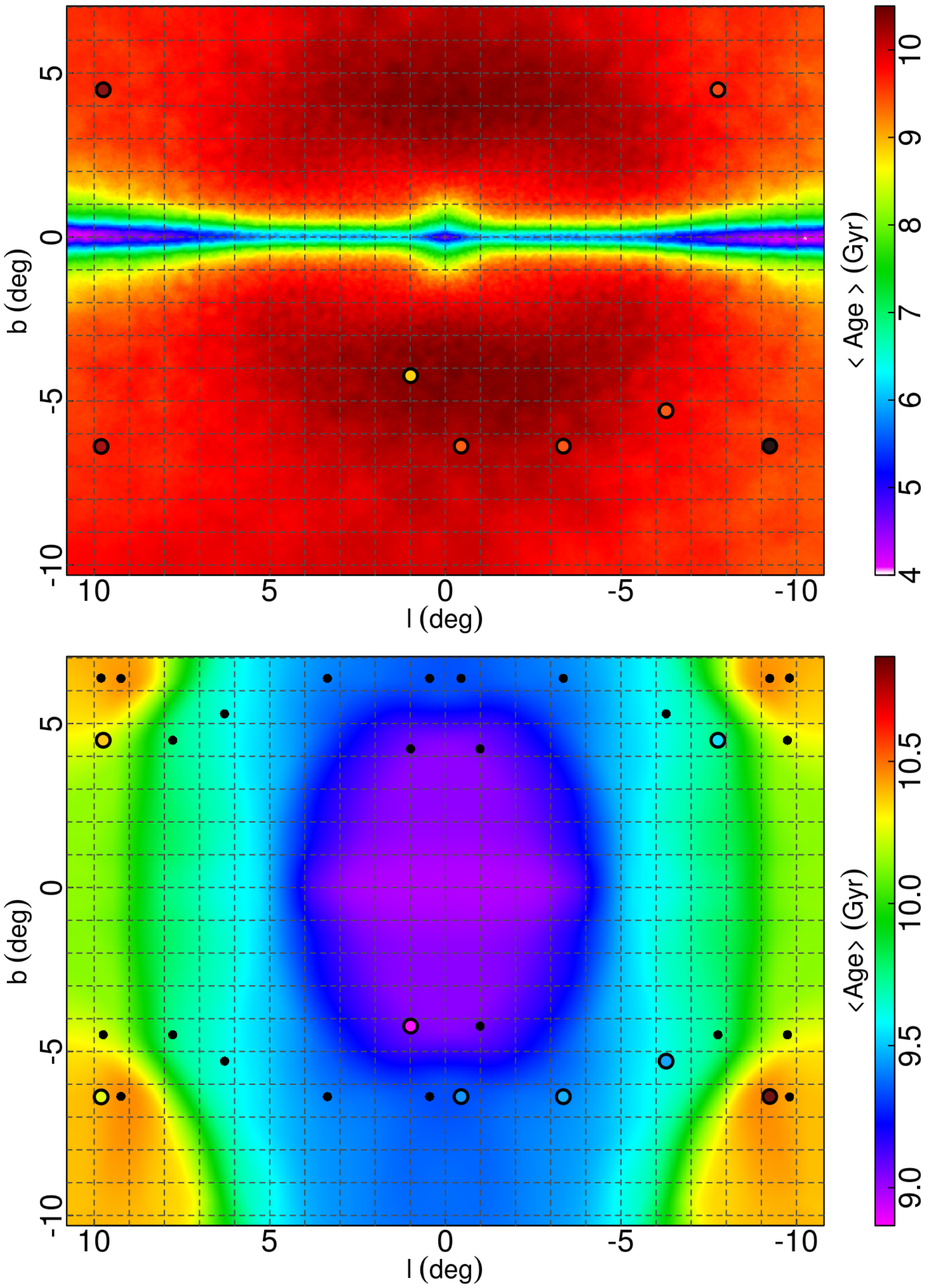

Figure 4.19: Mean stellar age map as produced by the N-body simulations from Debattista et al. (2017) (top panel), and from this work (bottom panel). As in Figure 4.16, we have included the color-coded filled circles of the fields actually used to make the observation-based map, where the colors are in the same scale as the background map. Additionally, for the bottom panel, the black dots show the position of the extra data points produced by the 4-fold symmetry we have imposed.

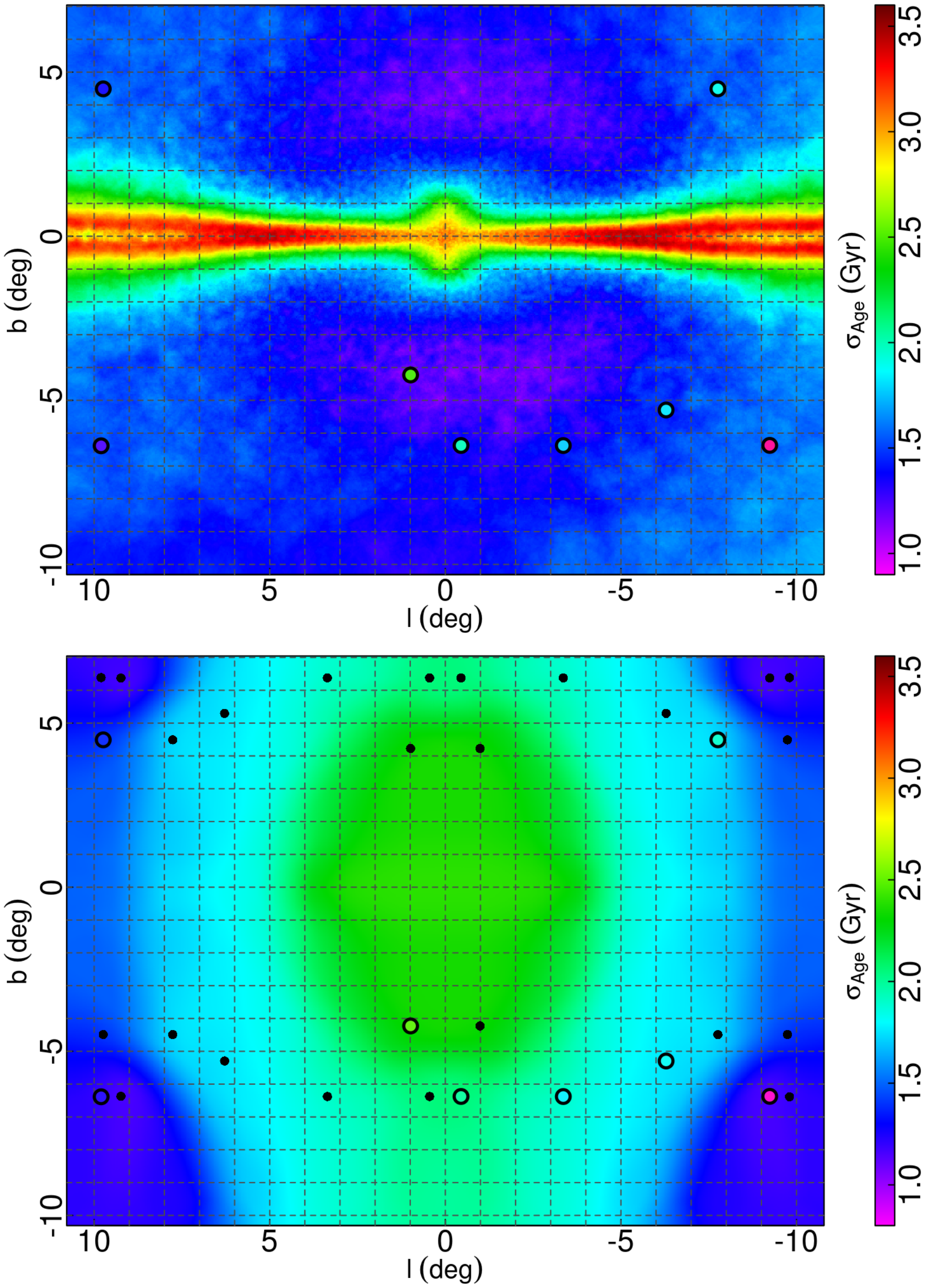

Figure 4.20: Age dispersion maps for N-body simulations (top panel) and the GIBS prior results (bottom). Both maps are in the same scale in $\sigma_{\rm age}$. In similar fashion as in Figure 4.16, we use color-coded filled points to denote the fields from which we have data, and black circles to mark the datapoints reflections from the imposed 4-fold symmetry.

considering the rough approach we have taken for the GIBS prior sample (i.e. steps in age of 1 to 2 Gyr, mandatory widths of 0.6 Gyr in age distribution). However, without access to the central 2 degrees, we still cannot discard discrepancy between the two, or be able to favor either formation scenario outlined in §1.

Despite the limitations hereby described, the final conclusion is that considering the ages we have found for the nominal fields in Table 4.1, the bulge is *consistently old* ($\gtrsim$ 9.5 Gyr) at all longitudes explored and at least for $|b| > 3°$, with a rather small gradient towards the central longitudes. This, of course, excluding any small-scale variation that is not probed by the wide grid used here, nor anything that may break the imposed 4-fold symmetry. If we exclude the $|b| < 3°$ strip, which contains fields with doubtful quality data, then the interpolated map suggest an old bulge ($\gtrsim$ 9 Gyr) throughout the whole extension of the probed fields. In the case of the GIBS prior results, which are more reliable of those obtained from the SFH reconstruction, a centrally concentrated population of ∼9 Gyr is also hinted, with an appropriate central gradient of ∼0.16 Gyr/deg, and between 9 and 10.5 Gyr.

Our results are still at odds with those obtained from the microlensed dwarfs by Bensby et al. (2017). Despite the fact that the probed area by their study overlaps considerably with the area in which we either start seeing younger populations or where our data start failing (which would mean that we simply are not seeing the same stars that they do), the age ranges we have found is sufficiently different to produce disagreement.

In order to finally provide a direct and complete comparison between both the spectroscopic age estimates and the N-body simulations from Debattista et al. (2017), we would need to reach the innermost regions, closer to the Galactic plane with sufficient accuracy. This would mean, not only deeper photometry to sample the MS-TO area with sufficient completeness and smaller errors, but also much more accurate dataset, to resolve the stars in the most crowded fields effectively. Once a sufficiently high level of accuracy is reached, an equally accurate (and complex) model would need to be tailored for this observations and purposes.

Chapter 5

Summary and future perspective

In this study I have derived a new JK_s photometric compilation of about 600 million stars in the Galactic bulge area by applying accurate PSF-fitting model on VVV images. These catalogs not only contain magnitudes and positions, but also diagnostic values (i.e. sharpness and χ^2) for photometric quality cleaning, as well as completeness values that are invaluable for star counting and statistics in the bulge region. Additionally, with the completeness experiments comes an estimate of the systematic uncertainties of the whole dataset. The entire compilation of 196 photometric catalogs covering about $300\,\mathrm{deg}^2$ across the bulge will be made public.

These new catalogs allowed me to derive a new extinction map with unprecedented high spatial resolution, which will be particularly important for the future spectroscopic surveys (i.e. MOONS) aiming at exploring the innermost bulge fields close to the Galactic plane. Indeed, this map provides high sensitivity especially towards the Galactic center and equatorial plane, and it outperforms all currently available extinction maps in the area. The method used to derive the map is also viable in the disk, as I have tested in the control fields, but also in the VVV disk area adjacent to the bulge VVV dataset.

The determination of the stellar ages in selected fields across the bulge have been provided through the comparison between observed and synthetic color-magnitude diagrams (CMD). Specifically, the observed bulge sample has been first decontaminated from the contribution of the intervening foreground disk population by using a statistical approach, and then compared to synthetic populations tailored to the observational biases, such as distance dispersion, differential reddening and completeness. The comparison between observations and models is approached in two different ways. One method assumes the metallicity distribution function (MDF) spectroscopically inferred by the GIBS survey (i.e. the population age is the only free parameter), while the other approach involves the reconstruction of the star formation history (SFH) in each field, but assuming no particular prior neither for the metallicity nor for the age (i.e. uniform distributions for both).

The ages derived by either approach are more or less consistent, although with a systematic difference of about 1-2 Gyr. Both methods find the bulk of the population to be consistently old ($\gtrsim$9.5 Gyr) in the outer bulge regions ($|b| \gtrsim 4°$, $|l| > 4°$), advocating for the presence of a mild gradient that implies younger stars (i.e. in average ∼9 Gyr) towards the center of the Galaxy, albeit with different slopes.

In the case of the SFH reconstruction, the gradient is not so certain because the photometric uncertainties of central field ($|b| < 3°$) that drives the SFH result prevents reliable and robust age estimates. Indeed, for the SFH reconstruction to be accurate, the photometry has to be deep enough to sample the oldest main sequence turn-off (MS-TO) with nominal completeness ($\gtrsim$ 30-50%), otherwise the fitting procedure will likely prefer younger solutions.

On the other hand, when excluding the inner region ($|b| < 3°$), the GIBS prior method finds a relatively smooth gradient of 0.16 Gyr/deg towards the Galactic center .

When attempting the determination of the stellar ages in few fields located in the inner bulge region, $|b| < 3°$, we noted that as the crowding becomes more severe there seems to be an increase in low-quality stars in the corresponding photometric catalogs. That is, badly fit by the field point spread function (PSF). The position in the CMD of these stars can mimic the signal of young stellar population components in the residual maps. These caveats affecting the photometry of innermost fields prevent us to firmly constrain the age of the stellar population in the innermost regions, where we do not have enough evidence to either completely discard a young component near the center ($\lesssim$5 Gyr), or to accurately constrain its relative contribution to the bulge population.

Nevertheless, we show that in the bulge region at $|b| > 3°$, the disk-decontaminated CMDs are best-fitted by using a synthetic populations mix containing mostly old ($\gtrsim$10 Gyr) stars, a proxy for blue straggler stars (BSS), and some fractions of stars not younger than ∼7 Gyr. The latter being necessary only to reproduce the CMD of fields at $-3° < b \lesssim -6°$)

I have used the most robust results (i.e from fields with $|b| \gtrsim 3°$) to build the first map of the mean age, and age dispersion of the bulge stellar population.

When comparing these maps with those obtained by using the N-body simulations from Debattista et al. (2017) I find an overall good agreement. However, to firmly testing the predictions of this model it is crucial to provide observational constrains in the innermost region, $|b| < 3°$, where unfortunately the data at our disposal proved to be not sufficiently good.

The results obtained in this work are in good agreement with the most recent photometric determinations based on HST data (Renzini et al., 2018), but still largely inconsistent with the findings from the microlesend dwarfs project of Bensby et al. (2017).

As final closing remarks, this thesis represents the first systematic and homogeneous study of the stellar population age across the Galactic bulge yielding the first age and age dispersion map. The bulge stellar population is found to be old ($>$ 9.5 Gyr) as several other photometric studies before, although none as extensive in terms of sampled area and number of detected stars as this work.

5.1 Future perpective

This study can be extended to as many fields as possible within the $|b| < 6°$ strip, with the mentioned caveats on the inner area ($|b| \lesssim 3°$). If the reddening issue is properly addressed/understood it is plausible to add fields with higher differential reddening in order to obtain more accurate ages for the central plane and center area. The larger the number of sampled fields is, the more constrained the resulting map becomes. Additionally, by appropriately sampling the bulge area (i.e. selecting more fields well distributed and including age determination in the central strip), the map could achieve sufficient resolution and robustness to adequately constrain the N-body simulations and models.

The ongoing VVV extension, the VVVX (Minniti, 2016), is providing the additional data to increase the depth and quality of the already presented fields/tiles by providing more epochs, but also opening the possibility to explore the region at $b > 5°$ that was not covered by VVV.

The internal work, code, and algorithms of this thesis (e.g. decontamination, extinction map construction algorithm, simulation dispersion, etc), which are part of the legacy value of this project, can be easily applied to different dataset, such for instance VVVX's. An immediate benefit of an increase in the number of epochs, is the extended depth of the photometry allowing to improve the MS-TO sampling in the marginal fields (e.g. b293, $b \sim -3°$), as well as possibly extending the effective area in which we can implement the SFH reconstruction algorithm and recover meaningful results.

On the other hand, in the new region provided by VVVX (i.e. outermost bulge region) one could start using Gaia proper motions to kinematically separate the bulge from the disk. This has not been possible for the present study because, due to the severe crowding and extinction, Gaia-DR2 provides very poor sampling of the old MS-TO already at high latitude (i.e. $b \sim -7.5°$).

Finally, with the extension of the data, also comes the possibility to develop an extinction map for these regions too. And not only in the bulge, but also into the disk area.

Appendix A

Emulation of observational effects

In this appendix I will explain the method by which we emulate or *disperse* synthetic populations from the ideal $(\mathrm{J}^{in}, \mathrm{K_s}^{in})$ plane into the *observed* $(\mathrm{J}^{obs}, \mathrm{K_s}^{obs})$.

What we intend to do, is to take any given model synthetic population, and emulate the observational effects we see in the observed data. That is, we seek to imprint the photometric + systematic errors and uncertainties in the photometry extraction procedure into a theoretical CMD. This is equivalent to convolving it with a kernel that depends on J and $\mathrm{K_s}$, which we unfortunately do not know nor cannot define conveniently nor consistently in a closed analytical form.

For the following part, we would like to explain that in the the following descriptions and objects, when we use *injected* or *recovered* we make direct reference to the results of the completeness experiments described in §2.3 and §4.1.1, but in particular to the results and criteria pertaining the latter. The end product of these experiments is a catalog that matches injected magnitude pairs $\mathbf{m^{in}} = (\mathrm{J}^{in}, \mathrm{K_s}^{in})$ to recovered $\mathbf{m^{rec}} = (\mathrm{J}^{rec}, \mathrm{K_s}^{rec})$. Following, we define a brief glossary with connections to what is mentioned in the main work:

$\mathbf{m^{in}}$: one pair of $(\mathrm{J}^{in}, \mathrm{K_s}^{in})$, the injected magnitudes from the completeness experiments.

$\mathbf{m^{rec}}$: one pair of $(\mathrm{J}^{rec}, \mathrm{K_s}^{rec})$, coupled to one particular $\mathbf{m^{in}}$.

$\{\mathbf{m^{in}}_i\}_{i=1}^{N}$: denotes a set of $\mathbf{m^{in}}_i$ where $i \in \{1, 2, 3, ..., N\}$

$\{\mathbf{m^{rec}}_i\}_{i=1}^{N}$: denotes a set of $\mathbf{m^{rec}}_i$ where $i \in \{1, 2, 3, ..., N\}$

S : a particular subset of indices i, so that $S \subseteq \{1, 2, 3, ..., N\}$ and $\{\mathbf{m^{in}}_i\}_S \subseteq \{\mathbf{m^{in}}_i\}_{i=1}^{N}$.

We understand that there must exists a function $\mathbf{F}_\Psi(\mathrm{J}, \mathrm{K_s}) = \mathbf{F}_\Psi$, that takes as input a given pair $\mathbf{m^{in}}$ and outputs a $\mathbf{m^{rec}}$ as a random realization of some unknown distribution Ψ, which may also have non-trivial dependence with J and $\mathrm{K_s}$:

$$\mathbf{F}_\Psi : \ \mathbf{m^{in}} \rightarrow \mathbf{m^{rec}} \tag{A.1}$$

In terms of our objective, the theoretical CMD would provide a discrete set of vectors $\{\mathbf{m^{in}}_i\}_M$, for which we want the corresponding image set $\{\mathbf{m^{rec}}_i\}_M$ so that $\mathbf{F}_\Psi :\ \mathbf{m^{in}}_i \rightarrow \mathbf{m^{rec}}_i\ \forall i \in M$. Now, we do not know $\mathbf{F}_\Psi$, but thanks to the completeness experiments, we have the coupled sets of $\{\mathbf{m^{in}}_i\}_{i=1}^N$ and $\{\mathbf{m^{rec}}_i\}_{i=1}^N$ that stem from $\mathbf{F}_\Psi$. This means that we have in principle the means to construct an empirical estimator of $\mathbf{F}_\Psi$.

Now, $\mathbf{F}_\Psi$ is not a deterministic function; the image of a given $\mathbf{m^{in}}$ is a random realization of the distribution function (or kernel) Ψ. In that sense, given infinite trials with a particular $\mathbf{m^{in}}$ we should be able to reconstruct the underlying image distribution Ψ and use it to yield a sample set $\{\mathbf{m^{rec}}_i\}_U$. And since we cannot define $\mathbf{F}_\Psi$ without infinite trials (or a statistical model that works), using an empirical estimator $\widetilde{\mathbf{F}}_\Psi$ should suffice, so that:

$$\widetilde{\mathbf{F}}_\Psi :\ \{\mathbf{m^{in}}_i\}_S \rightarrow \{\mathbf{m^{rec}}_i\}_S \tag{A.2}$$

Where now S is an index set, that defines a subset of the coupled vector sets, $\{\mathbf{m^{in}}_i\}_{i=1}^N$ and $\{\mathbf{m^{in}}_i\}_{i=1}^N$. That is, $\forall i \in S,\ \mathbf{F}_\Psi :\ \mathbf{m^{in}}_i \rightarrow \mathbf{m^{rec}}_i$.

Being $\{\mathbf{m^{in}}_i\}_{i=1}^N$ and $\{\mathbf{m^{rec}}_i\}_{i=1}^N$ as defined above, without having explicit formulation for the action of $\mathbf{F}_\Psi$, we still can empirically map $\widetilde{\mathbf{F}}_\Psi$ by choosing a sufficiently convenient index set S.

In this sense, it is enough to have a sufficiently dense $\{\mathbf{m^{in}}_i\}_{i=1}^N$ so that any choice of S means that a) $\{\mathbf{m^{in}}_i\}_S$ is as close as possible to a "point", or conversely, that the metric distances between any pair of points in the vector set are as small as possible, and b) that S is numerous enough to provide sufficient statistics on $\{\mathbf{m^{rec}}_i\}_S$ to accurately reconstruct Ψ given $\{\mathbf{m^{in}}_i\}_S$.

Since what we have is the set $\{\mathbf{m^{rec}}_i\}_S$, but we want $\{\mathbf{m^{rec}}_i\}_U$ that may be much larger, it means we need to either make U as an oversampled S, so then $\{\mathbf{m^{rec}}_i\}_U$ is composed entirely of (possibly) repeated members of $\{\mathbf{m^{rec}}_i\}_S$, or we can obtain a $\{\mathbf{m^{rec}}_i\}_U$ by random draws of an empirically estimated density function $\widetilde{\Psi}$ defined by $\{\mathbf{m^{rec}}_i\}_S$, as a proxy for Ψ.

We have opted for the latter, and hereby describe how we construct $\widetilde{\Psi}$.

The set $\{\mathbf{m^{rec}}_i\}_S$ defines a convex hull region W^{rec}, so that all points in $\{\mathbf{m^{rec}}_i\}_S$ are contained within W^{rec}; take all the points in $\{\mathbf{m^{rec}}_i\}_S$ and connect lines to each possible pair, W^{rec} is then the outermost polygon. W^{rec} is convex by construction.

We arbitrarily expand W^{rec} to 101% of its dimensions (to avoid numerical approximation issues), and create a Voronoi tesselation of it using the points in $\{\mathbf{m^{rec}}_i\}_S$. We can now approach the true distribution Ψ from whence it came by defining the empirical estimator $\widetilde{\Psi}$ as a collection of uniform 2D distributions defined in the boundary of each tile of the tesselation, so that their respective integrals are the same, that is, given a random realization each tile would have the same probability of contributing. It follows that $\{\mathbf{m^{rec}}_i\}_U$ can be the random draw from $\widetilde{\Psi}$.

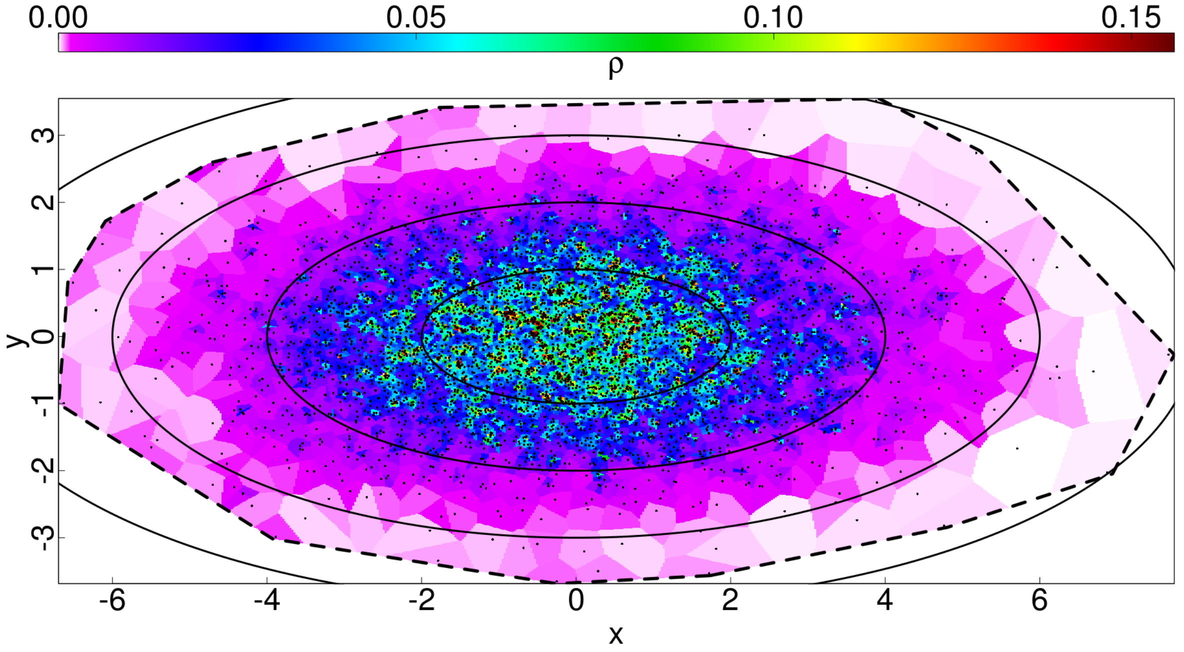

Figure A.1: $\widetilde{\Psi}$ for the concrete example where Ψ is a bivariate gaussian in XY with $\mu_X = \mu_Y = 0$ as centroid, and variances $\sigma_X^2 = 4$ and $\sigma_Y^2 = 1$, and $\{\mathbf{m^{rec}}_i\}_S$ is a set of 5,000 realizations of it. The color scale (ρ) is the density, which for each tiles is the inverse of its area. The color range has been adjusted to prevent saturation for very high localized densities, currently displaying all values above 0.157 (95% percentile) with dark red. Also plotted are the 1-4 σ contours for Ψ (solid lines) and the boundary of W^{rec} as described in text (dashed lines). The black dots mark the individual points of $\{\mathbf{m^{rec}}_i\}_S$.

In a concrete example, let Ψ be a bivariate gaussian in XY with $\mu_X = \mu_Y = 0$ as centroid, and variances $\sigma_X^2 = 4$ and $\sigma_Y^2 = 1$. Let $\{\mathbf{m^{rec}}_i\}_S$ be a set of 5,000 random realizations of Ψ. Then $\widetilde{\Psi}$ would look like in the Figure A.1.

Bibliography

J. Alonso-García, R.K. Saito, M. Hempel, D. Minniti, J. Pullen, M. Catelan, R. Contreras Ramos, N.J.G. Cross, O.A. Gonzalez, P.W. Lucas, T. Palma, E. Valenti and M. Zoccali, *ArXiv e-prints* (2018), [`arXiv:1808.06139`]

A. Aparicio and C. Gallart, *AJ* **128** (2004), 1465

A. Aparicio and S.L. Hidalgo, *AJ* **138** (2009), 558

C. Babusiaux, A. Gómez, V. Hill, F. Royer, M. Zoccali, F. Arenou, R. Fux, A. Lecureur, M. Schultheis, B. Barbuy, D. Minniti and S. Ortolani, *A&A* **519** (2010), A77

E.F. Bell, *ApJ* **682** (2008), 355

T. Bensby, S. Feltzing, A. Gould, J.C. Yee, J.A. Johnson, M. Asplund, J. Meléndez, S. Lucatello, L.M. Howes, A. McWilliam, A. Udalski, M.K. Szymański, I. Soszyński, R. Poleski, Ł. Wyrzykowski, K. Ulaczyk, S. Kozłowski, P. Pietrukowicz, J. Skowron, P. Mróz, M. Pawlak, F. Abe, Y. Asakura, A. Bhattacharya, I.A. Bond, D.P. Bennett, Y. Hirao, M. Nagakane, N. Koshimoto, T. Sumi, D. Suzuki and P.J. Tristram, *ArXiv e-prints* (2017), [`arXiv:1702.02971`]

T. Bensby, S. Feltzing and M.S. Oey, *A&A* **562** (2014), A71

T. Bensby, J.C. Yee, S. Feltzing, J.A. Johnson, A. Gould, J.G. Cohen, M. Asplund, J. Meléndez, S. Lucatello, C. Han, I. Thompson, A. Gal-Yam, A. Udalski, D.P. Bennett, I.A. Bond, W. Kohei, T. Sumi, D. Suzuki, K. Suzuki, S. Takino, P. Tristram, N. Yamai and A. Yonehara, *A&A* **549** (2013), A147

T. Bensby, A.R. Zenn, M.S. Oey and S. Feltzing, *ApJ* **663** (2007), L13

E.J. Bernard, M. Schultheis, P. Di Matteo, V. Hill, M. Haywood and A. Calamida, *MNRAS* (2018), [`arXiv:1801.01426`]

A. Bhardwaj, M. Rejkuba, D. Minniti, F. Surot, E. Valenti, M. Zoccali, O.A. Gonzalez, M. Romaniello, S.M. Kanbur and H.P. Singh, *A&A* **605** (2017), A100

F. Bournaud, B.G. Elmegreen and M. Martig, *ApJ* **707** (2009), L1

A. Calamida, K.C. Sahu, S. Casertano, J. Anderson, S. Cassisi, M. Gennaro, M. Cignoni, T.M. Brown, N. Kains, H. Ferguson, M. Livio, H.E. Bond, R. Buonanno, W. Clarkson, I. Ferraro, A. Pietrinferni, M. Salaris and J. Valenti, *ApJ* **810** (2015), 8

W. Clarkson, K. Sahu, J. Anderson, T.E. Smith, T.M. Brown, R.M. Rich, S. Casertano, H.E. Bond, M. Livio, D. Minniti, N. Panagia, A. Renzini, J. Valenti and M. Zoccali, *ApJ* **684** (2008), 1110

W.I. Clarkson, K.C. Sahu, J. Anderson, R.M. Rich, T.E. Smith, T.M. Brown, H.E. Bond, M. Livio, D. Minniti, A. Renzini and M. Zoccali, *ApJ* **735** (2011), 37

G. de Vaucouleurs (1964), in IAU Symposium, Vol. 20, The Galaxy and the Magellanic Clouds, ed. F. J. Kerr, 195

V.P. Debattista, L. Mayer, C.M. Carollo, B. Moore, J. Wadsley and T. Quinn, *ApJ* **645** (2006), 209

V.P. Debattista, M. Ness, O.A. Gonzalez, K. Freeman, M. Zoccali and D. Minniti, *MNRAS* **469** (2017), 1587

I. Dékány, D. Minniti, M. Catelan, M. Zoccali, R.K. Saito, M. Hempel and O.A. Gonzalez, *ApJ* **776** (2013), L19

P. Di Matteo, *PASA* **33** (2016), e027

J. Falcón-Barroso, R.F. Peletier and M. Balcells, *MNRAS* **335** (2002), 741

S. Feltzing and G. Gilmore, *A&A* **355** (2000), 949

F.R. Ferraro, A. Sills, R.T. Rood, B. Paltrinieri and R. Buonanno, *ApJ* **588** (2003), 464

I. Ferreras, R.F.G. Wyse and J. Silk, *MNRAS* **345** (2003), 1381

F. Fragkoudi, P. Di Matteo, M. Haywood, S. Khoperskov, A. Gomez, M. Schultheis, F. Combes and B. Semelin, *A&A* **607** (2017), L4

K. Freeman, M. Ness, E. Wylie-de-Boer, E. Athanassoula, J. Bland-Hawthorn, M. Asplund, G. Lewis, D. Yong, R. Lane, L. Kiss and R. Ibata, *MNRAS* **428** (2013), 3660

J.P. Fulbright, A. McWilliam and R.M. Rich, *ApJ* **636** (2006), 821

J.P. Fulbright, A. McWilliam and R.M. Rich, *ApJ* **661** (2007), 1152

O. Gerhard and I. Martinez-Valpuesta, *ApJ* **744** (2012), L8

G. Gilmore, S. Randich, M. Asplund, J. Binney, P. Bonifacio, J. Drew, S. Feltzing, A. Ferguson, R. Jeffries, G. Micela and et al., *The Messenger* **147** (2012), 25

O.A. Gonzalez, M. Rejkuba, D. Minniti, M. Zoccali, E. Valenti and R.K. Saito, *A&A* **534** (2011), L14

O.A. Gonzalez, M. Rejkuba, M. Zoccali, E. Valent, D. Minniti and R. Tobar, *A&A* **552** (2013), A110

O.A. Gonzalez, M. Rejkuba, M. Zoccali, E. Valenti, D. Minniti, M. Schultheis, R. Tobar and B. Chen, *A&A* **543** (2012), A13

O.A. Gonzalez, M. Zoccali, V.P. Debattista, J. Alonso-García, E. Valenti and D. Minniti, *ArXiv e-prints* (2015), [`arXiv:1510.05943`]

O.A. Gonzalez, M. Zoccali, S. Vasquez, V. Hill, M. Rejkuba, E. Valenti, A. Rojas-Arriagada, A. Renzini, C. Babusiaux, D. Minniti and T.M. Brown, *A&A* **584** (2015), A46

F. Gran, D. Minniti, R.K. Saito, M. Zoccali, O.A. Gonzalez, C. Navarrete, M. Catelan, R. Contreras Ramos, F. Elorrieta, S. Eyheramendy and A. Jordán, *A&A* **591** (2016), A145

M. Haywood, P. Di Matteo, O. Snaith and A. Calamida, *A&A* **593** (2016), A82

A. Helmi, *A&A Rev.* **15** (2008), 145

S. Hidalgo and A. Aparicio, *Mem. Soc. Astron. Italiana* **87** (2016), 350

C.D. Howard, R.M. Rich, D.B. Reitzel, A. Koch, R. De Propris and H. Zhao, *ApJ* **688** (2008), 1060

M. Jurić, Ž. Ivezić, A. Brooks, R.H. Lupton, D. Schlegel, D. Finkbeiner, N. Padmanabhan, N. Bond, B. Sesar, C.M. Rockosi, G.R. Knapp, J.E. Gunn, T. Sumi, D.P. Schneider, J.C. Barentine, H.J. Brewington, J. Brinkmann, M. Fukugita, M. Harvanek, S.J. Kleinman, J. Krzesinski, D. Long, E.H. Neilsen, Jr., A. Nitta, S.A. Snedden and D.G. York, *ApJ* **673** (2008), 864

S.G. Kleinmann (1992), in Astronomical Society of the Pacific Conference Series, Vol. 34, Robotic Telescopes in the 1990s, ed. A. V. Filippenko, 203–212

J. Kormendy and R.C. Kennicutt, Jr., *ARA&A* **42** (2004), 603

K. Kuijken and R.M. Rich, *AJ* **124** (2002), 2054

A. Kunder, A. Koch, R.M. Rich, R. de Propris, C.D. Howard, S.A. Stubbs, C.I. Johnson, J. Shen, Y. Wang, A.C. Robin, J. Kormendy, M. Soto, P. Frinchaboy, D.B. Reitzel, H. Zhao and L. Origlia, *AJ* **143** (2012), 57

A. Kunder, R.M. Rich, A. Koch, J. Storm, D.M. Nataf, R. De Propris, A.R. Walker, G. Bono, C.I. Johnson, J. Shen and Z.Y. Li, *ApJ* **821** (2016), L25

J.R. Lewis, M. Irwin and P. Bunclark (Dec. 2010), in Astronomical Society of the Pacific Conference Series, Vol. 434, Astronomical Data Analysis Software and Systems XIX, ed. Y. Mizumoto, K.-I. Morita, & M. Ohishi, 91

S.R. Majewski (Jan. 2012), in American Astronomical Society Meeting Abstracts, Vol. 219, American Astronomical Society Meeting Abstracts #219, 205.06

S.R. Majewski, R.P. Schiavon, P.M. Frinchaboy, C. Allende Prieto, R. Barkhouser, D. Bizyaev, B. Blank, S. Brunner, A. Burton, R. Carrera, S.D. Chojnowski, K. Cunha, C. Epstein, G. Fitzgerald, A.E. Garcia Perez, F.R. Hearty, C. Henderson, J.A. Holtzman, J.A. Johnson, C.R. Lam, J.E. Lawler, P. Maseman, S. Meszaros, M. Nelson, D. Coung Nguyen, D.L. Nidever, M. Pinsonneault, M. Shetrone, S. Smee, V.V. Smith, T. Stolberg, M.F. Skrutskie, E. Walker, J.C. Wilson, G. Zasowski, F. Anders, S. Basu, S. Beland, M.R. Blanton, J. Bovy, J.R. Brownstein, J. Carlberg, W. Chaplin, C. Chiappini, D.J. Eisenstein, Y. Elsworth, D. Feuillet, S.W. Fleming, J. Galbraith-Frew, R.A. Garcia, D. Anibal Garcia-Hernandez, B.A. Gillespie, L. Girardi, J.E. Gunn, S. Hasselquist, M.R. Hayden, S. Hekker, I. Ivans, K. Kinemuchi, M. Klaene, S. Mahadevan, S. Mathur, B. Mosser, D. Muna, J.A. Munn, R.C. Nichol, R.W. O'Connell, A.C. Robin, H. Rocha-Pinto, M. Schultheis, A.M. Serenelli, N. Shane, V. Silva Aguirre, J.S. Sobeck, B. Thompson, N.W. Troup, D.H. Weinberg and O. Zamora, *ArXiv e-prints* (2015), [`arXiv:1509.05420`]

M. Martig, M. Fouesneau, H.W. Rix, M. Ness, S. Mészáros, D.A. García-Hernández, M. Pinsonneault, A. Serenelli, V. Silva Aguirre and O. Zamora, *MNRAS* **456** (2016), 3655

F. Matteucci, D. Romano and P. Molaro, *A&A* **341** (1999), 458

A. McWilliam, *PASA* **33** (2016), e040

A. McWilliam and R.M. Rich, *ApJS* **91** (1994), 749

A. McWilliam and M. Zoccali, *ApJ* **724** (2010), 1491

D. Minniti, *PASP* **106** (1994), 813

D. Minniti (Jan. 2016), in Galactic Surveys: New Results on Formation, Evolution, Structure and Chemical Evolution of the Milky Way, 10

D. Minniti, P.W. Lucas, J.P. Emerson, R.K. Saito, M. Hempel, P. Pietrukowicz, A.V. Ahumada, M.V. Alonso, J. Alonso-Garcia, J.I. Arias, R.M. Bandyopadhyay, R.H. Barbá, B. Barbuy, L.R. Bedin, E. Bica, J. Borissova, L. Bronfman, G. Carraro, M. Catelan, J.J. Clariá, N. Cross, R. de Grijs, I. Dékány, J.E. Drew, C. Fariña, C. Feinstein, E. Fernández Lajús, R.C. Gamen, D. Geisler, W. Gieren, B. Goldman, O.A. Gonzalez, G. Gunthardt, S. Gurovich, N.C. Hambly, M.J. Irwin, V.D. Ivanov, A. Jordán, E. Kerins, K. Kinemuchi, R. Kurtev, M. López-Corredoira, T. Maccarone, N. Masetti, D. Merlo,

M. Messineo, I.F. Mirabel, L. Monaco, L. Morelli, N. Padilla, T. Palma, M.C. Parisi, G. Pignata, M. Rejkuba, A. Roman-Lopes, S.E. Sale, M.R. Schreiber, A.C. Schröder, M. Smith, L.S. , Jr., M. Soto, M. Tamura, C. Tappert, M.A. Thompson, I. Toledo, M. Zoccali and G. Pietrzynski, *New A* **15** (2010), 433

D.M. Nataf, *PASA* **33** (2016), e023

D.M. Nataf and A.P. Gould, *ApJ* **751** (2012), L39

D.M. Nataf, A. Udalski, A. Gould, P. Fouqué and K.Z. Stanek, *ApJ* **721** (2010), L28

M. Ness, K. Freeman, E. Athanassoula, E. Wylie-de-Boer, J. Bland-Hawthorn, M. Asplund, G.F. Lewis, D. Yong, R.R. Lane and L.L. Kiss, *MNRAS* **430** (2013), 836

M. Ness, K. Freeman, E. Athanassoula, E. Wylie-de-Boer, J. Bland-Hawthorn, M. Asplund, G.F. Lewis, D. Yong, R.R. Lane, L.L. Kiss and R. Ibata, *MNRAS* **432** (2013), 2092

M. Ness, K. Freeman, E. Athanassoula, E. Wylie-De-Boer, J. Bland-Hawthorn, G.F. Lewis, D. Yong, M. Asplund, R.R. Lane, L.L. Kiss and R. Ibata, *ApJ* **756** (2012), 22

M. Ness, G. Zasowski, J.A. Johnson, E. Athanassoula, S.R. Majewski, A.E. García Pérez, J. Bird, D. Nidever, D.P. Schneider, J. Sobeck, P. Frinchaboy, K. Pan, D. Bizyaev, D. Oravetz and A. Simmons, *ApJ* **819** (2016), 2

S. Nishiyama, M. Tamura, H. Hatano, D. Kato, T. Tanabé, K. Sugitani and T. Nagata, *ApJ* **696** (2009), 1407

S. Ortolani, A. Renzini, R. Gilmozzi, G. Marconi, B. Barbuy, E. Bica and R.M. Rich, *Nature* **377** (1995), 701

A. Pietrinferni, S. Cassisi, M. Salaris and F. Castelli, *ApJ* **612** (2004), 168

A. Pietrinferni, S. Cassisi, M. Salaris and F. Castelli, *ApJ* **642** (2006), 797

A. Pietrinferni, S. Cassisi, M. Salaris and S. Hidalgo, *A&A* **558** (2013), A46

A. Pietrinferni, M. Molinaro, S. Cassisi, F. Pasian, M. Salaris, D. Pelusi, P. Manzato and C. Vuerli, *Astronomy and Computing* **7** (2014), 95

P. Pietrukowicz, S. Kozłowski, J. Skowron, I. Soszyński, A. Udalski, R. Poleski, Ł. Wyrzykowski, M.K. Szymański, G. Pietrzyński, K. Ulaczyk, P. Mróz, D.M. Skowron and M. Kubiak, *ApJ* **811** (2015), 113

M. Portail, C. Wegg and O. Gerhard, *MNRAS* **450** (2015), L66

S. Randich, G. Gilmore and Gaia-ESO Consortium, *The Messenger* **154** (2013), 47

A. Renzini and F. Fusi Pecci, *ARA&A* **26** (1988), 199

A. Renzini, M. Gennaro, M. Zoccali, T.M. Brown, J. Anderson, D. Minniti, K.C. Sahu, E. Valenti and D.A. VandenBerg, *ApJ* **863** (2018), 16

R.M. Rich, *AJ* **95** (1988), 828

R.M. Rich, *ApJ* **362** (1990), 604

R.M. Rich and L. Origlia, *ApJ* **634** (2005), 1293

R.M. Rich, L. Origlia and E. Valenti, *ApJ* **665** (2007), L119

R.M. Rich, L. Origlia and E. Valenti, *ApJ* **746** (2012), 59

R.M. Rich, D.B. Reitzel, C.D. Howard and H. Zhao, *ApJ* **658** (2007), L29

A.C. Robin, C. Reylé, S. Derrière and S. Picaud, *A&A* **409** (2003), 523

A. Rojas-Arriagada, A. Recio-Blanco, P. de Laverny, Š. Mikolaitis, F. Matteucci, E. Spitoni, M. Schultheis, M. Hayden, V. Hill, M. Zoccali, D. Minniti, O.A. Gonzalez, G. Gilmore, S. Randich, S. Feltzing, E.J. Alfaro, C. Babusiaux, T. Bensby, A. Bragaglia, E. Flaccomio, S.E. Koposov, E. Pancino, A. Bayo, G. Carraro, A.R. Casey, M.T. Costado, F. Damiani, P. Donati, E. Franciosini, A. Hourihane, P. Jofré, C. Lardo, J. Lewis, K. Lind, L. Magrini, L. Morbidelli, G.G. Sacco, C.C. Worley and S. Zaggia, *A&A* **601** (2017), A140

R.K. Saito, M. Hempel, D. Minniti, P.W. Lucas, M. Rejkuba, I. Toledo, O.A. Gonzalez, J. Alonso-García, M.J. Irwin, E. Gonzalez-Solares, S.T. Hodgkin, J.R. Lewis, N. Cross, V.D. Ivanov, E. Kerins, J.P. Emerson, M. Soto, E.B. Amôres, S. Gurovich, I. Dékány, R. Angeloni, J.C. Beamin, M. Catelan, N. Padilla, M. Zoccali, P. Pietrukowicz, C. Moni Bidin, F. Mauro, D. Geisler, S.L. Folkes, S.E. Sale, J. Borissova, R. Kurtev, A.V. Ahumada, M.V. Alonso, A. Adamson, J.I. Arias, R.M. Bandyopadhyay, R.H. Barbá, B. Barbuy, G.L. Baume, L.R. Bedin, A. Bellini, R. Benjamin, E. Bica, C. Bonatto, L. Bronfman, G. Carraro, A.N. Chenè, J.J. Clariá, J.R.A. Clarke, C. Contreras, A. Corvillón, R. de Grijs, B. Dias, J.E. Drew, C. Fariña, C. Feinstein, E. Fernández-Lajús, R.C. Gamen, W. Gieren, B. Goldman, C. González-Fernández, R.J.J. Grand, G. Gunthardt, N.C. Hambly, M.M. Hanson, K.G. Hełminiak, M.G. Hoare, L. Huckvale, A. Jordán, K. Kinemuchi, A. Longmore, M. López-Corredoira, T. Maccarone, D. Majaess, E.L. Martín, N. Masetti, R.E. Mennickent, I.F. Mirabel, L. Monaco, L. Morelli, V. Motta, T. Palma, M.C. Parisi, Q. Parker, F. Peñaloza, G. Pietrzyński, G. Pignata, B. Popescu, M.A. Read, A. Rojas, A. Roman-Lopes, M.T. Ruiz, I. Saviane, M.R. Schreiber, A.C. Schröder, S. Sharma, M.D. Smith, L. Sodré, J. Stead, A.W. Stephens, M. Tamura, C. Tappert, M.A. Thompson, E. Valenti, L. Vanzi, N.A. Walton, W. Weidmann and A. Zijlstra, *A&A* **537** (2012), A107

R.K. Saito, D. Minniti, B. Dias, M. Hempel, M. Rejkuba, J. Alonso-García, B. Barbuy, M. Catelan, J.P. Emerson, O.A. Gonzalez, P.W. Lucas and M. Zoccali, *A&A* **544** (2012), A147

R.K. Saito, M. Zoccali, A. McWilliam, D. Minniti, O.A. Gonzalez and V. Hill, *AJ* **142** (2011), 76

M. Salaris and L. Girardi, *MNRAS* **337** (2002), 332

F.A. Santana, R.R. Muñoz, T.J.L. de Boer, J.D. Simon, M. Geha, P. Côté, A.E. Guzmán, P. Stetson and S.G. Djorgovski, *ApJ* **829** (2016), 86

F.A. Santana, R.R. Muñoz, M. Geha, P. Côté, P. Stetson, J.D. Simon and S.G. Djorgovski, *ApJ* **774** (2013), 106

S. Saracino, E. Dalessandro, F.R. Ferraro, D. Geisler, F. Mauro, B. Lanzoni, L. Origlia, P. Miocchi, R.E. Cohen, S. Villanova and C. Moni Bidin, *ApJ* **832** (2016), 48

M. Schultheis, A. Rojas-Arriagada, A.E. García Pérez, H. Jönsson, M. Hayden, G. Nandakumar, K. Cunha, C. Allende Prieto, J.A. Holtzman, T.C. Beers, D. Bizyaev, J. Brinkmann, R. Carrera, R.E. Cohen, D. Geisler, F.R. Hearty, J.G. Fernandez-Tricado, C. Maraston, D. Minnitti, C. Nitschelm, A. Roman-Lopes, D.P. Schneider, B. Tang, S. Villanova, G. Zasowski and S.R. Majewski, *A&A* **600** (2017), A14

A. Sollima, G. Beccari, F.R. Ferraro, F. Fusi Pecci and A. Sarajedini, *MNRAS* **380** (2007), 781

P.B. Stetson, *PASP* **99** (1987), 191

P.B. Stetson (1993), in IAU Colloq. 136: Stellar Photometry - Current Techniques and Future Developments, ed. C. J. Butler & I. Elliott, Vol. 136, 291

P.B. Stetson, *PASP* **106** (1994), 250

F. Surot, S. Hidalgo, E. Valenti, E. Sökmen, M. Rejkuba, M. Zoccali and D. Minniti, *A&A* (2018b, in prep)

F. Surot, E. Valenti, S.L. Hidalgo, M. Zoccali, E. Sökmen, M. Rejkuba, D. Minniti, O.A. Gonzalez, S. Cassisi, A. Renzini and A. Weiss, *A&A* (2018a, submitted)

M.B. Taylor (Jul. 2006), in Astronomical Society of the Pacific Conference Series, Vol. 351, Astronomical Data Analysis Software and Systems XV, ed. C. Gabriel, C. Arviset, D. Ponz, & S. Enrique, 666

D.M. Terndrup, *AJ* **96** (1988), 884

A. Udalski, M. Szymanski, J. Kaluzny, M. Kubiak and M. Mateo, *Acta Astron.* **42** (1992), 253

A. Udalski, M.K. Szymański and G. Szymański, *Acta Astron.* **65** (2015), 1

E. Valenti, M. Zoccali, O.A. Gonzalez, D. Minniti, J. Alonso-García, E. Marchetti, M. Hempel, A. Renzini and M. Rejkuba, *A&A* **587** (2016), L6

E. Valenti, M. Zoccali, A. Mucciarelli, O.A. Gonzalez, F. Surot Madrid, D. Minniti, M. Rejkuba, L. Pasquini, G. Fiorentino, G. Bono, R.M. Rich and M. Soto, *ArXiv e-prints* (2018), [`arXiv:1805.00275`]

E. Valenti, M. Zoccali, A. Renzini, T.M. Brown, O.A. Gonzalez, D. Minniti, V.P. Debattista and L. Mayer, *A&A* **559** (2013), A98

S. van den Bergh and E. Herbst, *AJ* **79** (1974), 603

C. Wegg and O. Gerhard, *MNRAS* **435** (2013), 1874

C. Wegg, O. Gerhard and M. Portail, *MNRAS* **450** (2015), 4050

J.L. Weiland, R.G. Arendt, G.B. Berriman, E. Dwek, H.T. Freudenreich, M.G. Hauser, T. Kelsall, C.M. Lisse, M. Mitra, S.H. Moseley, N.P. Odegard, R.F. Silverberg, T.J. Sodroski, W.J. Spiesman and S.W. Stemwedel, *ApJ* **425** (1994), L81

Y. Xu, C. Liu, X.X. Xue, H.J. Newberg, J.L. Carlin, Q.R. Xia, L.C. Deng, J. Li, Y. Zhang, Y. Hou, Y. Wang and Z. Cao, *MNRAS* **473** (2018), 1244

M. Zoccali, O.A. Gonzalez, S. Vasquez, V. Hill, M. Rejkuba, E. Valenti, A. Renzini, A. Rojas-Arriagada, I. Martinez-Valpuesta, C. Babusiaux, T. Brown, D. Minniti and A. McWilliam, *A&A* **562** (2014), A66

M. Zoccali, V. Hill, A. Lecureur, B. Barbuy, A. Renzini, D. Minniti, A. Gómez and S. Ortolani, *A&A* **486** (2008), 177

M. Zoccali, A. Renzini, S. Ortolani, L. Greggio, I. Saviane, S. Cassisi, M. Rejkuba, B. Barbuy, R.M. Rich and E. Bica, *A&A* **399** (2003), 931

M. Zoccali and E. Valenti, *PASA* **33** (2016), e025

M. Zoccali, E. Valenti and O.A. Gonzalez, *ArXiv e-prints* (2018), [`arXiv:1807.06377`]

M. Zoccali, S. Vasquez, O.A. Gonzalez, E. Valenti, A. Rojas-Arriagada, J. Minniti, M. Rejkuba, D. Minniti, A. McWilliam, C. Babusiaux, V. Hill and A. Renzini, *A&A* **599** (2017), A12

Acknowledgments

Thanks to Elena Valenti, my supervisor at the European Southern Observatory (ESO). Not only from the scientific perspective, where her continued support, guidance and encouragement played an undoubtedly crucial part in what I have achieved, but also on a personal level, for her disposition, kindness, hospitality and welcoming demeanor, often beyond mere duty.

Thanks to Sebastián Hidalgo. His early involvement provided the foundations upon which this work is based.

Thanks to my referees, Prof. Dr. Achim Weiss and PD Dr. Markus Kissler-Patig, for not only having accepted such role and providing guidance, but also showing encouraging interest in my work.

Thanks to ESO, Max-Planck Institute and their people, without whom none of this would have been possible.

Thanks to Dante, Joyce, Marina, Manuela, Enrico and so many others who helped me be where I am now. To those people I met along the way and provided often illuminating and interesting discussions over a cup of coffee.

To my friends, who despite the distance and almost mythical presence, helped me keep my sanity throughout this experience.

A mis padres, Myrtha y Francisco, quienes me han dado su apoyo y amor incondicionales a cada paso. A mis hermanas, cuñados y sobrinos, quienes no han perdido un día de contacto.

A mis abuelos, Olieta y Florial, a quienes no pude sino despedir de lejos. A su memoria dedico mi trabajo.

I acknowledge the support by the DFG Cluster of Excellence ”Origin and Structure of the Universe”. The simulations have been carried out on the computing facilities of the Computational Center for Particle and Astrophysics (C2PAP).